Journal of Analytical & Numerical Methods in Mining Engineering

Volume 15, No.45, Winter 2026 ISSN: 2251-6565

In The Name of Allah, the Most Compassionate, the Most Merciful

Journal of Analytical and Numerical Methods in Mining Engineering

Islamic World Science Citation Center

Directory of Open Access Journals

Regional Information Center for Science and Technology RICeST

Indexed by Scopus

Volume 15, No. 45, Winter 2026

Journal of Analytical and Numerical Methods in Mining Engineering

Grantee and Publisher: Yazd University, Department of Mining and Metallurgy
Director in chief: Dr. Alireza Yarahmadi Bafghi
Editor in chief: Dr. Mohammad Fatehi Marji
Manager: Dr. Manouchehr Sanei
Executive Director: Mrs. Mahdieh Dehghan Harati

Editorial Board:

Dr. Abdolhamid Ansari (Associate prof., Mining, Geo-Physics, Yazd University, Iran)
Dr. Raheb Bagherpour (Professor, Mining Exploration, Isfahan University of Technology, Iran)
Dr. Reza Dehghan (Associate prof., Mineral Processing, Yazd University, Iran)
Dr. Mohammad Fatehi Marji (Professor, Rock Mechanics, Yazd University, Iran)
Dr. Javad Gholamnejad (Professor, Mining Exploitation, Yazd University, Iran)
Dr. Abolghasem kamkar rouhani (Professor, Mining Exploration, Shahrood University of Technology, Iran)
Dr. Ahmad Khodadadi (Professor, Mineral Processing, Tarbiat Modares University, Iran)
Dr. Ahmadreza Mokhtari (Associate Prof., Mining Exploration, Isfahan University of Technology, Iran)
Dr. Reza Rahmannejad (Professor, Rock Mechanics, Shahid Bahonar University of Kerman, Iran)
Dr. Hojjatollah Ranjbar (Professor, Economic Geology, Shahid Bahonar University of Kerman, Iran)
Dr. Alireza Yarahmadi Bafghi (Associate Prof., Geo-mechanics, Yazd University, Iran)

International Editorial Board:

Dr. Celal Karpuz (Professor, Rock Mechanics, Middle East Technical University, Ankara, Turkey)

Dr. Thierry Verdel (Professor, Risks and Vulnerability in Geomechanics, Institute National Polytechnique de Lorraine (INPL), Nancy, France)

Editor:

Mrs. Mahdieh Dehghan Harati, Dr. Manouchehr Sanei

Supporters:

Iran Central Iron Ore Company- Bafgh (ICIOC)
Mining Technologies Research Center, Yazd University
Iranian Society of Mining Engineering

Address:

Department of Mining and Metallurgy, Yazd University, Pajouhesh Street, Safaeieh, Yazd, Iran
Postal Box: 89195-741 - **Tell:** +9835-38200131 - **Fax:** +9835-38200131

Email: *mm-journal@journals.yazd.ac.ir* **Website:** *www.anm.yazd.ac.ir*

Table of Content

Vol. 15, No. 45, Winter 2026, pages 1-11

Journal of Analytical and Numerical Methods in Mining Engineering

Journal home page: http://anm.yazd.ac.ir/

Research article

Prediction and Optimization of Roadheader Performance based on Characteristics and Geo-Mechanical Parameters of Rock (Case Study: TABAS Parvedeh coal mine No. 1)

Amin Faramarz[1], Gholamreaz Saeedi[2]*, Ali Hosseini[3], Sajjad Aghababaei[2]

1- **Dept. of Mining Engineering, Zarand Higher Education Complex, Shahid Bahonar University of Kerman, Kerman, Iran**

2- **Dept. of Mining Engineering, Faculty of Engineering and Technology, Shahid Bahonar University of Kerman, Kerman, Iran**

3- **Dept. of Mining and Metallurgy Engineering, Yazd University, Yazd, Iran**

*Corresponding author: E-mail: *gsaeedi@uk.ac.ir*

*(*Received*: February 2024*, Accepted*: September 2025)*

DOI: 10.22034/ANM.2025.21296.1628

Keywords

Performance prediction

Roadheader

Nonlinear and linear regression

Coal mine

Particle Swarm Optimization

Abstract

Roadheader machines have good efficiency and flexibility in mechanized tunneling and underground mining. The application of Roadheaders increases the speed of excavation in the tunnels, which dramatically reduces the time and cost of the project. Considering the importance of this issue, this study aims to predict and optimize the penetration rate and excavation speed of Roadheaders using the particle swarm algorithm in Parvadeh No. 1 mechanized coal mine. Therefore, in this study, the characteristics of Roadheaders have been investigated in related studies. All of these studies were divided into two parts: field observations and laboratory tests. In this research, tunnel number one is considered as the case study, which is divided into 30 parts/sections, and in each section, rock core/sample preparation, the number of joints along the tunnel, excavation time, and volume of the excavated rock mass under the Roadheader machine operation were measured. In the laboratory studies section, the rock core was analyzed by the uniaxial compression strength (UCS) test, and finally, a database was provided based on the obtained results. In the following, nonlinear and linear regression models were used to select the best model for estimating the instantaneous cutting rate (ICR) of the Roadheader machine, which expresses the advancing rate of excavation. In these models, parameters including rock quality designation (RQD) of rock mass, tensile strength (σt), UCS, rock mass brittleness index (RMBI), pick consumption index (PCI), pick consumption factor (PCf), and specific energy (SE) were selected as input variables, and ICR was selected as the output variable. By comparing the results, the linear regression model had the highest determination coefficient and performance index, and the lowest root mean square error. Therefore, this model was selected as the most suitable model. In order to optimize ICR, the relationship obtained from the linear regression model was implemented in the particle swarm algorithm. The results showed that to obtain the optimal limit of ICR in the considered case study with a UCS of 1.68 MPa and a RQD of 33.09%, ICR is equal to 33.11 cubic meters per hour.

1. INTRODUCTION

Mechanized tunneling systems can be a suitable alternative to the traditional method of mining operations because they can be performed more precisely and faster at a lower cost, and produce more productive output [1]. In addition,

with the application of the mechanized method, the maintenance and the required manpower are reduced. Due to new developments and enhancements to increase the performance and reliability of drilling machines, miners who use mechanized excavation systems have a larger share of the mineral products market [2, 3]. Some of the more important factors in mechanized excavation are the prediction of costs and completion time of the project, which depend on the performance of the machine and its efficiency. Predicting the performance of the machine will have a direct effect on the speed of production and ultimately the profitability of excavation projects [4, 5].

Generally, the factors affecting the performance of excavation operations can be classified into four main categories which are described in the following.

A– Rock material parameters consist of compressive and tensile strength, hardness percent, abrasive minerals (quartz), type of texture and matrix of rock, elastic behavior, and rock energy properties such as rigidity index

B– Rock mass parameters such as the joint inclination, joint spacing, direction of discontinuities, junctions, groundwater, fault areas, position of the frontier, general classification of the rockmass, maintenance requirements, and field stress [6, 7].

C- Machine characteristics, including weight, power, machine forces, type of drum cutter, arrangement of cutting tools, and support system capacity.

D- Operation parameters consisting of shape, size, inclination, and length of excavation, path arc, drilling arrangement, acceleration operations, number of rock formations in the tunnel path, site management method, and work scheduling, which is the number of work shifts per day [8-11].

A combination of these parameters specifies the speed of excavation operation and the capacity of the machine production in a rockmass [12]. In this research, we attempt to present a model predicting the performance of a Roadheader based on geomechanically parameters of rock and drilling machine characteristics in a fully mechanized coal mine in Parvadeh No. 1 mine.

2. GENERAL STATUS AND CHARACTERISTICS OF PARVADEH NO. 1 COAL MINE OF TABAS

Tabas's city is located in the northeast of Yazd Province, Iran. Figure 1 shows the plan of Parvadeh No. 1. The thickness of the main coal zone is approximately 100 m, including five coal seams called B1, B2, C1, C2, and D which have the applicable thickness. Among these layers, the three layers C1, B2, and B1 are extractable economically. Coal seams are accessed by four diagonal tunnels with an inclination of 14 degrees. The mechanized longitudinal longwall method is used to extract the coal seams. In this mine, the Roadheader machine has been applied to develop the excavations such as roadways, slopes, cross-cuts [13, 14].

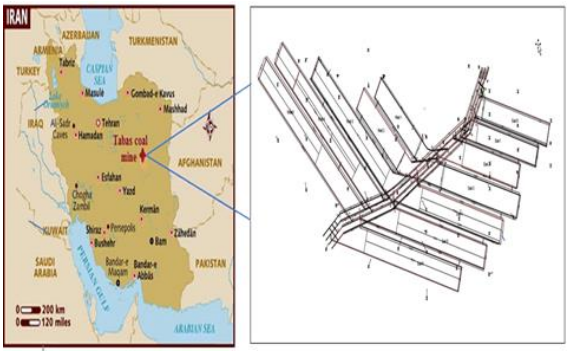

Fig. 1. The Tabas Parvadeh No. 1 coal mine [14].

In tunnel No.1 of the mine, four road-header machines were used excavation operation (Fig. 2). The model of these machines is DOSCO MD1100. It should be noted that in this mine, drilling and blasting systems are used in the conditions of existing hard rock formations (sandstone). The Roadheader machine is ranked among the lightweight to medium-weight machines. According to the application levels in British charcoal mines, this Roadheader is an ideal device for the extraction of mixed layers. Table 1 shows the main characteristics of the machine. [15, 16].

Fig. 2. A view of the Roadheader machine with axial excavation method in coal mines of Tabas [17].

Table 1. Observation performed in 30 tunnel sections

Roadheader characteristics	Unit	Value
Car length	mm	8066
Main body height of the machine	mm	1860
Body width of the machine	mm	2500
Boom rotation angle	degree	45
Cutting height maximum	mm	4700
Cutting width maximum	m	6160
Machine weight	ton	34
Cutting slice speed	rpm	32-58
Movement speed	m per sec	1.18
Conveyor width	mm	615

3. INVESTIGATING THE PERFORMANCE OF ROADHEADER MACHINE

Road headers are generally suitable for low to medium-strength rocks. There is no direct relationship between the machine and the tunnel shape. The cross-section of the tunnel excavated using this machine can be different. The tunnel surface is directly available at any time because these machines directly affect the bottom of the tunnel; it should have sufficient load capacity [18, 19].

Researchers have developed a lot of relationships to determine the infiltration rate of Roadheaders. Bilgin and colleagues presented Eq. (1) for the instantaneous cutting rate (ICR) for various transverse and axial Roadheaders [1].

$$ICR = 9.07Ln(RMBI) + 29.93 \quad (1)$$

where RMBI is the Rock mass brittleness index. This is calculated by Eq. (2) [1].

$$RMBI = e^{\left(\frac{\sigma c}{\sigma t}\right)} \times \left(\frac{RQD}{100}\right)^3 \quad (2)$$

In Eq. (2), σc is uniaxial compressive strength of intact rock; σt is the tensile strength of the intact rock, and RQD is the rock quality designation of rockmass. RQD of the rock mass is one of the most important factors affecting the performance of the Roadheader. In this study, this parameter is evaluated by Eq. (3) presented by Prest and Hudson [22].

$$RQD = 100e^{-0.1\lambda}(0.1\lambda + 1) \quad (3)$$

In Eq. (3), λ is the number of joints along the exaction strike/line. Using RMBI, we can calculate the pick consumption index (PCI) of Roadheader as the Eq. (4) [1].

$$PCI = e^{RMBI} \times \left(\frac{UCS}{P}\right) \quad (4)$$

In Eq. (4), UCS is the uniaxial compressive strength of the rock and P is the power of the digger, which is equal 84 KW. The pick consumption factor is a function (PCF) of PCI, which is calculated by Eq. (5) [1].

$$PCF = 45.67(PCI)^{-0.16} \quad (5)$$

The specific energy (SE) for the Roadheader is a function of σc, which can be calculated by the following equation: [1].

$$SE = 0.123\sigma_c + 0.97 \quad (6)$$

4. PSO ALGORITHM (PARTICLE SWARM OPTIMIZATION)

PSO (Particle Swarm Optimization) is an optimization method that can be used to deal with problems whose answers are a point or a surface in n-dimensional space. In this space, the assumptions are discussed, an initial speed is allocated to them, and communication channels are considered between particles. Then, these particles move in the space of the reaction, and the results are calculated based on a merit criterion after each period. Over time, particles tend to accelerate toward particles with a higher degree of merit and are in the same communication group. Despite the fact that every method works well in a range of issues, this method has been successful in solving continuous optimization problems. Using this algorithm, we can optimize the Roadheader progress rate [21]. There are four steps for PSO algorithm, which are mentioned in the following:

(1) Creating a critical mass and evaluating it;

(2) Determining the best personal memories and the best collective memories;

(3) Updating the speed and position;

(4) If the stop conditions are not met, go to step 1 otherwise, it will end.

The termination conditions of this algorithm are as follows:

1) To reach an acceptable response rate,

2) The number of repetitions,

3) The number of repetitions passed without a certain improvement in the result, and

4) Completing a certain number of responses [18].

Particle deformation in this algorithm is based on the experience of the particles and the rest of the particles. Particles tend to experience the best

position and direction that they themselves or other neighbors have taken in the past. In general, it can be stated that the behavior and position of the rest of the particles on the hair are influenced by a small particle to achieve successful particles. Modeling PSO is also based on the search for successful particle swarming points, which has transformed PSO into a social search algorithm [19].

Particles attempt to gain the best position in the search space with respect to the memory of their experiences and knowledge and their collective intelligence. Particles compete to gain the best position over the rest of their neighbors [19].

5. DATA COFLLECTION

Database was created based on the data collected through the field and the laboratory, which are described in the following:

A- Field observations: In this section, the tunnel considered as the case study was divided into 30 parts along the tunnel strike and in each section, the rock core sampling work was carried out using a machine tool. In each section, three rock cores with a diameter of 54 mm were drilled. Simultaneously, the number of joints in the tunnel was counted along a withdrawal line. The number of joints in these 30 sections recorded between 22 to 26. During the Roadheader operation, the time and volume were also measured for excavating each section (Table 2).

B- Laboratory tests: The rock cores drilled in the tunnel were examined in the laboratory under a point load test to calculate the UCS and tensile strength. The height of the rock samples was 27–53 mm, and their diameter was 54 mm in all tests.

Many methods can be used to obtain tensile and compressive strength, one of which is the use of a point test. Point load testing is performed on small pieces of rock called cores[21]. Based on the described process to create the database, the required data was collected. In this regard, data about parameters, including the type of rock, excavating volume, time, number of joints per unit length, and RQD are presented in Table 2. Table 3 illustrates the data of point load index, compressive strength, and tensile strength of the rock. In the following, the amounts of RMBI, PCI, PCF, SE, and ICR were determined and the results are presented in (Table 4).

Table 2. Observation performed in 30 tunnel sections

excavating ring	Type of rock	excavating volume (m3)	time (min)	Number of joints per unit length (λ)	RQD%
1	Argillite	23.4	60	25	28.73
2	Silt-stone	22.5	54	24	30.84
3	Silt-stone	22.8	89	20	40.60
4	Argillite	25	49	22	35.46
5	Argillite	24.6	81	25	28.73
6	Argillite	25.2	57	24	30.84
7	Silt-stone	22.6	70	24	30.84
8	Silt-stone	22.7	62	22	35.46
9	Silt-stone	23.2	69	24	30.84
10	Argillite	26.4	64	24	30.84
11	Silt-stone	22.9	86	23	33.09
12	Silt-stone	22.4	45	23	33.09
13	Silt-stone	23.1	67	22	35.46
14	Silt-stone	24.2	56	20	40.60
15	Argillite	25.7	58	22	35.46
16	Argillite	24.9	38	22	35.46
17	Argillite	26.1	67	25	28.73
18	Silt-stone	23.2	65	24	30.84
19	Silt-stone	23.7	54	20	28.73
20	Coal	29.9	62	26	26.74
21	Silt-stone	24.2	74	23	33.09
22	Silt-stone	23.8	80	24	30.84
23	Silt-stone	26.1	39	20	40.60
24	Coal	28.4	55	26	26.74
25	Silt-stone	22.3	69	23	33.09
26	Silt-stone	22.9	73	23	33.09
27	Argillite	25.6	49	25	28.73
28	Argillite	26.7	52	24	30.84
29	Silt-stone	23	67	22	35.46
30	Silt-stone	22.8	82	22	35.46

Table 3. Calculations of the point load index, compressive resistance and tensile resistance of samples

Samples	Suitable load to break sample (kN)	Diameter (mm)	Point load index (MPa)	Is (50) (MPa)	Compressive resistance of sample (MPa)	Tensile resistance of sample (MPa)	Correction factor
1	4.20	43.10	2.26	2.11	50.73	2.03	0.94
2	4.90	43.65	2.15	2.10	50.49	2.02	0.98
3	20.89	46.92	2.22	2.16	51.78	2.07	1.07
4	5.11	58.65	1.48	1.59	38.16	1.53	1.09
5	5.02	55.64	1.62	1.70	40.79	1.63	0.99
6	4.73	49.07	1.95	1.93	51.63	2.07	0.94
7	4.12	43.10	2.30	2.15	51.19	2.05	1.02
8	4.93	52.46	1.79	1.83	43.90	1.76	0.96
9	4.74	46.18	2.22	2.14	51.41	2.06	0.94
10	4.31	43.89	2.23	2.10	50.47	2.02	0.95
11	4.37	44.66	2.19	2.08	49.97	2	1.03
12	5.01	53.75	1.73	1.79	42.89	1.72	1.04
13	5.05	55.02	1.66	1.73	41.59	1.66	1.01
14	5.01	51.13	1.91	1.93	46.30	1.85	1.07
15	5.21	58.06	1.54	1.65	39.53	1.58	0.95
16	4.33	44.66	2.17	2.06	49.50	1.98	0.96
17	4.55	45.43	2.20	2.11	50.57	2.02	1.08
18	5.99	59.81	1.67	1.81	43.44	1.74	1.04
19	5.81	55.02	1.92	2.00	48.11	1.92	0.94
20	3.01	43.10	2.18	2.04	48.94	1.96	1.00
21	4.45	50.45	1.74	1.75	41.93	1.68	1.00
22	4.33	79.67	1.74	1.74	41.67	1.67	1.62
23	5.02	54.39	1.6	1.76	42.12	1.68	1.04
24	3.02	43.10	1.99	1.86	44.67	1.79	0.94
25	6.01	60.38	1.64	1.79	42.85	1.71	1.09
26	4.02	44.66	2.01	1.91	45.85	1.83	0.95
27	4.34	51.80	1.61	1.64	39.26	1.57	1.02
28	3.99	43.89	2.07	1.95	36.85	1.87	0.94
29	4.01	46.18	1.88	1.81	43.53	1.74	0.96
30	5.23	53.11	1.85	1.90	45.62	1.82	1.03

Table 4. Calculation of the instantaneous drilling rate

Excavation section	Index fragility of rock mass (RMBI)	Partition consumption index (PCI)	Partition consumption factor (m3/pick)	Specific energy M j/ m3	instantaneous drilling rate (m3/h)
1	1.69	3.27	37.78	7.21	34.79
2	2.1	4.91	35.41	7.18	36.66
3	4.88	81.14	22.60	7.34	44.31
4	3.02	9.31	31.96	5.66	39.95
5	1.47	2.11	40.52	5.99	33.42
6	2.01	4.59	35.79	7.32	36.26
7	2.05	4.73	35.61	7.27	36.44
8	3.03	1.82	31.20	6.37	39.98
9	2.02	4.61	35.76	7.29	36.31
10	2.08	4.81	35.52	7.18	36.57
11	2.55	7.62	33.00	7.12	38.42
12	2.44	5.86	34.42	6.25	38.02
13	3.38	14.54	29.76	6.09	40.98
14	4.95	77.81	22.75	6.66	44.44
15	3.2	12.38	30.53	5.83	40.68
16	1.76	14.46	29.79	7.06	40.48
17	2.04	3.50	37.38	7.19	35.06
18	1.8	3.98	36.62	6.31	36.40
19	1.36	3.46	37.44	6.89	35.26
20	2.5	2.27	40.06	6.99	32.72
21	2.04	6.08	34.21	6.13	38.24
22	5.17	3.82	36.86	6.10	36.40
23	1.3	88.21	22.30	6.15	44.83
24	2.76	1.95	41.04	6.46	32.31
25	2.75	8.06	32.71	6.24	39.14
26	2.71	8.54	32.40	6.61	39.11
27	1.22	2.58	39.23	5.80	34.80
28	2.26	5.14	35.15	6.73	37.16
29	3.42	13.50	30.11	6.32	40.65
30	1.69	16.60	29.13	6.58	41.08

6. STATISTICAL SURVEY OF THE VARIABLES

In this study, descriptive statistics were used to predict the instantaneous drilling rate of inferential statistics (including correlation coefficient and multivariate regression). Descriptive statistics of considered variables/parameters are presented in Table 5.

Table 5. Descriptive statistics of all 30 excavated sections in the considered advancing tunnel

Number	Parameter	Indication	Mean	Minimum	Maximum	Standard deviation
1	instantaneous cutting rate	ICR	21.17	20.54	36.29	3.85
2	Rock quality designation	RQD	14.33	13.75	24.75	6.038
3	Tensile strength	σ_t	0.09	0.59	0.663	0.173
4	Uniaxial comprehensive strength	UCS	22.31	5.35	16.71	4.36
5	Rock mass brittleness index	RMBI	4.34	1.09	2.214	1.028
6	Pick consumption index	PCI	24.44	0.44	3.476	6.309
7	Pick consumption factor	PCF	57.34	26.71	42.76	6.8363
8	Specific energy	SE	2.95	1.33	3.210	0.52

7. PREDICTION OF ICR USING LINEAR AND NON-LINEAR REGRESSIONS

The main purpose of regression analysis is to obtain a mathematical relationship between one or more independent and dependent variables. Therefore, in the regression analysis, in addition to the correlation between the independent variables and the dependent variable being investigated, the type and form of the mathematical relationship are also determined [20-21]. In this study, in all linear and nonlinear regression models, the parameters of ICR, σt, σc, RQD, PCI, PCF, and SE were selected as input variables and instantaneous infiltration rate as output variable.

7.1. Linear Regression

In this study, to predict ICR, the correlation between independent and dependent variables was determined by Pearson's correlation coefficient (Table 6). Indeed, the correlation coefficient shows the severity of the linear relationship and the type of direct or inverse relationship between the independent and dependent variables.

Table 6. Pearson correlation coefficient matrix for parameters affecting the instantaneous drilling speed

Row	Variables	ICR	RQR	σ_t	UCS	RMBI	PCI	PCF	SE
1	ICR	1	-0.036	0.213	0.221	0.975	0.719	-0.934	0.220
2	RQD	-0.036	1	0.362	0.366	-0.640	-0.188	0.028	0.365
3	σ_t	0.213	0.362	1	1	0.176	0.199	-0.432	1
4	UCS	0.221	0.366	1	1	0.182	0.122	-0.438	1
5	RMBI	0.975	-0.064	0.176	0.180	1	0.831	-0.930	0.182
6	PCI	0.719	-0.188	0.119	0.117	0.831	1	-0.784	0.122
7	PCF	-0.934	0.028	-0.435	-0.435	-0.930	-0.784	1	-0.438
8	SE	0.220	0.365	1	1	0.182	0.122	0.438	1

To predict ICR, a multiple linear regression model was used with a simultaneous login method in which all independent variables were analyzed simultaneously. To perform linear regression, from 30 excavated sections in the tunnel, 22 sections were adopted for modeling, and 8 sections were selected for testing models. Based on these calculations, the linear regression equation for modeling was obtained as Eq. (7).

$$\begin{aligned} ICR = {} & 115.07 + 0.229(RQD) - 17.837(\sigma_t) \\ & - 26.53(UCS) \\ & - 7.47(RMBI) \\ & + 0.034(PCI) \\ & - 1.84(PCF) + 6.82(SE) \end{aligned} \quad (7)$$

To secure linear regression, the assumption of independence of errors, normal errors, and the linearity of independent variables should be tested. The Watson Camera Test can be used to

study the independence of errors. If the value of this statistic is in the range of 1.5–2, the assumption of the independence of errors can be considered. In addition, if the co-linear ratio is high in a regression equation, there is a high correlation between the independent variables. Therefore, despite the high coefficient of determination, the regression model may not have high credibility. The existence of this phenomenon can be examined by controlling the variance inflation factor (VIF) and tolerance. If VIF is more than 10 and the tolerance is less than 0.1, linearity between the independent variables is probable. If the VIF value is greater than 30, it indicates a serious problem. The coefficients of the regression model for the variables of research and control of the co-linear statistics of the model variables are shown in Table 7. The values of the VIF and table tolerance show that there is no coincidence between the variables included in this study.

Error frequency distribution charts and homogeneity of variances can also be plotted (Fig. 3). By comparing the error distribution diagram with the normal distribution diagram, it was found that the error distribution is almost normal because the mean value is close to zero and the standard deviation is less than one. Regarding the homogeneity diagram of variances, a standardized dispersion curve of standardized residues versus fitting values shows the optimal state because the residues are randomly dispersed in a horizontal bar around a zero residual value (Fig. 4). Table 7 presents the statistical characteristics of the regression, analysis of variance, and regression coefficients. In Table 8, the ratio of F is 73.669 and is significant at the level of 0.001. Table 8 shows the statistical characteristics of the regression and variance analyses used to predict instantaneous drilling rates. The Durbin–Watson test is a test for examining the autocorrelation between residuals in structural and regression models. The Durbin–Watson statistic ranges from 0 to 4. If there is no sequential correlation between the residuals, the value of this statistic should be close to 2. If it is close to zero, it indicates a positive correlation, and if it is close to 4, it indicates a negative correlation. In general, if this statistic is between 1.5 and 2.5, it indicates favorable results [20]. Given that the Durbin–Watson statistic obtained is a number between 1.5 and 2.5, it therefore indicates favorable statistical results, and also because it is close to 2, it indicates positive correlation.

Table 7. Regression coefficients and their tests

Linear statistics		p-value	t-value	Standard coefficients	Non-standard coefficients		Model
				Beta	Error level	B	
Tolerance	VIF	0.00	9.65	-----	11.92	115.07	Fixed
0.132	3.34	0.00	4.25	0.265	0.540	2.229	Qualitative Index of Rock Mass
0.379	3.33	0.00	3.25	-1.02	0.23	-17.837	Compressive resistance
0.533	4.45	0.007	-2.96	-1.38	8.95	-26.53	Tensile resistance
0.467	2.09	0.00	-6.98	-2.31	1.07	-7.47	Index of rock mass fracture
0.178	1.67	0.001	4.02	0.246	0.009	0.034	Blade consumption index
0.190	1.48	0.00	-9.67	-2.78	0.191	-1.84	Blade consumption factor
0.550	2.22	0.030	2.31	1.09	2.95	6.82	Special energy

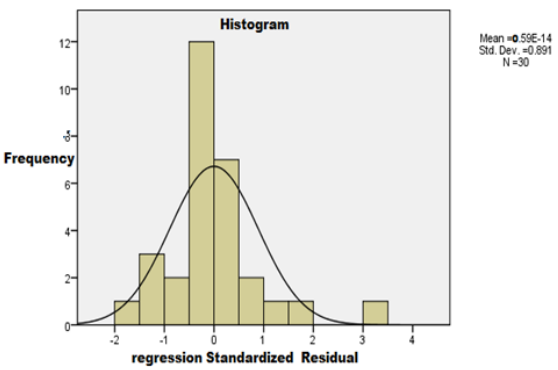

Fig. 3. Frequency distribution chart of errors.

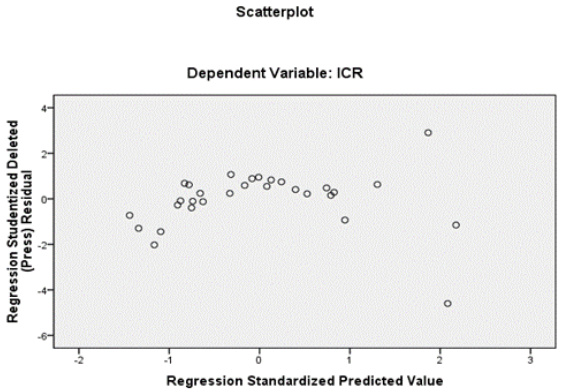

Fig. 4. Chart of homogeneity variances.

Table 8. Statistical characteristics of regression and variance analysis for predicting ICR

Model summary					
R	R2	Converted to R2	Standard error Estimation	Watson camera statistic	
0.999	0.999	0.982	0.510	2.09	
Variance analysis ANOVA					
Changes source	Sum of squares	Freedom degree	Mean of squares	Significance level	F level
Regression	313.26	7	52.23	0.00	231.01
Remaining	0.266	23	0.021	-	-
Total	313.69	30	-	-	-

7.2. Multiple Nonlinear Regressions

In many cases, a linear model is used to determine the relationship between the independent and dependent variables. In fact, the relationship between variables is not always linear and may be non-linear. Therefore, in this study, the previous data were also fitted with polynomial, power, and exponential nonlinear models, which are discussed below [21].

A: Polynomial Nonlinear Regression

After the analysis, a polynomial model was used to predict the ICR of the road-header with a R-square (R^2) of 0.994 as Eq. (8).

$$\begin{aligned} ICR = {} & 46.170 + 0.051(RQD) - 61.176(\sigma_t)^2 \\ & + 0.005(UCS)^3 \\ & + 0.013(RMBI)^4 \\ & - 4.317(PCI)^5 \\ & - 4.906(PCF)^6 \\ & - 0.001(SE)^7 \end{aligned} \quad (8)$$

B: Power nonlinear regression

In this case, a nonlinear power regression model was used to forecast the ICR of the Roadheader with a R^2 of 0.997, as shown in Eq. (9).

$$ICR = 10^{\begin{matrix}[1.540-1.867(RQD)-0.237(\sigma_t)+0.002(UCS)+ \\ 0.039(RMBI)-0.002(PCI)-0.003(PCF)+0.060(SE)]\end{matrix}} \quad (9)$$

C: Exponential nonlinear regression

A nonlinear exponential regression model was used to predict ICR of the Roadheader with a R^2 of 0.998, as shown in Eq. (10).

$$\begin{aligned} ICR = exp(& -0.845 + 0.197(\sigma t)^{-0.062} \\ & - 1.047(\sigma t)^{0.716} \\ & + 0.076(UCS)^{0.280} \\ & + 1.566(RMBI)^{0.156} \\ & + 1.064(PCI)^{-0.041} \\ & + 1.972(PCF)^{-0.518} \\ & + 1.113(SE)^{0.439}) \end{aligned} \quad (10)$$

The relationship between the predicted values of ICR and the values measured by different models for the test data can be seen in Figures 4 to 6.

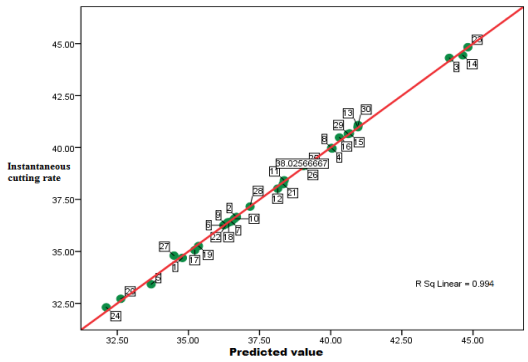

Fig. 4. Relationship ICR and its predicted values achieved by polynomial function (R2=0.994).

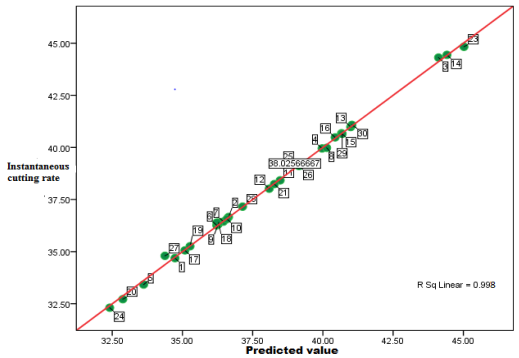

Fig. 5. Relationship between ICR and its predicted values achieved by exponential function (R2=0.998).

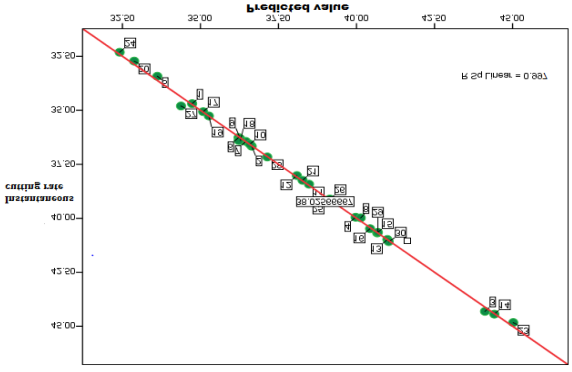

Fig. 6. Relationship between ICR and its predicted values achieved by power function (R2=0.998).

8. SELECTING BEST MODEL FOR ALGORITHM POS

To evaluate the performance of different models, compare them, and choose the best model, R^2, square root mean square of errors, mean absolute percentage error (MAPE), and VAF are determined for each model. The results show that there is a good relationship between the instantaneous drilling rate of the Roadheader and the predicted value of the parameters with a very high R^2 of the exponential functions model (R^2 = 0.998). To select the best model for estimating the drilling rate of the Roadheader machine, based on nonlinear and linear regression models, the linear regression model with the highest R^2, i.e., the value (R^2=0.999) was selected. To obtain the best model among 30 sections, we selected and calculated 8 sections for the predicted value and 22 sections for the measured value. Table 9 shows the best model for the PSO algorithm based on the determined effective factors.

Table 9. Selection of the best model for the PSO algorithm based on the determined effective factors

Model	R^2	RMSE	MAPE	VAF
Linear regression	0.999	0.612	0.07212	99.80
Nonlinear regression of polynomial function	0.994	0.985	0.07717	86.1
Nonlinear regression of power function	0.997	0.885	0.07814	87.1
Nonlinear regression of exponential function	0.997	0.945	0.07316	88.1

9. OPTIMIZATION OF ICR USING THE ALGORITHM PSO (PARTICLE MASS OPTIMIZATION ALGORITHM)

Selecting the appropriate input parameters is an important part of evolutionary intelligence algorithms and analytical models. Using the analysis of the main components, we can determine the parameters affecting a physical phenomenon. In this research, the input and output parameters for 30 considered sections as the case study are RQD, UCS, σt, RMBI, PCI, PCF, SE, as input parameters, and ICR as the output parameter.

To model the issue, all the values of the parameters must be recorded so that they can be called up from the function when needed. At this stage, the definition and implementation of the initial values are performed as shown in Figure 8.

In this section, we specify the target function, the number of unknown variables, the structure of the unknown variables, and the upper and lower limits of the variables. The relationship obtained from the linear regression model was used to predict the ICR in the PSO algorithm. The linear regression model was implemented several times with parameter variations. This trend continued until the algorithm reached the appropriate convergence. The target function is ICR. According to Figure 7, the results of the PSO algorithm show that to obtain the optimum level of the target function for a rock section with a σc of 51.78 MPa and a RQD of 33.09%, ICR of the Roadheader is equal to 36.41 m3/h. In Figure 8, the horizontal axis represents the number of function evaluations or NFEs.

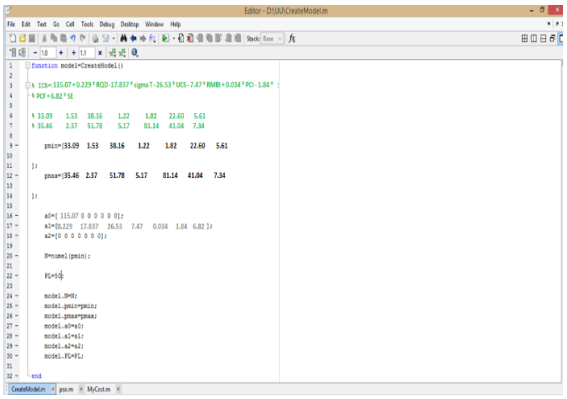

Fig. 7. Modeling of input parameters for optimization of the considered tunnel.

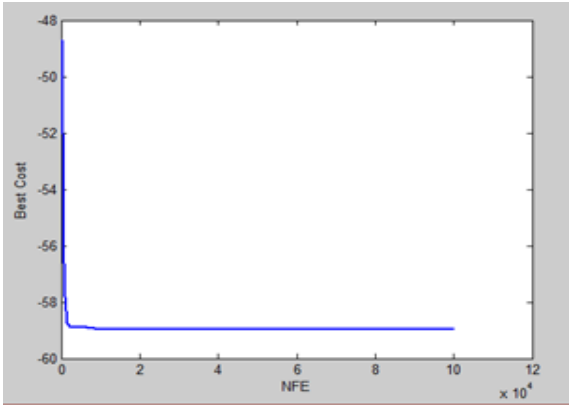

Fig. 8. Output of optimization issue of ICR of Roadheader as a diagram.

10. ANALYZING THE SENSITIVITY OF THE NEURAL NETWORK MODEL USING THE COSINE FIELD METHOD

Sensitivity analysis is the study of the effect of output variables on the input variables of a statistical model. In other words, it is a way to change the inputs of a systematic statistical model that can predict the effects of these changes in the output of the model. The cosine field method is used to determine the ratio between the involved parameters. In this section, the intensity of the relationship between the ICR and the input

parameters is determined. The results are illustrated in Table 10.

Table 10. Analysis of the sensitivity of the input parameter model to the instantaneous drilling rate using the cosine field method

Input parameter	Sensitivity level to the instantaneous drilling rate
Qualitative index of rock mass (%)	0.999
Tensile resistance (MPa) (σt)	0.996
Single-axial compressive resistance of the rock (UCS) (MPA)	0.997
Fragility index of the rock mass (RMBI)	0.995
Partition consumption index (PCI)	0.995
Partition consumption factor (PCF)(m3/pick)	0.997
Specific energy (SE) (MJ/M3)	0.992

As shown in Figure 9, σt, UCS, RQD, and PCF are the most important parameters affecting ICR. In addition, the influence of RMBI is relatively strong. Parameters such as SE and PCI are more sensitive to input parameters than ICR.

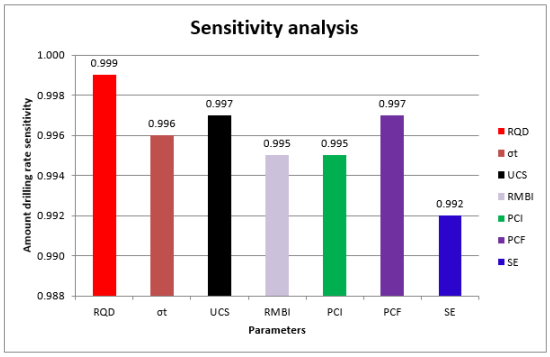

Fig. 9. Intensity level of the instantaneous drilling rate relationship with each input parameter.

According to Table 10, the results were analyzed by SPSS Software to measure the intensity level of ICR relationship with each of the input parameters.

The effective parameters in determining ICR for the case study were evaluated by cosine field sensitivity analysis, which are as follows:

A: The computational error rate is almost zero, indicating that the trained network has reached the desired convergence.

B: The rate of advancement for these tunnels from the input parameters is strongly influenced by the geomechanically properties of the rock.

11. CONCLUSION

This research presented a model to predict the performance of Roadheader machine in underground coal mines based on characteristics and geotechnical parameters of rock. In this regard, a case study including 30 sections along a tunnel in Parvadeh No. 1 underground coal mine was taken to account. Analyses were performed based on linear regression and nonlinear regression, and the ANF system to predict instantaneous cutting rate (ICR) of Roadheader. Based on the introduced approach, prediction of ICR in various geotechnical conditions is available for tunnels and roadways in underground coal mines. The prediction was conducted using the neural network and PSO algorithm. The best linear regression model was selected according to the performance evaluation methods. To achieve the best model made by the neural network, the coefficient of determination (R^2), performance index, root mean square error, and mean absolute error percentage were used. Finally, to select the best model for estimating ICR, the linear regression system has a better estimation and higher accuracy than nonlinear regression. The mean squared error for the linear regression model is less than that for the other two models, and the correlation coefficient in linear regression is greater than that in nonlinear regression. This is while linear regression has a determination coefficient R2 = 0/999, and this value has tremendous reliability. Finally, by inserting the linear regression results in the PSO algorithm, it is shown that to obtain the optimum target function for the rock mass transfer with a UCS of 1.68 MPa and RQD of 33.09%, ICR of the Roadheader equals 33.11 cubic meters per hour. Considering specific energy (SE) as an important parameter in determining the drilling rate, so this parameter should be considered for determination of ICR. Here, the results of the algorithm show that for 34.21 of the consumable partition, SE should be 6.15 MJ/m3.

REFERENCES

[1] Ebrahim Abadi, A. (2012). Introducing a Model for Road headers' Performance Prediction Based on the Specific Energy and the Angle between Tunnel Axis, Quarterly Scientific - Research Journal of Environmental Geology, Year 6, Issue 20 - Shapa 2008-4250.

[2] Ebrahimabadi, A., Goshtasbi, K., Shahriar, K., and Cherghi, Seifabad, M. (2011). Predictive Models for Roadheaders' Cutting Performance in Coal Measure Rocks", YERBILIMLERI Journal, Vol. 32, No. 2, pp 89-104.

[3] Ebrahimabadi, A. (2012). Stability Analysis and Optimum Support Design of Tunnel No. 1 of Central Mine in Tabas Coal Mine Project", ITA-AITES World Tunnel Congress and 38th General Assembly (2012), Bangkok, Thailand, 8p.

[4] Ebrahimabadi, A., Azimipour, A and Bahreini, A. (2016). Prediction of Roadheaders' performance using artificial neural network approaches (MLP and KOSFM)", Tunneling and Underground Space Technology, Volume 59, Pages 127-133.

[5] Comakli, R., Sair Kahraman, S and Balci, C., (2014). Performance prediction of Roadheaders in metallic ore excavation", Tunneling and Underground Space Technology, 38-45.

[6] Bilgin, N. and Ocak, I. (2010). Comparative studies on the performance of a Roadheader, impact hammer and drilling and blasting method in the excavation of metro station tunnels in Istanbul", Tunnelling and Underground Space Technology, Volume 25, Issue 2, Pages 181-187.

[7] Bilgin, N., Dincer, T., Copur, H and Erdogan, M. (2004). Some Geological and Geotechnical Factors Affecting the Performance of a Roadheader in an Inclined Tunnel", Tunnelling and Underground Space Technology, Vol 19, Elsevier, pp. 629-636.

[8] Eftekhari, S. M. and Bastami, M. (2020). Effect of the Replacement of Cutting Tools on the Performance of TBM in Tehran Metro Line 6. *Journal of Analytical and Numerical Methods in Mining Engineering*, *10*(24), 63-76. doi: 10.29252/anm.2020.13703.1438.

[9] Mokhtarian, M. , Eftekhari, M. and Baghbanan, A. (2014). Application of Principal Component Analysis in Prediction of Penetration Rate of TBM Using Artificial Neural Networks. *Journal of Analytical and Numerical Methods in Mining Engineering*, *3*(6), 33-43.

[10] Khodaee Ashestani, S. , Chakeri, H. , Darbor, M. , Khoshzaher, E. and Bazargan, S. S. E. (2023). Estimating Penetration Rate of Excavation Machine Using Geotechnical Parameters and Neural Networks in Tabriz Metro. *Journal of Analytical and Numerical Methods in Mining Engineering*, *13*(37), 1-9. doi: 10.22034/anm.2023.20414.1604.

[11] Bilgin, N and Balci, C. (2005). Performance Prediction of Mechanical Excavators in Tunnels, Training Course of Tunnel Engineering, Istanbul Technical University, Turkey.

[12] Copur, H., Ozdemir, L and Rostami, J. (1998), "Roadheader Applications in Mining and Tunneling Industries", The Mining Engineering, pp. 38-42.

[13] Hosseini, A. , Najafi, M. and morshedy, A. H. (2022). The effect of technical parameters of cross-measure boreholes methane drainage method on the amount of exhaust gas (Case study: Tabas Parvadeh coal mine No.1). *Journal of Analytical and Numerical Methods in Mining Engineering*, *12*(30), 79-89. doi: 10.22034/anm.2022.2570.

[14] Hosseini A, Najafi M (2021) Determination of Methane Desorption Zone for the design of a drainage borehole Pattern (Case Study: E4 Panel of the Tabas Mechanized Coal Mine, Iran). Rud Zb 36:61–75.

[15] Hosseini A, Najafi, M and Morshedy, AH. (2022) Determination of suitable distance between methane drainage stations in Tabas mechanized coal mine (Iran) based on theoretical calculations and field investigation. J Min Inst 258:1050–1060.

[16] Hosseini, A., Najafi, M., Shojaatlhosseini, SA and Rafiee, R. (2017) Determination of a suitable extraction equipment in mechanized longwall mining in steeply inclined coal seams using fuzzy analytical hierarchy method (Case study: Hamkar coal mine, Iran). J Min Environ 8:487–499.

[17] Dosco Overseas Engineering Ltd, (2008), Newark Nottinghamshire, England, www.dosco.co.uk.

[18] Rostami, J., Ozdemir, L and Neil, D., M. (1994), "Roadheader Performance Optimization for Mining and Civil Construction", Proceedings of 13th Annual Technical Meeting of the Institute of Shaft Drilling Technology (ISDT), Las Vegas, pp. 1-17.

[19] Thuro, K and Plinninger, R.J. (1999), "Roadheader Excavation Performance – Geological and Geotechnical Influences", 9th ISRM Congress Paris, Theme 3: Rock Dynamics and Tectonophysics/Rock Cutting and Drilling, pp.25-28.

[20] Mostowfi, N. (2011), learn how to use MATLAB", Department of Chemical Engineering, Tehran University.

[21] B. H. G. Brady and E. T. Brown, (1993), "Rock Mechanics for Underground Mining", Second Edition.

[22] S. Hamekhoni, and Ramzan Ali Royaei, (2022), The Effect of Cultural Factors on Cost Stickiness, Financial Accounting and Auditing Research, Volume 14, Number 54, Pages 159-178.

Vol. 15, No. 45, Winter 2026, pages 13-21

Journal of Analytical and Numerical Methods in Mining Engineering

Journal home page: http://anm.yazd.ac.ir/

Research article

Rock Load Height Prediction for Large-Scale Caverns Using Numerical Analysis

Abolfazl Abdollahipour[1]*

1- School Of Mining Engineering, College Of Engineering, University Of Tehran, Tehran, Iran

*Corresponding author: E-mail: *abdollahipour@ut.ac.ir*

(Received: *January 2025*, Accepted: *April 2025)*

DOI: 10.22034/ANM.2025.22613.1656

Keywords

Rock load height

Cavern stability analysis

Cavern Roof Displacement

Numerical analysis

Support design

Abstract

Determination of rock load values plays a crucial role in the stability analysis and design of underground structures, particularly in ensuring the safety and cost-effectiveness of support systems. Rock load height serves as a vital parameter for determining the required support in underground openings. Over the years, numerous researchers have developed various methods to estimate rock load height, often based on parameters such as rock quality, opening width, and uniaxial compressive strength. However, the combined effects of additional key parameters, including the ratio of horizontal to vertical stress (K ratio) and overburden height, have not been thoroughly investigated in a unified framework. This study addresses this gap by incorporating these parameters to propose a new empirical relationship for estimating rock load height. Numerical analyses were performed using a safety factor contour of 2.0 to evaluate the rock load heights in cavern roofs under diverse conditions. The results of this comprehensive analysis were compared with existing methods, demonstrating good agreement and validating the reliability of the proposed approach. The new relationship offers a significant advantage by accounting for the influence of varying overburden heights and horizontal-to-vertical stress ratios, thus providing more precise estimations tailored to site-specific conditions. Furthermore, the study introduces a novel equation that links vertical displacement in the cavern roof to rock load height. This innovative approach provides a practical tool for integrating monitoring data into stability assessments. By bridging theoretical insights with real-world applications, the proposed methodology advances the understanding and prediction of rock load behavior, ensuring safer and more effective underground design practices.

1. INTRODUCTION

Predicting rock load height in large-scale caverns is crucial for ensuring stability and safety during construction and operation. Numerical analysis plays a significant role in this prediction by simulating various geological and mechanical conditions. Numerical analysis provides a robust approach to estimating rock load behavior by integrating geomechanical parameters, geometrical factors, and advanced modeling techniques. Key geomechanical parameters such as Rock Mass Rating (RMR), uniaxial compressive strength (UCS), and material constants significantly influence numerical predictions [1,2]. Additionally, the Geological Strength Index (GSI) and the ratio of saturated UCS to in-situ stress (R/σ) are crucial for understanding deformation behavior [3]. Geometrical factors, including the span, height, and depth of caverns, as well as their spacing, play a vital role in stability assessments [4,5]. Overburden depth and lateral stress coefficients are particularly influential in vertical displacement predictions [6]. Recent numerical studies further emphasize that rock-mass behavior, stress conditions, and modeling strategy

strongly influence stability predictions. For example, comparisons of 2D and 3D tunnel analyses under static and seismic loading show that weaker or jointed masses exhibit substantially different displacement patterns depending on dimensionality [7]. Similar sensitivity is observed in room-and-pillar systems, where numerically derived pillar strengths and optimal dimensions deviate from empirical formulas—especially under dynamic loads [8]. In large underground water tunnels, numerical assessments have also shown that support demand correlates closely with plastic-zone development in weak rock masses [9]. Together, these studies highlight the need for rock-load estimation methods that explicitly incorporate stress anisotropy and overburden effects—an issue addressed by the unified numerical framework proposed in this work. Various numerical methods have been employed to improve prediction accuracy. The Hoek-Brown criterion, combined with Monte Carlo simulations, enables dynamic estimations of rock mass mechanical properties [1]. Machine learning approaches such as Artificial Neural Networks (ANN) effectively predict maximum horizontal displacement using large numerical modeling datasets [2]. Additionally, fuzzy logic (FL) and statistical analysis (SA) offer reliable methodologies for estimating vertical displacements, enhancing predictive accuracy[6].

The excavation method significantly impacts rock load behavior. Techniques such as partial excavation with reserved rock pillars and various support systems (e.g., bolts, shotcrete lining) influence deformation and stability [5,10]. Comparative numerical simulations help assess the effectiveness of different support structures in mitigating deformation [10].

Several large-scale projects have validated numerical models through real-world applications. For instance, the Baihetan Hydropower Station successfully utilized probabilistic stability assessments and dynamic simulations, confirming the alignment of numerical predictions with field data [1]. Similarly, studies on the Ayalon Cave demonstrated the importance of cover height in stability assessments, as numerical predictions corresponded well with observed roof collapses.

Predictive models are developed from extensive numerical simulations incorporating multiple geomechanical and geometrical factors [2,6]. Empirical validation through case studies, such as those in the Carrara basin and the Etzel Field Test, further ensures the reliability of numerical predictions [11]. The integration of numerical analysis with field data validation enhances predictive accuracy, contributing to safer and more efficient underground construction. Continuous advancements in modeling techniques and data-driven approaches will further improve the understanding of rock load height behavior in large-scale caverns.

Terzaghi [12] proposed that the rock load height H_p is the height of loosening zone over a tunnel roof, which is likely to load the steel arches (Fig. 1). According to Terzaghi's theory, rock load increases with the opening size. A limitation of Terzaghi's theory is that it may not be applicable for tunnels wider than 6 m [1].

Protodyakonov assumed that the pressure arch on the tunnels is a parabolic arch [13]. He proposed the following relation for estimating the rock load used in urban railways in Moscow:

$$H_p = \frac{b}{2f} \tag{1}$$

where H_p is the parabolic arch height, b is the parabolic width and f is the strength factor (Protodyakonov coefficient) that depends on the ground characteristic, approximately one tenth of the uniaxial compressive strength of the host rock around the tunnel. The parabolic width is calculated from the following equation:

$$b = B + 2H.\tan(45 - \frac{\phi}{2}) \tag{2}$$

where B is the tunnel width; H is the tunnel height and ϕ is the internal friction angle of rocks. In cohesionless gravel and sandy grounds, Protodyakonov f equals to $tan(\phi)$.

Barton et al. [14] proposed the empirical relation for ultimate rock load based on the NGI-Q classification system.

$$p_v = (0.2/J_r)Q^{-1/3} \tag{3}$$

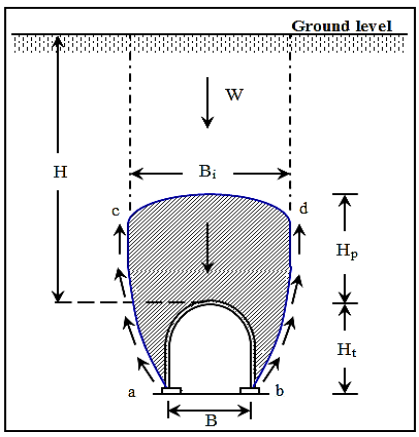

Fig. 1. Terzaghi's rock-load concept in tunnels.

where Q is the Q value, J_r is the joint roughness coefficient, p_v is ultimate roof rock load in MPa. They further suggested that if the number of joint sets is less than three, Eq. (3) should be expressed as:

$$p_v = \frac{0.2.J_n^{1/2}}{3.J_r}.Q^{-1/3} \quad (4)$$

The Terzaghi scheme was modified by using the RQD [15]. In the modified scheme, a reduction was made since the effect of water was overestimated in the Terzaghi scheme. Rose's observations indicated that water had little effect on the rock load H_p. Other authors [16] have compared support pressure measured from tunnels and caverns with estimates from Terzaghi's rock load theory and found that the support pressure in rock tunnels and caverns does not increase directly with excavation size as assumed by Terzaghi.

Unal [17] proposed the following relation for estimating the rock load (p_v) using the RMR for openings with a flat roof:

$$p_v = \left[\frac{100 - RMR}{100}\right].\gamma.B \quad (5)$$

where γ is the unit weight of rock and B is the tunnel width.

Bhasin and Grimstad [18] suggested the following relation for predicting rock load (p_v in kPa) in tunnels through poor rock masses (say Q<4):

$$p_v = \frac{40B}{J_r}Q^{-1/3} \quad (6)$$

where B is the diameter or span of the tunnel in meters. Eq. (6) shows that the rock load increases with tunnel size B in poor rock masses.

According to the Russian method, rock load height consists of the structural collapse zone depth, the blasting crushed zone depth, and depth of elasto-plastic collapse zone [19]. The Russian method suggests that the total rock load height is determined by the following equation:

$$H_p = k_1 B \quad (7)$$

Considering different engineering and geological conditions, several parameters in underground openings and statistical analysis of each calculated depth zone coefficient k_1 have been determined and are presented in Table 1.

Table 1. Coefficient k_1 for Russian method

Protodyakonov coefficient (f)	K_1
≥15	0-0.05
14-10	0.05-0.1
9-7	0.1-0.15
6-5	0.15-0.2
4	0.2-0.3
3-2	0.3-0.4

In heavy jointed or heavily altered rock mass, the coefficient k_1 must be determined by experiment, and in the first stages of cavern design, it is possible to use the proposed value in the table, but it must be multiplied by 1.5 [19]. Also, for Protodyakonov coefficients less than 4, the effect of large tunnel or cavern depth is considered by a correction factor k_2, which must be multiplied in H_p. Table 2 presents k_2 for different depths.

Table 2. Correction factor for Russian method [19]

Depth[m]	≤ 100	250	500
K_2	1.0	1.3	1.5

Other researchers have used heuristic methods to predict roof pressure [20].

Abdollahipour and Rahmannejad [21] showed that the horizontal to vertical stress ratio and the deformation modulus are two important parameters in underground excavations stability. They used these parameters along with several other parameters in a later study [22] and proposed an equation to estimate the displacement in cavern sidewalls. Another study has investigated the effect of adjacent caverns using the plastic zone formed between two adjacent caverns [23]. Effects of these two parameters (horizontal to vertical stress ratio and deformation modulus), geometry, and depth of opening on rock load height have never been studied altogether. In this study it is made to consider the effect of all these features on the rock load height for a single cavern.

2. RESEARCH METHODOLOGY

In this study, a series of numerical analyses was performed to estimate rock load height for the design of a cavern lining. The two-dimensional FEM program, Phase^2 [24] has been used to model and analyze the rock load height. The following simplifications and assumptions have been made:

The surrounding rock mass is homogeneous and continuous, the joint effect is considered using

the equivalent deformation module, E using a model proposed by Sitharam [25].

The initial in situ stress is uniformly distributed within the computational domain, and the two principal stresses (minor and major principal stresses) act in horizontal and vertical directions; the out-of-plane stress is the intermediate principal stress. The mechanical properties of rocks into which caverns have been excavated are presented in Table 3. The required parameters, when not present, were obtained using the RocLab program. It is assumed that the rock mass obeys the Hoek-Brown criterion. A single horseshoe-shaped cavern was utilized as the default for all analyses. An expansion factor of 5 with "Box Boundary Type" has been used in Phase^2 to ensure that the boundary is far enough away to simulate "infinite" or far-field conditions, and doesn't influence the results near the excavations. The "Increase Mesh Element Density" option has been used to increase the element density around the caverns. This was done to improve the accuracy of the displacement and plastic depth results. When the mesh was generated, all nodes on the external boundary were given a fixed, zero displacement boundary condition. Figure 2 shows a cavern of 33×52m cross-section modeled in Phase^2 as described above.

In all numerical models conducted, fixed boundary conditions were applied in all directions, as the model is located at a great depth and its upper surface does not represent the ground surface. To assess the influence of boundary conditions, several comparative analyses were performed using both roller and fixed boundaries, revealing no significant difference in the model's response. This was attributed to the sufficient distance between the boundaries and the excavation zone. Moreover, given that over 1000 numerical simulations were conducted and the software's default settings applied fixed boundaries, this approach was adopted to streamline the modeling process and enhance computational efficiency without compromising result accuracy.

Table 3. Mechanical properties of rock masses

Reference	ν [-]	E [MPa]	UCS [MPa]	S [-]	m_b [-]	RMR [-]
[26]	0.33	3162	113.4	0.0007	1.28	35
[27]	0.3	4350	70	0.0013	2.12	47
[27]	0.27	11900	100	0.0054	3.546	54
[26]	0.27	13335	119	0.007	6.01	60
[27]	0.26	28700	85	0.11	5.94	68
[28]	0.25	56000	340	0.0357	10.961	75

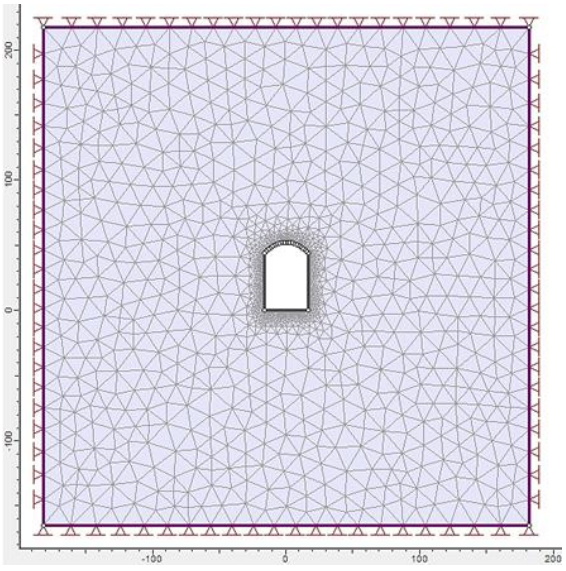

Fig. 2. A horseshoe cavern of 33×52m cross section modeled in Phase 2.

3. NUMERICAL ANALYSIS

A horseshoe cavern with cross-section dimensions of 10×15, 18×30, 33×52, 60×60m was selected, six different horizontal to vertical stress ratios i.e., k= 0.33, 0.5, 1, 1.5, 2, 2.5 have been used in calculations for each rock type, and four different overburden depths of H=100, 200, 300 and 400m have been considered.

The size of the relaxed zone (equivalent to the plastic zone in an elasto-plastic analysis) occurred by tunnel excavation could be found by finding the contour of safety factor of 2.0 or 3.0 [29]. Also, a safety factor contour of 2.0 has been used successfully to design lining support for a 2-arch tunnel [30]. In addition to that Hoek et al. [31] proposed to use the same value of safety factor contour. Therefore, the contour of safety factor of 2.0 has been used in numerical analyses to estimate the height of relaxed zone in cavern roof. Figure 3 shows the height of relaxed zone on the roof of a cavern obtained from safety factor

contour of 2. Figure 4 shows the vertical and horizontal displacements in this model.

Nearly 1000 cases have been computed altogether. Eq. (8) has been fitted on the results of numerical analyses.

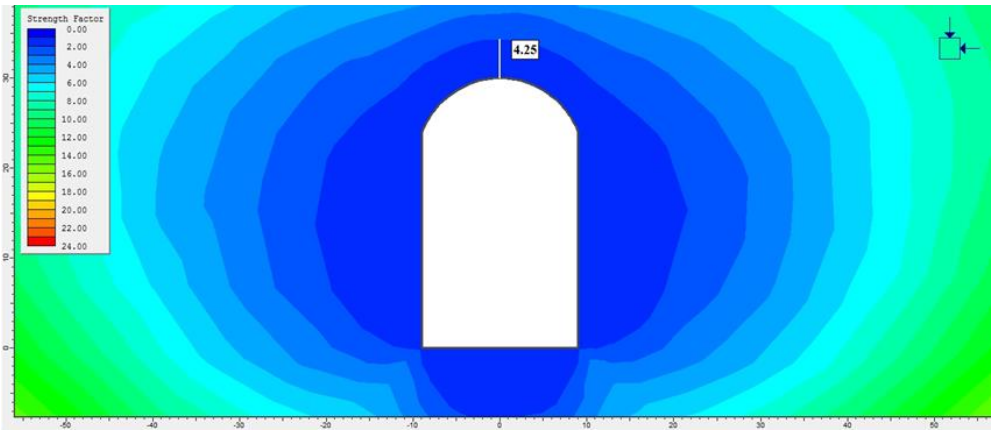

Fig. 3. Safety factor contours around a 18×30m cavern in a rock with RMR=35.

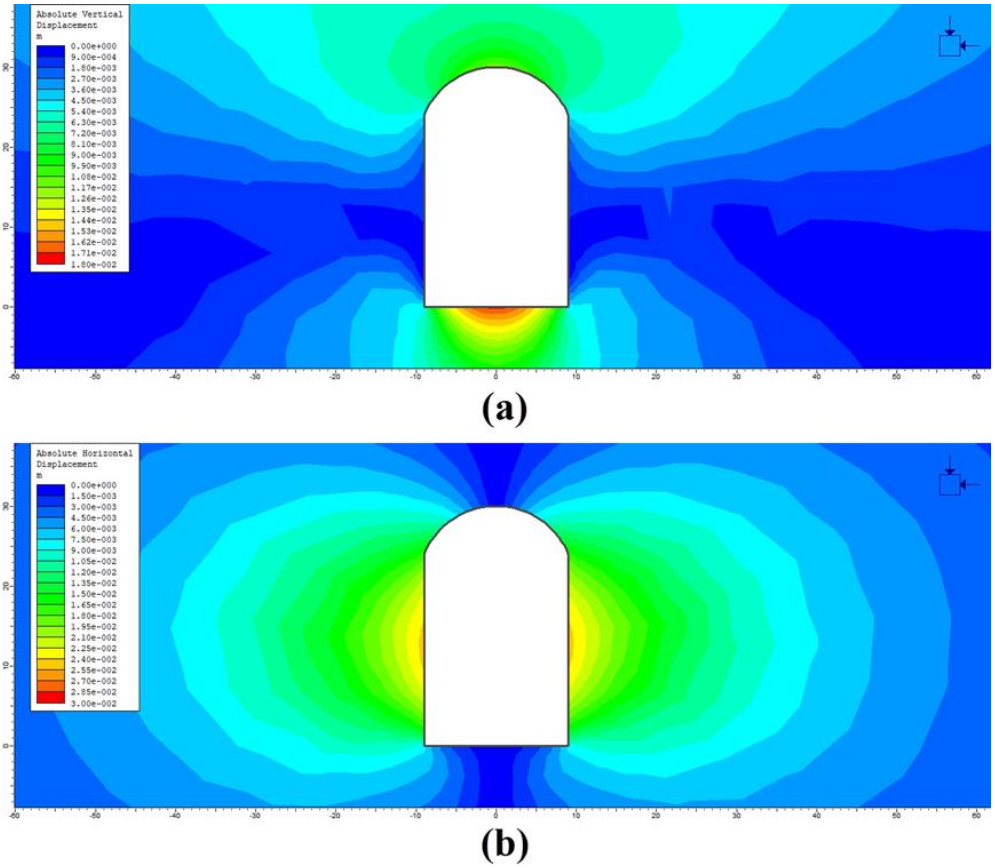

Fig. 4. Displacement contours around a 18×30m cavern in a rock with RMR=35, a) vertical displacement, b) horizontal displacement.

Results of regression are presented in Figure 5. The determination coefficient of this linear model, R^2, is 90.43.

$$H_p = \left(0.0066\times(100\text{-RMR})\times B\right) + 0.0115\times KH\text{-}3.35 \quad (8)$$

where H_p (m) is rock load height, B (m) is cavern width, K (-) is the horizontal to vertical stress ratio, and H is overburden depth (m).

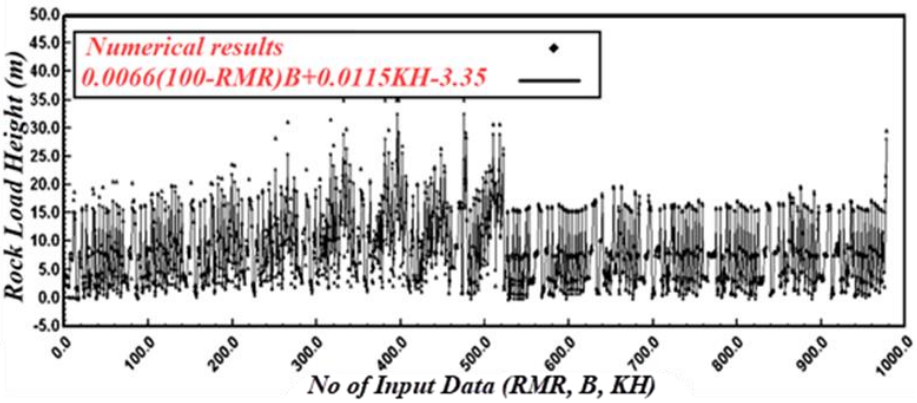

Fig. 5. Regression results of proposed equation (Eq. 8).

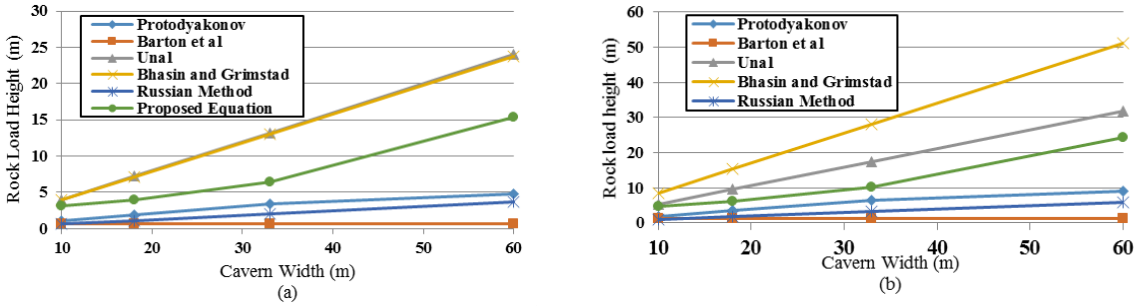

Fig. 6. Comparison of new and existing equations for two cases: a) H=200m, RMR= 60 and K=1, and b) H=400m, RMR= 47 and K=1.

4. RESULTS AND DISCUSSION

To evaluate the proposed equation, the rock load height results of the proposed equation (8) are compared with aforementioned empirical equations in the introduction. Other needed parameters of empirical equations are presented in Table 4.

A large number of numerical analyses have been carried out. Results showed that all equations have a similar trend with different slopes. Figure 6 shows the resulting curves of numerical analyses for two different overburden heights. The vertical axis stands for rock load height and the horizontal axis represents the cavern width.

Table 4. Mechanical parameters of rocks

RMR	Q	J_r	J_n	φ	f
35	0.41	1	12	28.3	11.34
47	1.56	1.5	6	32.5	7
54	3.40	1.5	6	36.5	10
60	6.61	2	4	40.2	11.9
68	16.08	3	3	41.4	8.5
75	35.01	4	1	46.5	34

As it can be seen in Figure 6 the results of the proposed equation are in accordance with other empirical methods. While Eq. (8) proves to be in reasonable limits, it has the following advantages in comparison with other methods:

Unlike some other methods, the required parameters in proposed equation are common field data that are always available and easy to obtain or even estimate.

Eq. (8) estimates the rock load height considering the cavern depth and the field stress (overburden height and horizontal to vertical stress ratio), which makes it more logical in estimating rock load height than other equations that do not consider these parameters (see Table 5).

Horizontal to vertical stress ratio of 1.5 along with RMR= 54 in 4 different overburden depths of 100, 200, 300 and 400m have been considered in Table 5. It shows the advantage of proposed equation in estimating the rock load. The proposed equation has estimated different rock load heights for different conditions. Other methods have predicted rock load heights according to the opening width, except for Barton et al. which depends on rock quality (Q) only.

Table 5. Rock load height of different methods for K=1.5 and RMR=54. (Units are in meters)

H	B	Barton et al.	Protodyakonov	Unal	Bhasin and Grimstad	Russian Method	Proposed Equation
100	33	2.68	1.29	15.18	21.69	1.65	6.71
200	33	2.68	1.29	15.18	21.69	1.65	8.03
300	33	2.68	1.29	15.18	21.69	1.65	9.62
400	33	2.68	1.29	15.18	21.69	1.65	11.52
100	60	2.68	1.00	27.60	39.43	3.00	16.01
200	60	2.68	1.00	27.60	39.43	3.00	19.17
300	60	2.68	1.00	27.60	39.43	3.00	22.95
400	60	2.68	1.00	27.60	39.43	3.00	27.47

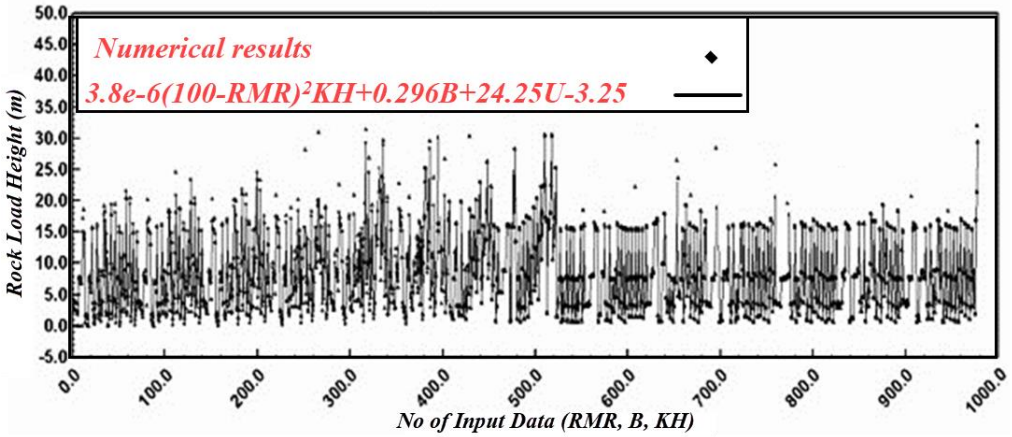

Fig. 7. Regression results for proposed equation (Eq. 9).

5. ESTIMATING ROCK LOAD HEIGHT USING VERTICAL DISPLACEMENT

In many practical cases, the vertical displacement of the caverns' roof is available; establishing a relationship between this displacement and the rock load height one should be able to estimate the rock load pressure on the roof. Therefore, vertical displacements of the aforementioned numerical analyses have been derived. Eq. (9) has been fitted to the results of numerical analyses (Fig. 7). The determination coefficient, R^2, is 90.1.

$$H_p = \left[3.8\times(100\text{-RMR})^2\times KH\right]\times10^{-6}+ 0.296B+24.25U-3.25 \quad (9)$$

where U is roof displacement (m) (always as a positive value). The rock load height can be estimated more accurately for low overburden depth i.e. low vertical stresses. Eq. (9) can be useful when monitoring data are available so that the rock load height and subsequently the rock load pressure can be estimated quickly. Given that roof displacement is often available from monitoring systems, this equation allows for a practical and efficient estimation of rock load pressure. This estimation is particularly useful for low overburden depths, where the accuracy is higher. The results can be directly applied in support design, including shotcrete thickness and rock bolt length calculations. Results can then be applied in support design to calculate shotcrete or lining thickness (for example, Lame's thick-wall cylinder theory [32] which requires roof pressure), rock bolt length, etc.

6. CONCLUSIONS

This study presented a comprehensive investigation into rock load height prediction for large-scale caverns using numerical analysis. Existing empirical methods were reviewed, and a systematic approach was proposed to estimate rock load height based on numerical simulations. The rock load height was determined using a safety factor contour of 2.0, corresponding to the relaxed zone in the cavern roof. A new empirical equation was derived from extensive numerical analyses, incorporating key parameters such as cavern width, overburden depth, and the horizontal-to-vertical stress ratio. The proposed equation was validated against existing methods, demonstrating a strong correlation and improved reliability in various geological conditions.

The advantages of the proposed equation include its reliance on commonly available field parameters, making it more practical for engineering applications. Unlike some previous methods, the equation considers the effect of overburden depth and horizontal stress ratio, allowing for a more realistic estimation of rock load height. Furthermore, a secondary equation was introduced to estimate rock load height based on vertical roof displacement, providing a useful tool for integrating monitoring data into stability assessments. This approach enhances the practical applicability of the study by enabling real-time estimation of rock load pressure, which is essential for optimizing support design.

This research advances the understanding of rock load behavior in underground caverns, bridging theoretical analysis with practical implementation. The findings contribute to safer and more cost-effective underground design practices by improving rock load estimations and support system efficiency. Future work could focus on refining the proposed equations using additional case studies and incorporating three-dimensional numerical modeling to further enhance prediction accuracy.

REFERENCES

[1] Liu G, Zhou C, Feng K, Jiang Q, Li S, Bao H, et al. Probabilistic evaluation method for the stability of large underground cavern considering the uncertainty of rock mass mechanical parameters: A case study of Baihetan underground powerhouse project. Eng Geol 2024;340:107660. https://doi.org/10.1016/j.enggeo.2024.107660.

[2] Rajabi M, Rahmannejad R, Rezaei M, Ganjalipour K. Evaluation of the maximum horizontal displacement around the power station caverns using artificial neural network. Tunnelling and Underground Space Technology 2017;64:51–60. https://doi.org/10.1016/j.tust.2017.01.010.

[3] Luo S-T, Yang F-J, Zhou H, Zhang C-Q, Wang X-H, Lü T, et al. Multi-index prediction method for maximum convergence deformation of underground powerhouse side wall based on statistical analysis. Yantu Lixue/Rock and Soil Mechanics 2020;41:3415–24.

[4] Li X, Zhu W, Chen W, Wu K. Determining weight of factors in stability analysis of underground caverns by analytic hierarchy process. Chinese Journal of Rock Mechanics and Engineering 2004;23:4731–4.

[5] Tao L, Huang L, Shi C, Zhang N. Deformation Control Standards for Super-Large-Span Flat Underground Cavern. Tunnel Construction 2022;42:9–15.

[6] Rezaei M, Rajabi M. Vertical displacement estimation in roof and floor of an underground powerhouse cavern. Eng Fail Anal 2018;90:290–309. https://doi.org/10.1016/j.engfailanal.2018.03.010.

[7] Hashemi, M. and Hajiazizi, M. (2023). The effect of two-dimensional and three-dimensional modeling on the seismic response of tunnels in the jointed rock mass by pseudo-static analysis. *Journal of Analytical and Numerical Methods in Mining Engineering*, *13*(36), 61-78. doi: 10.22034/anm.2023.18536.1557.

[8] Heidarnejad, M. , Azhari, A. , Ahour, M. and Ghasemi,Ḏ. (۲۰۲۲). Determining the optimal dimensions of the pillars under static and dynamic loads in room and pillar mines (Case study: Tabas central coal mine). *Journal of Analytical and Numerical Methods in Mining Engineering*, *12*(31), 35-45. doi: 10.22034/anm.2022.2632.

[9] Behzadinejad, H. , Faramarzi, L. and Darbor, M. (2017). Stability Analysis and Support System Design of Penstock Tunnels Bifurcation with Headrace Tunnel of Rudbare-Lorestan Dam Project. *Journal of Analytical and Numerical Methods in Mining Engineering*, *7*(13), 113-123. doi: 10.29252/anm.7.13.113.

[10] Liu JH, Zhu WS, Li SC. Numerical Analysis of 3-D FLAC on Supporting Effects of Underground Caverns Surrounding Rockmass of Xiao Lang Di Key Water Control Project, 2006, p. 1467–72. https://doi.org/10.4028/0-87849-989-x.1467.

[11] Vagnon F., Bonetto S.M.R., Caselle C., Ferrero A.M., Umili G., Vianello D., et al. A comprehensive study on natural and induced stress state in large underground marble quarry. ISRM International Symposium - EUROCK 2020, 2020.

[12] Terzaghi K. Rock defects and loads on tunnel support. In: Proctor R V., White TL, editors. Introduction to Rock Tunnelling with Steel Supports, Youngstown, Ohio: Commercial Sheering & Stamping Co.; 1946.

[13] Huang X, Zhang Z. Stress arch bunch and its formation mechanism in blocky stratified rock masses. Journal of Rock Mechanics and Geotechnical … 2012.

[14] Barton N, Lien R, Lunde J. Engineering classification of rock masses for the design of tunnel support. Rock Mechanics 1974.

[15] Rose D. Revising Terzaghi's Rock Load Coefficients. 23rd U.S. Symposium on Rock Mechanics SME/AIME, New York, U.S.A.: 1982, p. 953–60.

[16] Jethwa J, Dube A. A Classification System for Support Pressure in Tunnels and Caverns. Journal of Rock Mechanics and Tunnelling Technology 1995:13–24.

[17] Unal K. Design guidelines and roof control standards for coal mine roofs. Pennsylvania State University, 1983.

[18] Bhasin R, Grimstad E. The use of stress-strength relationships in the assessment of tunnel stability. Tunnelling and Underground Space Technology 1996.

[19] Mastokov VM. Large underground openings section. Moscow: Nedra publication; 1974.

[20] Feng X, Wang Y, Yao J. A neural network model for real-time roof pressure prediction in coal mines. International Journal of Rock Mechanics and Mining Sciences 1996.

[21] Abdollahipour A, Rahmannejad R. Sensitivity analysis of influencing parameters in cavern stability. Int J Min Sci Technol 2012;22:707–10. https://doi.org/10.1016/j.ijmst.2012.08.020.

[22] Abdollahipour A, Rahmannejad R. Investigating the effects of lateral stress to vertical stress ratios and caverns shape on the cavern stability and sidewall displacements. Arabian Journal of Geosciences 2012;2. https://doi.org/10.1007/s12517-012-0698-z.

[23] Abdollahipour A, Ghannadshirazi H. Stability analysis and determination of rock pillar between two adjacent caverns in different regions of Asmari formation in Iran. Int J Min Sci Technol 2014;24:593–6. https://doi.org/10.1016/j.ijmst.2014.07.005.

[24] RocScience Inc. Phase2: finite element analysis and support design for excavations. 2005.

[25] Sitharam T, Sridevi J, Shimizu N. Practical equivalent continuum characterization of jointed rock masses. International Journal of Rock Mechanics & Mining Sciences 2001.

[26] Jafari A, Hedayatjou J. 3D stability analysis and support designation of tunnels of Gotvand powerhouse dam. 7th Iranian tunnel Conference. (In Persian)., 2003.

[27] Yosefian A. The design and consideration of segmental lining case study: 3 and 4 of the Qumroud tunnel. (In Persian). ShahidBahonar University of Kerman, 2008.

[28] Johansson J. High Pressure Storage of Gas in Lined Rock Caverns, Cavern Wall Design Principles. Royal Institute of Technology, Stockholm, Sweden, 2003.

[29] You K. An assessment of safety factor for tunnels excavated in a weak rock layer. (In Korean). J of Korean Tunnelling Association 2000:47–57.

[30] You K. Estimation of rock load for the design of 2-arch tunnel lining. The World Tunnel Congress & 33rd ITA/AITES Annual General Assembly, Prague: 2007, p. 785–9.

[31] Hoek E, Carranza-Torres C, Diederichs MS, Corkum B. Integration of geotechnical and structural design in tunnelling. 56th Annual Geotechnical Engineering Conference, Minneapolis, Minnesota: 2008, p. 1–53.

[32] Timoshenko SP. Strength of Materials, Part II, Advance Theory and Problem. New York: Van Nostrand Reinhold; 1976.

Vol. 15, No. 45, Winter 2026, pages 23-34

Journal of Analytical and Numerical Methods in Mining Engineering

Journal home page: http://anm.yazd.ac.ir/

Research article

Optimum mine dump design in Wardha Valley coalfields using finite difference numerical methods

Radhakanta Koner[1]*

1- Dept. of Mining Engineering, Indian Institute of Technology (Indian School of Mines), Dhanbad, India

*Corresponding author: E-mail: *rkoner@iitism.ac.in*

(Received: *February 2025*, Accepted: *September 2025*)

DOI: 10.22034/ANM.2025.22754.1665

Keywords

Mine dump

Dump Height

Slope Angle

Stage dumping

Dynamic loading

Factor of Safety

Abstract

The Wardha Valley coalfields are experiencing an acute shortage of dumping space for ongoing open-pit projects. This creates barriers to expanding the life of the projects and to developing the coal in greater depth. The acquisition of new land to dispose of waste material is challenging in the present socio-economic conditions of the region. The project administration cannot afford to lose large amounts of coal at greater depths. So, it is necessary to optimise the geometry of the waste dump slope. A steep slope can lead to a potential failure, and a flat slope may not be an economically viable option, so a balance must be found between these two aspects. In this study, a finite-difference numerical tool was used to account for the multiple factors contributing to the stability of mine dumps. The analysis was considered as a static and dynamic analysis using the FLAC2D finite-difference numerical modelling tool. The study proposed a viable alternative to waste dump geometry to optimise the use of natural resources in the Wardha Valley coalfields. The work showed that double-stage dumping is more advantageous. This study also showed that mining companies could accommodate 18% more waste rock in the available space without compromising safety by following this analysis.

1. INTRODUCTION

Large-scale mechanization and big opencast mining projects emerged in India after the 1990s. The open-pit project is prevalent in different coal mining projects in the country, with the increasing demand for coal [1]. Mining depths are increasing day by day due to the exhaustion of shallow deposits. The lifetime of projects increases with deep open-pit mines; thereby, efficient planning and design of the bench slope, pit slope, access roads, etc., become essential for the life of projects. The need for stability analysis becomes very important due to steep bench slopes, overall pit slopes, and increased bench heights. The volume of overburden removed last year was around 1926.34 million cubic meters [1]. This volume will soon increase due to the anticipated growth of open-pit coal mining projects. Hence, dumping such a large volume of overburden in the proper place and stabilizing the dump slope is also a challenging technical and economic problem for coal mining enterprises. Shortly, 500-800 m deep coal deposits may be exploited by India's opencast coal mining method. So, a large-scale study of the mine dump stability should be carried out before implementing such projects.

Experience has shown that since open-pit projects began, the material has been dumped in stages, keeping some free space within limited reach. So, a common practice in Indian open-pit projects is to maintain benches in the mine dump. This facilitates efficient management of the mine

dump. The stage dumping allows the mining department to better handle the mine dump by adhering to several safety regulations. The limited space within the leased area and the management of the huge volume of waste rock have forced the mining authority to adopt the heightening of mine dumps beyond the permissible limits. In this particular situation, there are only a few alternatives for the miners. One is to run the mine with an increasing stripping ratio and at the same time, maintain the safety of the mine dump. This necessitates a revised parametric study to optimize the mine dump geometry with all prevailing external boundary conditions taken into account. A mining region in India with an acute shortage of dumping space and several other restrictions imposed from time to time by the regulatory authority was chosen for the study. Open-pit mining projects dominate this mining area, and guidance on dumping patterns is needed to run these mines.

This investigation thereby focuses on considering three alternative modes of dumping: single stage, double stage, and triple stage. In the stages, the bench height is limited to 30 m, but to cover the whole domain of viable alternatives, it has been increased to 90 m in some cases. The analysis takes into account the gravity load as the self-weight of the waste rock and the dynamic loading conditions to which these dumps are often subjected during major earthquakes. When designing a dump, there are many ways to assign values and combine various geometric and dimensional parameters while respecting safety and environmental constraints. The total tonnage capacity required can have as many geometrical representations as its limitations allow. In this situation, building a mathematical optimization model is the best option to interrelate certain vital variables. Given the broad scope of numerical applications available today, it has become essential for engineers to fully understand the varying strengths and limitations inherent in each of the different methodologies. When assessing slopes, geotechnical engineers use a factor of safety value to determine the stable/unstable conditions of slopes. The marginal equilibrium technique is the most commonly used conventional analysis method. However, with the help of recent significant advancements in computational and memory resources, geotechnical engineers, given the low-cost implications, have found the finite difference method (FDM) to be powerful and valuable, a viable alternative for all pre-field applications. Although there are certain limitations to the applicability of this method in capturing the actual field conditions, especially in cases of enormous discontinuity associated with the foundation of a large dump slope mass.

This work deals primarily with finding the optimum dump height and slope angle combination for safe overburden dumps. A parametric study has been conducted to analyze the effect of seismic vibration on dump stability.

1.1. Dump Design Considerations

A mine dump can be defined as a massive structure formed by placing large amounts of material in lifts of a restricted vertical expansion that lie one on top of the other and create a stable slope at the angle of repose. However, the formed dump needs a horizontal base, built by pushing dumping material from a specific elevation and leveling off the required footprint area.

Typically, this first phase in the construction of a dump construction takes the irregular shape of the terrain where it is placed. The height of the subsequent lift is constant, although it is limited to prevent shear stresses in the foundation and is a factor in control of consolidations and permeability variations [2]. The total height of the dump is also limited by the formation mechanism [3-9] and limitations of the carrying capacity [10, 11]. As with most the large open-pit operations, haulage is performed by heavy trucks. Access to the successive dump lifts is achieved by installing ramps of suitable width, superelevation, and gradient ramps to minimize the travel distance and reduce transportation costs. In dump designing, costs may be governed by any or all of the following factors:

1.1.1. Geometry

The dumps were usually designed to handle the total capacity throughout the life of mine. Over-sizing can cause the underutilization of valuable areas. Undersizing can increase the total haulage distances.

1.1.2. Operating costs

The costs result from fuel, energy, maintenance, and labour of the haul trucks.

1.1.3. Haulage distances

To minimize the total haulage distance while maintaining the required capacity by strategically placing ramps, exits, entrances, and dumping sequences.

1.1.4. Stability control

It will define the angle of repose and the nature of the underlying material. Maintaining the stability of the dump may require the relocation of waste rock or geomaterial, especially if water is present [12, 13].

1.1.5. Acquisition of the land

The dumping space requires a permit for dumping purposes, as specified by law.

1.1.6. Environmental factors

Costs of implementing and maintaining effective systems to reduce and eliminate losses. In the design considerations to maintain long-term stability, erosion control [14] should avoid rehandling costs [2] for reclamation and closure. Although every dump is unique [15], and some of its cost may be due to its factors, the above description includes all the general concerns that must be elaborated to develop the most economical dump design. Many of the parameters influencing mine dump slope design and optimizing the slope geometry are more economical when executing the project-specific guideline in the field. A finite-difference-based numerical toolbox is a good aid for modeling these options and possibilities and finding the best possible alternatives. In the dump design, it was observed that mine dump geometry optimization would meet many of the parameters that we have already discussed. Here is the importance of undertaking the present study.

2. MATERIALS AND METHODOLOGY

Slope stability analysis is an important area of geotechnical engineering for an open-pit project. Most textbooks on soil mechanics include several methods of slope stability analysis. A detailed review of equilibrium methods of slope stability analysis is presented by Duncan [16-18]. These methods include the ordinary practice of slices, Bishop's modified method, the force equilibrium methods, Janbu's generalized procedure of slices, Morgenstern-Price method, and Spencer's method. These methods, in general, require the soil mass to be divided into slices. The directions of the forces acting on each slice in the slope are assumed. This assumption plays a crucial role in distinguishing one limit equilibrium method from another. The limit equilibrium methods require a continuous surface for the soil mass to pass through. This surface is essential in calculating the minimum factor of safety (FOS) against sliding or shear failure. Before figuring slope stability using these methods, some assumptions, such as side forces and their directions, must be artificially set to build the equilibrium equations.

The finite difference approach in the analysis of slope stability problems does not assume the shape or location of the failure surface, slice side forces, and directions [18][19]. The method can be applied to complex slope configurations and soil deposits in two or three dimensions to model virtually all types of mechanisms. General soil material models that include Mohr-Coulomb and many others can be used. Equilibrium stresses, strains, and corresponding shear strengths in the soil mass can be computed very accurately. The critical failure mechanism developed can be extremely general and need not be simple circular or logarithmic spiral arcs. The method can be extended to account for seepage-induced failures, brittle soil behavior, random field soil properties, and engineering interventions such as geo-textiles, soil nailing, drains, and retaining walls. This method can inform about the deformations at working stress levels and monitor progressive failure, including overall shear failure [20].

2.1. Failure Mechanisms

The different failure modes that occur in mine waste dumps have been summarized by Caldwell and Moss [21], who reviewed these analysis methods. The typical mine dump of the Wardha Valley coalfields is shown in Figure 1. Surface or edge landslides may occur as the material moves down the slope. This failure mode is most likely to occur in crest-tipped embankments and is best evaluated by equations describing the stability of an infinite slope. A shallow landslide may occur if enough water enters the slope mass and flows parallel to the surface. Dumps placed on a flat surface of competent soil are the least likely to fail. However, if a thin layer of soft material covers the flat ground, base failure may occur. If the ground is inclined, base failure is more likely to occur. This mode of failure has been observed in both end-dump and embankments laid in layers.

Fig. 1. **Mine dumps of Wardha Valley coalfields.**

Block translation can occur where a dump is formed on inclined ground, and the soil cover is relatively thin and weak. An unusually high water table in a dam, earthquakes, or organic material decay beneath the dump may start such a failure. Circular arc failure through the dump material is most common where the dump material contains a significant percentage of fine-grain soil. Similarly, a circular arc failure surface can develop through a deep foundation soil deposit of fine-grained soil. In the Wardha Valley coalfields, it has been observed that the circular mode of failure is

prevalent; thereby, the primary focus in this study will be on this direction.

2.2. Deformations As An Indication Of Failure

Deformations occur in a slope due to stresses and shear displacements in the mass of material forming the dump. Some of these deformations, such as consolidation, are not indicative of failure, while others, such as shear displacement along the failure surface, are. It is necessary to distinguish deformations that indicate failure from those that do not to predict failure. This requires an understanding of the failure mode and the deformations that accompany it. Analytical techniques currently available to analyze dump deformations are cumbersome and not sufficiently accurate to enable pre-construction estimates of consolidation and failure deformations. Instead, failure criteria are usually based on experience gained as the dump is constructed. The rate of deformation and change of the pace of deformation are generally good indicators of the behavior of a slope. They were used to establish criteria indicative of failure. We used the observed deformation rate, rate of movement, and acceleration pattern parameters to assess the failure in a mine dump [22].

2.3. Mine Site

In this investigation, an extensive geotechnical characterization of the dump geomaterial was initiated to estimate various properties. The locations of nine of the eleven selected mines and the land cover map for the present study are presented in Figure 2. It can be observed that they all belong to the Kamtee series of coal formations available in this part of the country. They are characterized by a top layer of black cotton soil of varying thicknesses of 4 to 8 m.

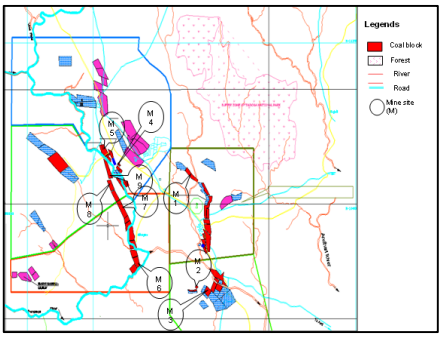

Fig. 2. Location of Mine Sites at Wardha Valley Coalfields.

2.4. Waste Rock Sampling Scheme

The variations in the soil and rock characteristics, and the varying complexity of dump conditions existing in the mines of the Wardha Valley coalfields considered in the present study, necessitated sampling methods of utmost importance. The dumps of these mine sites are of different categories, and a uniform sampling pattern of eight samples per dump was used to generalize the approach of sampling from each of the stages (benches) found in these dumps. Five samples were collected, following the standards, from the bottom and top benches, one from the middle bench and two from the top of the dump as shown in Figure 3, which is just representative and does not match the scale and shape of the existing dumps. Although a more rigorous sampling design might have proved better, we followed this sampling pattern due to the time and other resources of this study [23-25]. Thus, 252 samples were collected instead of 264 (i.e., eight samples per dump x 3 categories of dump per mine x 11 mine sites) because of the absence of a particular type of dump in some of the selected mines.

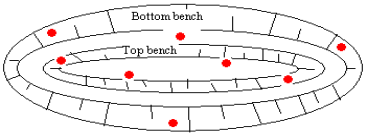

Fig. 3. Schematic Sample Collection Program from a Particular Dump (eight samples per dump).

2.5. Geotechnical Laboratory Interpretation

The materials constituting the mine dumps were collected from the fields, and they were mainly mixtures of broken rocks and loose soil. The proportion of loose soil was greater for the samples collected from the upper part of the dump than those collected from the lower part. Waste rock properties have mainly been attributed to the age of mine dumps, and mine dumps are divided into three categories.

a) Running dumps: Where active waste rock dumping is being carried out, further dumping will stop after reaching a certain desired height over a specific planned area.

b) Old dumps: Dumping here has been stopped for several years, and the mines have no plan to dump in the near future.

c) Vegetated dumps: Green reclamation has already been adopted/ achieved here, and there are no further plans for dumping.

Hence, this categorization will help the study team understand the diverse geotechnical nature of waste rock due to its age, changes in material properties due to compaction, and biological changes in the geo-materials that make up these dumps, etc., since a detailed investigation of material characteristics and site conditions forms the first part of any geotechnical study. We followed the detailed methods outlined in [26, 27].

Accurate determination of the representative shear strength of dump materials is essential for a

meaningful slope stability analysis. However, the value of shear strength determined by laboratory testing depends on many factors, particularly the type of soil, the quality of the test samples, the size of the test samples, and the test methods. In a direct shear test, the plane of shear failure is predetermined. The test is usually carried out in a box split into two halves; hence, it is a shear box test. The equation can characterize the shear strength of cohesive soils.

$$\tau = \sigma tan\varphi + c \quad (1)$$

where σ is the normal stress, c is the cohesion, and φ is the internal friction angle. The results are summarised in Table 1.

Table 1. Average Cohesion and Internal friction angle of dump geomaterial of different mines

Name of the mines	Cohesion (kPa)	Internal friction angle (°)
Mine 1	0.00	38.56
Mine 2	0.00	48.65
Mine 3	13.97	27.95
Mine 4	26.87	32.58
Mine 5	26.89	22.25
Mine 6	0.00	33.64
Mine 7	0.00	31.40
Mine 8	0.00	36.74
Mine 9	0.00	33.40
Mine 10	49.63	24.13
Mine 11	100.03	19.74

2.6. The Geometry Of The Mine Dump

Slope stability analyses were performed along the cross-section of the dump slope. The cross-section includes stages of dumping (single, double, and triple stage dumps with heights of 90m, 45m, and 30m high benches respectively), slope angle from 20 to 45 deg., and berm width from 12 to 20 m between the stages of dumping. In this study, the homogeneous basement was considered as the natural rock prevailing at the dumpsite for study, excluding major geological features. Several combinations of the parameters mentioned above were studied in a dimensional optimization problem, and a total of 1936 model was analyzed.

2.7. Seismic Coefficients

The dynamic factors as the cause of instability of the external mine dump slopes were studied in detail, and a complete modeling analysis was performed. Seismic coefficient values were used in the numerical modeling.

2.8. Boundary Conditions

The length of the outer boundaries of the numerical models was varied to select the far-field boundary conditions. It was observed that the outer boundary of the mine overburden dumps in the numerical model should be extended to 50 m on both sides of the toe to achieve the far-field conditions. And, in the vertical direction, it was found that is should be around 30 m from the base of the dumps to reach the far-field condition. In the elastic-ideal-plastic numerical analysis of the external mine overburden dumps, conducted in the investigation, these conditions were taken into account for modeling. It was necessary to model the entire mine dump, rather than any particular part of the dump, because of the lack of symmetry in the site dump geometry in order to obtain accurate stresses and displacements. The boundary condition that appeared to work best was roller boundaries on both sides except for the bottom surface, i.e., in dump stability analysis, the side boundary elements were constrained with velocity in the x-direction equal to zero.

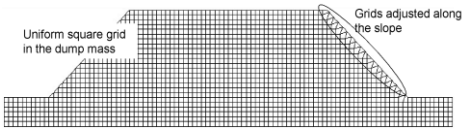

Fig. 3. A Single Stage Dump Section with Equal Grid Size.

And, the lowest boundary elements were constrained to zero velocity in both x- and y-. A uniform, quadratic grid with equal zone size was used, as shown in Figure 4, to minimize the effects of the grid in continuum modeling. The grids were adjusted along the slope surface to reduce the eccentricity of these elements, as depicted in Figure 4 — a similar grid pattern adopted in double- and triple-stage mine dump slopes.

2.9. Fully Dynamic Numerical Model

A fully dynamic analysis is recommended for higher acceleration levels. Dynamic numerical analysis using explicit time integration schemes poses a computational stability problem [28-31]. The time step between increments is kept below a critical value to ensure computational stability. Incremental displacements in the finite-difference grid are calculated from the velocity field of the previous step. However, stability and accuracy are two different issues. The fact that stability is maintained does not automatically guarantee that the analysis results will be accurate. With explicit time integration, stresses and displacements are calculated by extrapolating the velocity field of the previous step. This means that displacements and stresses change linearly between steps (i.e., a constant velocity between steps is assumed). It is argued that keeping the time steps small enough (like those small-time steps on the order of 10^{-6} seconds required for stability) will provide an

accurate solution. The continuum model solves the equation of motion for mass-spring-dashpot systems in the time domain with incremental time steps. The calculated incremental displacements are related to the incremental stresses associated with chosen constitutive relationships the program uses explicit time step integration between consecutive steps. A critical time step is chosen to maintain computational stability [32]. The critical time step is selected $1.1x10^{-6}$ in this study. For simplicity, dry conditions were assumed, and a simple constitutive model was used; hence, the elements were modeled as elastic perfectly plastic Mohr-Coulomb materials. It should be noted that Rayleigh damping was used. Vertical displacement was fixed at the boundary since it was assumed that a very stiff in-situ layer exists at a depth of 30 m. The displacements are bound together at the lateral boundaries in both directions [33]. Assuming that waves radiating from the boundaries can be neglected, the coupled boundary condition with coupled degrees of freedom accurately models the free-field response at the lateral boundaries [34].

2.10. Input Ground Motion

The stability of the created and existing dumps for different mine sites was analyzed with different ground motion conditions. The El Centro time history recorded at 117 (USGS) station during the Imperial Valley earthquake was used in the analysis (Fig. 5). The study considered three acceleration time histories of the 1941 Imperial Valley earthquake. We used the PEER strong-motion database. The acceleration time histories were applied incrementally to all nodes along the lower boundary of the finite-difference model. It should be noted that the low-frequency components of earthquake motion usually dominate the displacement response [35]. Thus, displacement histories at different monitoring points were computed to assess the effect of numerical dissipation on the low-frequency response. After observing the response frequency, it can be assumed whether inaccurate high frequencies have been introduced into the solution.

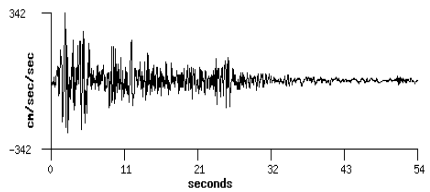

Fig. 5. Ground Acceleration Time histories of the records in the analyses – El Centro Earthquake CA - Array Sta 9; Imperial Valley Irrigation District - 302 Commercial, United States Geological Survey.

3. RESULTS AND DISCUSSION

In the analysis, a constant height of 90 m was used. The bench height and slope angle were varied, and the combinations of a large number of the models were analyzed.

A total of 1,936 models have been analyzed in three different dumping patterns: single stage, double stage, and triple stage dumping, shown in Table 2. This study was conducted to fulfill the main purpose of this research work. The summarised results (Table 2) showed a corresponding increase in volume accommodation capacity for a total base dump slope angle of 28.5° at a constant total height of 90 m and berm width of 12 m in all the cases. The changes in cross-sectional area at a constant total height and the same base area were calculated for these three different dumps to assess the volume of accommodation. For the lower bench height, the inclination may be increased, which prevails in the analysis. The double-stage dumping is advantageous because of the total waste rock accommodation capacity on the same base area, after comparing the results shown in Table 2. On average, it is about 1.5 times greater compared to the triple-stage dumping as a whole.

3.1. Static Condition

When analyzing the static stability, the safety factor was calculated and assumed 1.25 as a long-term factor, and the results correspond to those shown in Table 2.

The increase in capacity of the design dumps is calculated relative to the 28.5-degree dump slope limit set by the competent authority in Indian mining conditions, projecting an increase in the scope of dumping at the specific mine locations saving precious land.

3.1.1. Effect of Dump Parameters on Stability

The parametric analysis investigated the effects of dump height, soil strength, and the dump slope angle on permanent displacements of the base case slope. The values of the base case parameters were increased and decreased to create a range of observed behavior.

Table 2. Results of static analysis with FLAC tool

Name of the mines	Configuration Analyzed	Dump Slope Angle (in degrees)	Percentage of increase of volume
Mine 1	Single stage	30	5.95
	Double stage	32.63-37.04	7.15-13.18
	Triple stage	30.54-34.43	3.5-9.15
Mine 2	Single stage	35	22.45
	Double stage	41.42	18.07

	Triple stage	38.29	13.73
Mine 3	Single stage	25	0
	Double stage	31.55-35.69	5.27-11.10
	Triple stage	26.57-30.54	0-3.5
Mine 4	Single stage	35	22.45
	Double stage	37.04-41.42	13.18-18.07
	Triple stage	34.43-38.29	9.15-13.73
Mine 5	Single stage	20-25	0
	Double stage	23.70-26.85	0
	Triple stage	25.37-26.57	0
Mine 6	Single stage	28.5	0
	Double stage	28.19-32.63	0-7.15
	Triple stage	26.57-30.54	0-3.5
Mine 7	Single stage	25	0
	Double stage	26.85-28.19	0
	Triple stage	26.57	0
Mine 8	Single stage	30	5.95
	Double stage	32.63	7.15
	Triple stage	30.54-34.43	3.5-9.15
Mine 9	Single stage	28.5	0
	Double stage	28.19-32.63	0-7.15
	Triple stage	26.57-30.54	0-3.5
Mine 10	Single stage	30	5.95
	Double stage	32.63	7.15
	Triple stage	30.54-34.43	3.5-9.15
Mine 11	Single stage	30	5.95
	Double stage	32.63-37.04	7.15-13.18
	Triple stage	34.43-38.29	9.15-13.73

3.1.2. Effect of Bench Height on Stability of Dump

The height of the mine dump affects the magnitude of permanent displacements, as shown in Table 3 for a standardized single stage dump with a slope angle equal to 28.5°. The displacement was found to increase as the slope height increased. The average maximum displacement magnitudes obtained from the different models are shown in Table 3. It is observed that as the slope height increased, the maximum displacements also increased. The locations of these displacements were intentionally ignored in this part of the analysis because we are performing only a parametric analysis, but we are not considering the area of instability. Increased displacements indicate a high possibility of failure of the slopes unless proper preventive measures are taken. It was observed that a change in the dump height from 50 m to 90 m with an overall deviation of ±20% caused a change in maximum displacement from 11.89 cm to 14.65 cm with an average deviation of ±11.5% (Table 3). The relationship between these two parameters remains linear for the ranges analyzed in this study.

Table 3. Results of static analysis with FLAC tool

Dump Height (m)	Average Maximum Displacement (cm)
50	11.89
60	12.32
70	13.43
80	14.27
90	14.65

3.1.3. Effect of Slope Angle on Dump Stability

The dump slope angle affects the magnitude of permanent displacements shown in Table 4 for a standardized single-stage dump of 90 m. Displacement decreased when the slope was flatter. The average values of maximum displacements obtained from the models analyzed are shown in Table 4. It was observed that the maximum displacement increases with the dump angle. The locations of these displacements were intentionally ignored in this part of the analysis. It was observed that a change in the dump angle from 20° to 40° with an overall deviation of ±10% caused the average maximum displacement to change from 14.08 cm to 26.92 cm with an average deviation of ±10% (Table 4), except for the last case where a deviation of 77% was observed. The relationship between these two indices remains non-linear for the ranges analyzed in this study. It was observed that for dump angles between 28.5° to 30° and 35° to 40°, the rate of change of the average maximum displacement with the slope angle increased rapidly.

Table 4. Average Maximum Displacement with the Corresponding Dump Angle

Dump Angle (°)	Average Maximum Displacement (cm)
20.0	14.08
25.0	14.53
28.5	14.65
30.0	15.67
35.0	16.33
40.0	26.92

3.1.4. Effect of Internal Friction Angle on Dump Stability

The values of the internal friction angles are assumed to reflect the strength of the soil. It was found that an increase in the soil strength results in an increase in resistance to permanent displacements. This part of the investigation was carried out for numerical dump models with 28.5° as the overall slope angle and a height of 90 m for a single-stage dumping mode. A considerable

effect of the friction angle on the permanent displacements was observed, as shown in Table 5. The average maximum displacements in magnitudes obtained from the analyzed numerical models are shown in Table 5. It was observed that the maximum displacements decreased with an increase in the friction angle of the dump materials. The locations of these displacements were intentionally ignored in this part of the analysis. It was observed that a change in the friction angle of the dump materials from 31.40° to 48.65° with an overall deviation of ±26% caused a change in the maximum displacement from 14.65 cm to 164.90 cm with an average deviation of ±85.14% (Table 5). The observed relationship between the friction angle and maximum average displacement remains non-linear for the ranges analyzed in this part of the study.

Table 5. Average Maximum Displacement with the Corresponding Friction Angle

Internal Friction Angle (°)	Average Maximum Displacement (cm)
31.40	164.90
32.58	98.64
33.40	73.88
33.64	66.88
36.74	32.64
38.56	27.46
48.65	14.65

3.2. Pseudo-Static Analysis

The pseudo-static analysis is an extended limit equilibrium method and uses calculated dynamic earth pressure to assess the stability of slopes [16]. The magnitude of the dynamic force and the lateral inertia force per slope mass are evaluated using a seismic coefficient. Various methods and empirical recommendations make it possible to estimate the magnitude of dynamic earth pressures. Once the magnitudes of static and dynamic forces are estimated, different failure mechanisms, both external and internal, can be tested for stability. These mechanisms include sliding along the base and overturning.

The mine locations are not subject to strong seismic zones; instead, it is a low-seismicity area. The present study takes a seismic coefficient of 0.1 in the pseudo-static mode of study, and the results are shown in Table 6. It was found that the factor of safety decreased by 2-3 percent.

Table 6. Dynamic stability analysis of dumps

Name of the Mines	Configuration Analyzed	Slope Angle	Factor of safety
Mine 1	Single stage	30	1.16
	Double stage	32.63-37.04	1.12
	Triple stage	30.54-34.43	1.09
Mine 2	Single stage	35	1.11
	Double stage	41.42	1.13
	Triple stage	38.29	1.45
Mine 3	Single stage	25	1.10
	Double stage	31.55-35.69	1.14
	Triple stage	26.57-30.54	1.06
Mine 4	Single stage	35	1.09
	Double stage	37.04-41.42	1.22
	Triple stage	34.43-38.29	1.14
Mine 5	Single stage	20-25	1.11
	Double stage	23.70-26.85	1.05
	Triple stage	25.37-26.57	1.14
Mine 6	Single stage	28.5	1.02
	Double stage	28.19-32.63	1.10
	Triple stage	26.57-30.54	1.08
Mine 7	Single stage	25	1.11
	Double stage	26.85-28.19	1.02
	Triple stage	26.57	1.04
Mine 8	Single stage	30	1.13
	Double stage	32.63	1.09
	Triple stage	30.54-34.43	1.04
Mine 9	Single stage	28.5	1.06
	Double stage	28.19-32.63	1.12
	Triple stage	26.57-30.54	1.07
Mine 10	Single stage	30	1.08
	Double stage	32.63	1.12
	Triple stage	30.54-34.43	1.11
Mine 11	Single stage	30	1.14
	Double stage	32.63-37.04	1.10
	Triple stage	34.43-38.29	1.10

3.2.1. Effect of Horizontal Seismic Coefficient on Dump Stability

The impact of the varying horizontal seismic coefficient (HSC) on the dump stability is examined in this section. Figure 6 below shows a columnar representation of the varying safety factor with HSC for the running dump geometry of ten mine sites and material conditions. HSC values of 0.01, 0.03, 0.05, 0.08, and 0.1 were analyzed in this part of the study.

It is observed that the safety factor decreases with an increase in the HSC. The safety factor remains maximum for the static case compared to the safety factors obtained in the dynamic model.

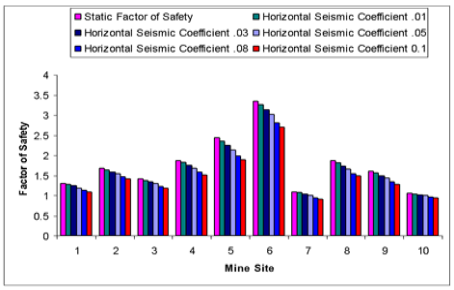

Fig. 4. Increasing Horizontal Seismic Coefficient Shows Decreasing Safety Factor.

3.3. Seismic Stability Analysis

It is necessary to investigate earthquakes, how the dump mass behaves during vibration, the magnitude of stress and deformation during and after vibration. The numerical analysis is performed for a 2D cross-section of the total dump mass. Analyses of the effects of ground failure/settlement are outside of the scope of this numerical study.

3.3.1. Effect of Input Accelerations on Displacements

The effect of input motion on the permanent average displacements was investigated in this part of the study. Four recorded earthquakes with different durations, amplitudes, and frequency contents were selected for analysis. For each of these recordings, the peak horizontal accelerations causing slope movement were scaled to match the El Centro base excitation (PHA= 0.2 g). Predicted displacements for each of these modified earthquake records were noted. The range of final displacements was from 0.7 cm to 8.7 cm, which was predicted for a numerical dump model of a single stage of 90 m high, with a slope angle of 28.5° having the same material conditions as mine site 2. This observation reflects the high level of record-to-record variability inherent in earthquake motion. This suggests that the design of dump slopes should not be based only on the analysis of a single ground motion record alone.

3.3.2. Effect on Stage Dumping

The present investigation compares combinations of different mine dump geometries and stage dumping to find the optimized one to make the best use of the available natural resources to the fullest extent. Thereby, we investigated all three types of dumps with dynamic load application and simulated the responses. Numerical models developed and analyzed for the different dump conditions were diagnosed under dynamic loading conditions. The selected models analyzed here represent stable configurations obtained from static analysis results and are shown in Table 2. All of these models analyzed for the material properties for mine site number two are shown below. Similar analyses have been carried out for all available configurations of material properties and the stable dump geometries. The results for the single, double, and triple stage configurations are presented below in sequence.

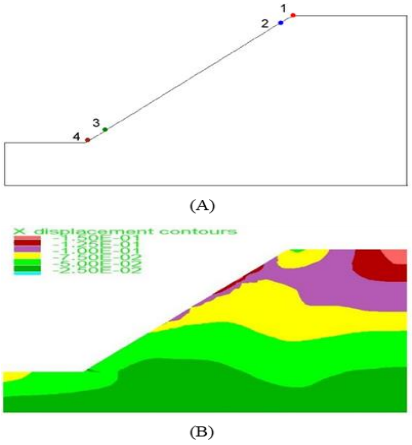

Fig. 7. Single Stage Dump Slope (90 m height and 35° slope angle with Four Monitoring Points (A); Horizontal Displacement Contours at Single Stage Dump Slope after 10 s of Dynamic Load (B).

Figure 7 shows the left side monitoring points in the studied dumps for the single stage with a 35° slope angle. The study used a double stage with 12 m berm distance and 40° stage angles; and a triple stage with 25 m berm distance and 30° stage angles for conducting a similar study. The numerical models used twice as many monitoring points with an equivalent number of points on the right side of each dump for analysis. The displacement time histories for monitoring points 1 and 4 have the same trend as points 2 and 3 for single-stage dumping with a maximum value of 18.74 cm and a minimum of 10.92 cm, as shown in Table 7. A similar character was observed for the the curves in time history of velocity and acceleration of these points. It was observed that the displacement and velocity remained neard zero until 0.5 s. In contrast, the acceleration remained insignificant up to 1.5 s after applying the excitation. The contour of the horizontal displacement vectors for the three stages indicated that the double-stage dumps had a smooth change in displacements. It was noted that the range of overall horizontal displacements was the smallest for the single-stage dumping, then the double-stage dumps, and then the triple stage dumps for mine site 2. Table 7 shows the range of magnitudes obtained by analyzing the effect of input acceleration for single, double, and triple stage dumps. The left monitoring points represent the horizontal displacement, horizontal velocity, and horizontal acceleration time histories.

Table 7. Displacement, Velocity and Acceleration at the Monitoring Points in the Dump Slope during Dynamic Loading

Sl. No	Type of Slope	Range of Displacement (cm) (Min to Max)	Range of Velocity (cm/s) (Min to Max)	Range of Acceleration (cm/s2) (Min to Max)
1	Single Stage Mine Dump Slope	-10.92 to 18.74	-40.08 to 40.94	-396.27 to 538.53
2	Double Stage Mine Dump Slope	-117.22 to 12.39	-78.24 to 38.61	-376.56 to 518.80
3	Triple Stage Mine Dump Slope	-285.81 to 7.43	-182.60 to 94.23	-1718.26 to 1468.48

4. OBSERVATIONS

From the plots and their time histories of horizontal velocity and acceleration over 10 s, as shown in Table 7 for the single, double, and triple stages of dumping, it is clear that changes in acceleration occurred more frequently in the triple-stage dumps, then in the double stage, and then single-stage dumping patterns. The range of change in the acceleration values was maximum for the triple-stage dumps, whereas a similar change was observed for the single- and double-stage dumps. For single-stage dumping, the maximum and minimum displacement, velocity, and acceleration values were (18.74, -10.92) cm, (40.94, -40.08) cm/s, and (538.53, -396.27) cm/s2, respectively, for the monitoring points mentioned above. A similar analysis for the double-stage dumping gave the maximum and minimum values of (12.39, -117.22) cm for displacement, (38.61, -78.24) cm/s for velocity, and (518.80, -376.56) cm/s2 for acceleration at the monitored points. Whereas for the triple-stage dumping, the maximum and minimum values of (7.43, -285.81) cm for displacement, (94.23, -182.60) cm/s for velocity, and (1468.48, -1718.26) cm/s2 for acceleration were obtained at the monitored points. The ranges of displacements, velocities, and accelerations obtained for the single-, double-, and triple-stage dumps were (28, 129, 293) cm for displacements, (86, 116, 276) cm/s for velocities, and (934, 904, 3176) cm/s2 for accelerations.

Although it is difficult to compare the changes in the displacements, velocities, and accelerations obtained with the static and dynamic modes of analysis, it was observed that the overall range of displacement changes at similar monitoring points showed higher displacement values for the dynamic analysis model compared to the corresponding static mode of analysis. The same was observed when comparing double and triple stages of dumping patterns for all three parameters, namely displacement, velocity, and acceleration values. The overall dump slope angles were unequal in the above models (35.0° for single-stage, 41.4° for double-stage, and 24.0° for triple-stage dumping), although the height was constant (90 m). It may be noted that the observed x-displacements differ in the three cases. It should not be concluded that single-stage dumping is safer (as seen in the x-displacement plots) than the double-stage dumping. It may be noted that even at a dump slope angle of 40°, the single-stage dump became unstable in the static analysis under the present conditions.

5. DISCUSSION

Mines 1, 2, 4, and 11 have higher slope angles than the other mine dumps due to their higher frictional characteristics of the mine dumps material. A maximum 41.42 degree dumps slope is possible with the present characteristics of the overburden material with a volume gain of 18.07%. These mines will benefit from a longer project life and compared to production expansion. The highest gain of volume accommodation was obtained for mine number two, at 22.45% for single-stage dumping. It was also observed that a mine dump with a 41.42º slope angle would remain safe under prevailing seismic conditions. In a worst-case scenario analysis, it was found that the obtained slope angle would remain stable over the longer term of the project. The study showed that optimization analysis using a parametric comparison of different field parameters and site conditions plays an influential role in good project planning and optimization of land resources. In the deformation study, the peak permanent deformation ranges from 11.89 cm to 14.65 cm for the dump heights of 50 m to 90 m. Similarly, it ranges from 14.08 cm to 26.92 cm for a dump slope angle of 20º to 40º. And for the available material characteristics of the angle of internal friction 31.4º to 48.65º, the deformation decreases from 164.9 cm to 14.65 cm. So, it was observed that deformation under pseudo-static loading is more sensitive to the material friction properties.

6. CONCLUSIONS

The following conclusions can be drawn from the results of this investigation:

1. The dumping pattern has an impact on the stability characteristics of the external overburden dumps. Double-stage dumping shows a higher factor of safety than single- and triple-stage dumping. It is possible to make the overall

dump slope angle steeper without sacrificing the safety factor in the case of double-stage dumping.

2. The influence of average seismic intensity showed very little effect on the stability of the dumps since the stable and safe dump slope angles differ by at most 1%-3% in relation to the angles obtained from the static analyses.

3. The impact of dynamic loading due to blast vibration and earthquakes causes more deformation in the toe side of the dump slope than in the crest of the dump. Vibration amplitudes in this area are more accentuated than in the crest area. The duration of these loads has an adverse effect on the dump slope stability (length of duration varies from 2 to 10 s). Every second of increasing time increment leads to a7.6% increase in dump slope displacement.

4. Dynamic analysis shows that the height and slope angle negatively affect the dump deformation in the analyzed range of 50–90 m and 20°-40°, respectively, with the observed deformation range of 11.9-14.7 cm and 14.1-26.9 cm. The material friction angle analyzed in the 31.4°-48.7° range showed significant potential for influencing the deformational dump characteristics observed in the 164.9-14.7 cm range. Ground motion input with a scaled peak amplitude of 0.2g showed that El-Centro seismic input affected the deformational dump characteristics more than Loma-Prieta, Friuli, and Kobe, with a change of 0.7-8.7 cm.

5. The failure surface in the dump slopes obtained from static and dynamic analyses was found to be circular. Parameters such as shear strain, displacement, and yield point plots were efficiently used as indicators to predict circular failure. In the absence of direct failure plane analysis as a result of continuum-based numerical modeling, they had a good agreement with each other.

Data Availability Statement

All data and computer codes used in this work will be provided by email to the corresponding author upon reasonable request.

Declaration of Competing Interest

The author states that he has no known competing financial interests or personal relationships that would affect the work presented in this paper.

Acknowledgments

The author is thankful to IIT(ISM) Dhanbad for conducting this research. This work was supported by the IIT(ISM) Dhanbad [grant number FRS (108)/2016-17/ME, 2020].

REFERENCES

[1] Provisional Coal Statistics, Ministry of Coal, Government of India, http://coal.gov.in/sites/default/files/2021-06/Provisional-Coal-Statistics-2020-21_0.pdf Accessed last June 2021

[2] Jorge Puell Ortiz, Methodology for a dump design optimization in large scale open-pit mines, Cogent Engineering, 4:1, 1387955, (2017) http://dx.doi.org/10.1080/23311916.2017.13879.

[3] J.R. Metcalf, Angle of repose and internal friction, Int. J. Rock Mech. Min. Sci. 3 (1966) 155–161. https://doi.org/10.1016/0148-9062(66)90005-2.

[4] S. Sujatono, The determination of mine waste dump material properties through back analysis, J. King Saud Univ. - Eng. Sci. (2021). https://doi.org/10.1016/j.jksues.2021.02.008.

[5] K.M. Khan, G. Bushell, Comment on "rolling friction in the dynamic simulation of sandpile formation," Phys. A Stat. Mech. Its Appl. 352 (2005) 522–524. https://doi.org/10.1016/j.physa.2005.01.019.

[6] S. Supandi, Geotechnical profiling of a surface mine waste dump using 2D Wenner–Schlumberger configuration, Open Geosciences 13.1, (2021) 335–344. DOI: 10.1515/geo-2020-0234.

[7] P. Zou, X. Zhao, Z. Meng, A. Li, Z. Liu, W. Hu, Sample Rocks Tests, and Slope Stability Analysis of a Mine Waste Dump, Advances in Civil Engineering 2018, (2018). https://doi.org/10.1155/2018/6835709.

[8] S. Liu, H. Wang, W. Xu, Z. Cheng, Z. Xiang, W. Xie, Numerical Investigation of the Influence of Rock Characteristics on the Soil-Rock Mixture (SRM) Slopes Stability, 24 (2020) 3247–3256. https://doi.org/10.1007/s12205-020-0034-1.

[9] Zhang, D., et al. (2014) Study on Formation Mechanism of Dumping Piles on Dumping Area Stability, Open Journal of Geology, 4, 161-175. http://dx.doi.org/10.4236/ojg.2014.44012.

[10] Peng, C., Ji, D., Zhao, L., Ren, F.H., 2013. Study on Limit Height and its Stability of Open-Pit Dump Based on Basement Bearing Mechanism. AMM 405–408,177–181. https://doi.org/10.4028/www.scientific.net/amm.405-408.177

[11] AK Bharati, A. Ray, R. Rai, A Stability Classification System for the Dragline Dump Slope, Mining, Metallurgy & Exploration 38.2,(2021) 1095–1109. https://doi.org/10.1007/s42461-021-00409-8.

[12] Russell, M. (2008) So you want to have the best possible waste rock dump, in Proceedings First International Seminar on the Management of Rock Dumps, Stockpiles and Heap Leach Pads (Rock Dumps 2008), A.B. Fourie (ed), 5–6 March 2008, Perth, Australia, Australian Centre for Geomechanics, Perth, pp. 117–128.

[13] M. Water, A.K. Singh, Quality Assessment of Mine Water in the Raniganj Coalfield Area, India Quality Assessment of Mine Water in the Raniganj

Coalfield Area, India, (2010). https://doi.org/10.1007/s10230-010-0108-2.

[14] Pantelis, G., Ritchie, A.I.M. and Stepanyants, Y.A., 2002, A conceptual model for the description of oxidation and transport processes in sulphidic waste dumps. Applied Mathematical Modeling, v. 26, p. 751-770.

[15] Petra Zástěrová, Marian Marschalko, Dominik Niemiec, Jan Durďák, Roman Bulko, Jozef Vlček, Analysis of Possibilities of Reclamation Waste Dumps after Coal Mining, Procedia Earth and Planetary Science, Volume 15, 2015, Pages 656-662, https://doi.org/10.1016/j.proeps.2015.08.077.

[16] C. Zienkiewicz, C. Humpheson, R.W. Lewis, Associated and non-associated visco-plasticity and plasticity in soil mechanics, Geotechnique 25.4, (1975) 671–689. https://doi.org/10.1680/geot.1975.25.4.671.

[17] M. Ghadrdan, A.P. Dyson, T. Shaghaghi, A. Tolooiyan, Slope stability analysis using deterministic and probabilistic approaches for poorly defined stratigraphies, Geomech. Geophys. Geo-Energy Geo-Resources. 3 (2021). https://doi.org/10.1007/s40948-020-00189-3.

[18] Duncan, J. M. (1996). State of the Art: Limit Equilibrium and Finite-Element Analysis of Slopes. Journal of Geotechnical Engineering, 122(7), 577–596. https://doi.org/10.1061/(asce)0733-9410(1996)122:7(577).

[19] Kaerbek Rafkatovich Argimbaev, 2016. Simulation of Rock Mass Stress-Strain Behavior Using the Method of Equivalent Materials During Ore Deposit Open-Pit Mining. Research Journal of Applied Sciences, 11: 894-899. doi: 10.36478/rjasci.2016.894.899.

[20] Radhakanta Koner, Debashish Chakravarty, Numerical analysis of rainfall effects in external overburden dump, International Journal of Mining Science and Technology, Volume 26, Issue 5, 2016, Pages 825-831, https://doi.org/10.1016/j.ijmst.2016.05.048.

[21] S. Liu, Z. Su, M. Li, L. Shao, Slope stability analysis using elastic finite element stress fields, Eng. Geol. 273 (2020) 105673. https://doi.org/10.1016/j.enggeo.2020.105673.

[22] Griffiths. D. V. and Lane. P. A.; (1999), Slope Stability analysis by finite elements, Geotechnique, 49(3), 387-403, https://doi.org/10.1680/geot.1999.49.3.387.

[23] R. Brummer, P. Andrieux, C. Detournay, R. Hart, FLAC and Numerical Modeling in Geomechanics 2003, FLAC Numer. Model. Geomech. 2003. (2003). https://doi.org/10.1201/9781439833490.

[24] Hekmat, M. Osanloo & Akbarpour M. Shirazi, New approach for selection of waste dumpsites in open-pit mines, Mining Technology, 2008, 117:1, 24-31.

[25] MC He, J.L.Ã. Feng, X.M. Sun, Stability evaluation and optimal excavated design of rock slope at Antaibao open-pit coal mine, China, 45 (2008) 289–302. https://doi.org/10.1016/j.ijrmms.2007.05.007.

[26] Okagbue, C.O., 1984, The geotechnical characteristics and stability of a spoil heap at Southwestern Pennsylvania coal mine, USA: Engineering Geology, v. 20, p. 325– 341.

[27] Koner, R., Chakravarty, D. (2016) Characterisation of overburden dump materials: a case study from the Wardha valley coalfield. Bull Eng Geol Environ 75, 1311–1323. https://doi.org/10.1007/s10064-015-0830-x.

[28] Rezaiee-Pajand, M., and Karimi-Rad, M. (2016) A New Explicit Time Integration Scheme for Nonlinear Dynamic Analysis, International Journal of Structural Stability and Dynamics, Vol. 16, No. 09, 1550054 (26 pages), https://doi.org/10.1142/S0219455415500546.

[29] Liang Lu, Zongjian Wang, Xiaoyuan Huang, Bin Zheng, Katsuhiko Arai, (2014) "Dynamic and Static Combination Analysis Method of Slope Stability Analysis during Earthquake", Mathematical Problems in Engineering, vol. 2014, Article ID 573962, 13 pages. https://doi.org/10.1155/2014/573962.

[30] Lisjak, A., and Grasselli, G. (2011) Combined finite-discrete element analysis of rock slope stability under dynamic loading, Pan-Am CGS Geotechnical Conference, October, 2-6, 2011, Toronto, Ontario, Canada, http://geoserver.ing.puc.cl/info/conferences/PanAm2011/panam2011/pdfs/GEO11Paper473.pdf

[31] Wei, W., Zhao, Q., Jiang, Q., Grasselli, G. (2018) Three new boundary conditions for the seismic response analysis of geomechanics problems using the numerical manifold method, International Journal of Rock Mechanics and Mining Sciences, Volume 105, Pages 110-122. https://doi.org/10.1016/j.ijrmms.2018.03.009.

[32] Noferesti, H., Hazegh, A. (2018). 'Comparison of pseudo-static, Newmark and dynamic response analysis of the final pit wall of Sungun copper mine', International Journal of Mining and Geo-Engineering, 52(2), pp. 141-147. https://doi.org/10.22059/ijmge.2018.229315.594661.

[33] A. Johari, A.R. Khodaparast, Analytical stochastic analysis of seismic stability of infinite slope, Soil Dyn. Earthq. Eng. 79 (2015) 17–21. https://doi.org/10.1016/j.soildyn.2015.08.012.

[34] CR Mcgann, P. Arduino, P. Mackenzie-Helnwein, Computers, and Geotechnics A stabilized single-point finite element formulation for three-dimensional dynamic analysis of saturated soils, Comput. Geotech. 66 (2015) 126–141. https://doi.org/10.1016/j.compgeo.2015.01.002.

[35] S.P. Pradatta, Analytical expressions for determining the stability of cohesionless soil slope under generalized seismic conditions, Journal of Mountain Science 15.7, (2018): 1559-1571. https://doi.org/10.1007/s11629-017-4780-6.

Vol. 15, No. 45, Winter 2026, pages 35-50

Journal of Analytical and Numerical Methods in Mining Engineering

Journal home page: http://anm.yazd.ac.ir/

Research article

A multi-option RES-based model (MORESM) for selecting the optimum rock bolt system in underground coal mines

Sajjad Aghababaei[1], Hossein Jalalifar[1], Ali Hosseini[2], Mehdi Najafi[2]*

1- **Dept. of Mining Engineering, Shahid Bahonar University of Kerman, Kerman, Iran**
2- **Dept. of Mining and Metallurgy Engineering, Yazd University, Yazd, Iran**

*Corresponding author: E-mail: *mehdinajafi@yazd.ac.ir*
(Received: *June 2025*, Accepted: *November 2025*)

DOI: 10.22034/ANM.2025.23315.1687

Keywords

Rock bolt
Roof convergence
Rock engineering system (RES)
Multi-option RES-based model
Underground coal mines

Abstract

The research presents a method entitled MORESM based on the rock engineering system (RES) for selecting the optimum rock bolt (RB) for underground coal mines. This method introduces a new application of RES that simultaneously provides the possibility of comparing various options in rock engineering and validating the model based on the relevant hazards. The model is intended to operate based on routinely collected field data in underground coal mines and does not require specialized or costly testing equipment. The model is based on two key components: the interaction matrix, which determines the weights of effective system parameters, and the rating matrix, which evaluates the response level of each RB under various system conditions. The rating matrix is used to evaluate each RB's relative efficiency by analyzing its responses compared to other RBs across different conditions, without considering the strength factors of each rock bolt, such as load-bearing capacity. This approach is applicable when outcome validation is supported by field data. Here, six RB types are involved as six options, and the model is capable of determining the risk of applying (VI_{ap}) for each RB. In the following, a case study including 100 plus to 10 locations/cases of an underground coal mine was used to test and validate the MORESM. In this regard, the amounts of roof convergence (tell-tale displacement (TTD) at considered locations) are considered as the relevant hazard caused by increasing the VI_{ap} of applied (installed) RB. The results demonstrated that there is an acceptable correlation between the determined VI_{ap}s and corresponding TTDs, with a coefficient determination (R^2) of 0.765, and also the measured and predicted TTDs, with an R^2 of 0.803. The findings also indicated that when the applied RB is far from the optimal RB, instability increases just as much. This could be considered as a criterion for evaluating the performance of MORESM. Finally, it is proven that the model could be helpful to estimate the substitution time of the applied RB with a useful option, which is investigated for the case study.

1. INTRODUCTION

Underground coal mines have had the most use of rock bolt (RB) compared with other mining methods. The application of RBs has caused an increase in productivity and a decrease in support costs in these mines. In recent years, a significant number of RBs have been produced by companies (more than 35 types) for the support operation of underground excavations. Each of these products has various performances in various conditions of strata surrounding an underground space. Some of them are capable of covering a wide range of rock mass behaviors in support operations, and some can only be applied in limited conditions. Application of appropriate RB is a major challenge as the application of inappropriate options creates serious problems. So, it is necessary to present a comprehensive model for the selection of optimum RB.

The selection of RB type and their application conditions have been investigated by many

researchers. Mark and Barczak (2000) stated that the strength of rock, dependent on geology and the loads applied primarily by the in situ and mining-induced stresses, are two major factors to determine the type and specifications of the support system [1]. Mark et al. (2000) studied the performance of point-anchor tension and fully grouted resin RBs in different geological environments by field studies [2]. Mark (2000), developed an approach to design the roof bolt systems. Based on the Mark's research, roof support mechanisms are determined by stress level and roof quality which are determining factors in selecting the roof support system [3]. Parker (2001) emphasizes time as an effective factor and recommends using the resin/bar bolt for long-term support. Van der Merwe and Madden (2002) discussed support system selection in underground coal mines and summarized their results in two tables as a very general guide. They involved the rock quality, horizontal stress, and time as the determining factors to system selection in their charts[4]. Yassien (2003) released some advice on applying the appropriate bolt type. In these recommendations, the rock quality, the horizontal stress, the mining method, and the time are emphasized as the major effective factors for RB selection [5]. Canbulat et al. (2005) investigated the performance of four various RBs from different manufacturers in South Africa. They also studied the performance of the tensioned and un-tensioned bolts in different rock types. They explained Non-tensioned roof bolts achieved significantly greater bond strengths than the tensioned bolts in sandstone and shale roofs. They also concluded that the overall support stiffness of non-tensioned roof bolts was significantly greater than that of the tensioned roof bolts [6]. Jalalifar et al. (2009) proposed an AHP-Entropy-TOPSIS method for the pick of the optimum RB. They considered 15 major effective parameters (see Figure 2 of their paper) for choosing the best option from eight types of RB. They stated that selecting the suitable rock bolt is dependent upon the load transfer capacity, curing time, ease of installation, anchor length, cost, and distance from the heading face [7]. Spearing et al. (2010) conducted experimental studies on corrosion of rock anchors in US underground coal mines. They explained that corrosion would only seem to be a potential issue for long-term applications in coal mines [8]. Li et al. (2014) believe that the performance of an RB is dependent upon the loading conditions to which it is subjected[9]. Scolari e al. (2017) tested a new RB in deep mining conditions and achieved better results compared with a simple frictional, inflatable bolt. The new RB is based on a frictional, inflatable bolt combined with an internal additional load-bearing element, called the Dynamic Omega-Bolt [10]. Zhigang et al. (2017) proved the importance of using an energy-absorbing bolt for rock support in a high-stress rock mass [11]. Li (2017) noted that the suitable types of RBs for a given rock mass are associated with the loading conditions in the rock mass. The rock mass behavior under the induced stresses is the main criterion for bolt selection. Li explained that the traditional principle of selecting strong RBs is valid only in conditions of low in situ stresses in the rock mass. Energy-absorbing RBs are preferred in the case of high in situ stresses [12]. Song et al. (2017) discussed how smart sensor technologies can monitor rock bolt performance in real-time, enhancing the ability to select suitable bolts based on actual ground conditions and bolt health [13]. Sun et al. (2018) demonstrated that applying the yielding bolts is an effective way to support the soft rock roadway under high stress [14]. Wu et al. (2019) reached experimental results highlighting how rock bolts perform under dynamic coal burst conditions, emphasizing bolt strength and ductility as critical parameters for optimal selection in burst-prone mines [15]. Shaposhnik et al. (2021) demonstrated that friction-anchored rock bolts perform well in backfill environments, emphasizing the importance of frictional engagement in excavations with loose or unconsolidated fill [16]. Tshitema & Kallon (2022) focused on the development of a specialized reinforcing rock bolt for hard rock mines, demonstrating that material properties and rock mass interaction significantly influence bolt selection [17]. Frenelus et al. (2022) analyzed durability and long-term stability of rock bolts, highlighting environmental exposure and bolt design as crucial parameters for selecting bolts in deep rock tunnels [18]. Li et al. (2022) evaluated the influence of pretension on cable bolts, showing that optimal pretension enhances bolt load-bearing capacity, a key factor in bolt design and selection for diverse geological conditions [19]. Jiang et al. (2023) examined the mechanical behavior of fully grouted rock bolts in soft rock, emphasizing grout quality and bolt stiffness as decisive factors for their suitability in weak ground [20]. Demin et al. (2024) presented a new technology combining support and friction anchors, suggesting that combining anchoring mechanisms can optimize bolt performance in ore mine workings [21]. Mesutoglu & Ozkan (2024) compared rock bolting and steel arch supports in thick coal seams, finding that

geological conditions and load requirements heavily influence the selection between these support types [22]. Wang et al. (2025) investigated bolt support mechanisms for hard roof control, identifying bolt length, diameter, and installation parameters as key for optimizing rock bolt effectiveness [23]. Isfahani et al. (2025) applied 3D numerical modeling to optimize rock bolt support for large underground structures, stressing bolt layout and mechanical properties as pivotal in support design [24]. Zhou et al. (2025) introduced an anchoring approach grounded in pre-stress distribution within composite rock strata, emphasizing the role of pre-stress management in determining the optimal bolt anchoring method [25].

According to the literature review, understanding the rock mass behavior is very important for the selection of an appropriate RB type. Many parameters are involved in the rock mass behavior and loading conditions as each of them has different effects. Therefore, there is a system with three main components consisting of rock mass, loading conditions, and RB. These components have different factors. The interaction between rock mass and loading conditions determines the rock mass behavior. Also, the interaction between rock mass behavior and each RB has different responses. So, the performance of each RB in various rock mass behaviors is different, and the best response in support operation could be obtained by applying the most appropriate RB type. By using this theory, a model based on the rock engineering system (RES) is presented for the selection of optimum RB in underground coal mines. The RES method is adopted because of its ability to evaluate the interaction between the effective parameters in rock mass that this process leads to simulating the rock mass behavior. MORESM provides the possibility of evaluating the risk of using various types of RB in various rock mass behaviors. A schematic of the adopted theory for the selection of an optimum option is shown in Figure 1. In this Figure, VI is the vulnerability index or risk of applying the RB. The interaction matrix and rating matrix are elements of MORESM, which are introduced in the following.

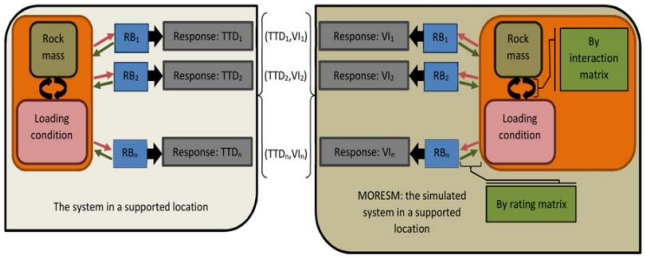

Fig. 1. A schematic of adopted theory for selection of optimum RB.

2. APPLIED METHOD AND PRESENTATION OF MORESM

Hudson (1992) presented an approach named rock engineering system (RES) for analyzing the interaction between effective parameters and components involved in rock mass for evaluating and answering complex engineering issues [26]. The RES determines and quantifies the interaction between parameters involved in a system. This process is conducted by an interaction matrix as a key element of RES (Fig. 2). An n*n interaction matrix is created by n parameters affecting the system. The off-diagonal positions in the matrix are filled by values describing the degree of interaction between the parameters. This research has adopted the "expert semi-quantitative" (ESQ) method (Hudson 1992) for numerically coding the interaction matrix, in such a way that 0 for no interaction, 1 for weak, 2 for medium, 3 for strong, and 4 for critical interaction, respectively. According to Figure 2, each particular parameter is denoted as coordinates (C, E). The interaction matrix helps in determining the weighting of each effective parameter within the system by Eq. (1).

$$a_i = \frac{(C_i + E_i)}{(\sum_{i=1}^{n} C + \sum_{i=1}^{n} E)} \times 100 \qquad (1)$$

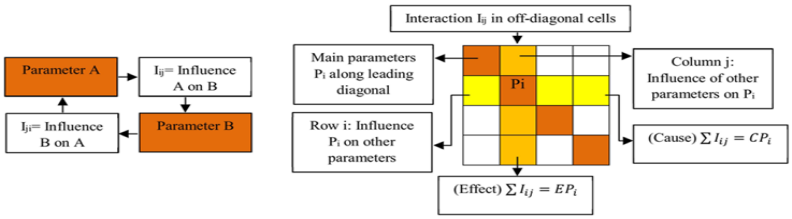

Fig. 2. A general view of interaction matrix, including principles of the interaction between parameters and the matrix coding (taken after Hudson (1992)) [26].

Based on the adopted theory and theory of the RES, the following steps are applied to determine the VI of applying (VI_{ap}) for each RB type:

- Determination of effective parameters on RB selection to consider the various behaviors of rock mass and to select an optimum option.
- Determination of weighting factor of each effective parameter in the system by Eq. (1).
- Determining the VI_{ap} by Eq. (2). When the VI_{ap} value is approaching 0 the risk level of the applying is lower, while its value approaching 100 shows that the risk level of the applying is higher.
- Testing and validating MORESM by field data. RBs with higher VI_{ap} have a lower performance in considered cases, which increases roof convergence, instability, and operation costs.
- Comparison of determined VI_{ap}s of different RB types and selecting an optimum option with help of auxiliary criteria.

$$VI = 100 - \sum_{i=1} a_i \frac{Q_i}{Q_{max}} \quad (2)$$

In this paper, six types of RB were taken into account based on the most applications in underground coal mines. The selection of these bolts, it is tries to cover the whole various strata behaviors in underground coal mines, from hard rocks in low-stress conditions to soft rocks in high-stress conditions. However, the selected RBs may not be comprehensive representatives, emphasizing this note that the main purpose of the paper is how to applying a method to choose the optimum RB. The six RBs are included such as mechanical expansion shell rock bolt (ES.RB), swellex rock bolt (S.RB), swellex-hybrid rock bolt (SH.RB), full-column slow/fast resin rock bolt (FCR.RB), point anchored resin rock bolt (PR.RB), and resin-grouted cone bolt (RG. CB). In this section, more than 30 RBs were investigated, and the selection was conducted based on parameters like type of point anchor part, genus, active or passive status, stiffness, needed time for pre-tensioning, delivery time of maximum load, lifetime, etc. Table 1 presents the investigated RBs with some of their characteristics.

2.1 Selection Of The Effective Parameters And Performing The Interaction Matrix

The interaction matrix was created by taking into account eight major parameters, which included the following: P1: coal mine roof rating (CMRR), P2: discontinuities formation (according to Figure 3), P3: induced-mining stress conditions (stress concentration factor), P4: the largest dimension of excavation, P5: conditions and location of the strong bed in the roof (distance from the roofline of excavation), P6: the ratio of bolt spacing to joint spacing, P7: the lifetime of excavation and P8: stress condition (degree of squeezing by Eq. (3) [27]. The six discontinuities formations include bedding without inclination and discontinuities (B1), inclined bedding without discontinuities (B2), jointed bedding by one joint set and without inclination (B1J1), inclined and jointed bedding by one joint set (B2J1), jointed bedding by two joint sets with no inclination (B1J2), and inclined and jointed bedding by two joint sets (B2J2).

These parameters were chosen to tackle a wide range of rock behavior and geotechnical conditions, including soft rock to hard rock, non-squeezing to squeezing, low to high-stress concentration, short to long time life for excavation, short to wide RB spacing, and shorter to wider excavation dimension and good to very bad conditions of discontinuities. The inclusion of excavation lifetime (P7) in the model allows the system to account for time-dependent deformation and fatigue in rock bolt performance, providing insight into temporal degradation effects across different excavation geometries and support durations. For this study, only the influence and interaction of rock mass and loading conditions on the reaction mechanism of RBs was considered and parameters such as the bearing capacity and elongation of RBs could be used as auxiliary criteria for final selection. As shown in Table 2 the interaction matrix was constructed to determine the contribution of each parameter in selecting the optimal RB. The interaction matrix values were derived through a structured expert elicitation process akin to the Delphi method, involving multiple rounds of feedback from six domain experts combined with a comprehensive literature review, to ensure consensus and robustness. The ai values for these parameters is illustrated in Figure 4.

Table 1. List of RBs (The six selected rock bolts are highlighted in green.)

No.	Rockbolt/Anchor name	Class	Type of point anchor part	Genus	Active/ Passive
1	Point anchored rock bolt (slot & wedge)	Mechanical	Slot & wedge	Steel	Active
2	Point anchored rock bolt (expansion shell)	Mechanical	expansion shell	Steel	Active
3	Roof truss	Mechanical/frictional/grouted	expansion shell/pint grouted	Steel	Active

4	Worley bolt	Frictional (deformable tube)	-	Steel	Passive
5	Split set/split-tube/friction stabilizer/swellex	Frictional	-	Steel	Passive
6	Power set self-drilling friction (expendable) bolts	Frictional	-	Steel	Passive
7	Swellex hybrid	Expendable set (frictional + mechanical)	-	Steel	Passive
8	Wooden dowels	Frictional	-	Wood	Passive
9	Fiber glass dowels/rockbolts	Frictional or grouted	-	GRP	Passive
10	Full-column concrete rockbolts (conventional bar or threadbar)	Cement grouted	-	Steel	Passive
11	Full-column concrete and fully threaded solid GRP bar	Cement grouted	-	GRP	Passive
12	Pre-tensioned cement fully-grouted rockbolts (conventional bar or threadbar)	Cement grouted +pre-tensioned	Cement grout	Steel	Active
13	Pre-tensioned cement semi-grouted rockbolts (conventional bar or threadbar)	Point + grouted	Cement grout	Steel	Active
14	Cement grouted expansion shell rockbolts (conventional bar or threadbar)	Mechanical + cement grouted	expansion shell	Steel	Active
15	Fully cement grouted and fully threaded self-drilling hollow GRP bar	Cement grouted	-	GRP	Passive
16	Perfo rocbolts	Grouted + frictional	-	Steel	Passive
17	Resin injected rockbolts (conventional bar or threadbar)	Resin grouted	-	Steel	Passive
18	Pre-tensioned resin fully-injected rockbolts: full-column slow/fast-resin combination bolts (conventional bar or threadbar)	Resin grouted + pre-tensioned	resin grout	Steel	Active
19	Point anchored resin-assisted mechanism anchor bolt (semi-injected) or pre-tensioned resin semi-injected anchor bolt (conventional bar or threadbar)	Mechanical + resin	resin grout	Steel	Active
20	Resin Grouted expansion shell rockbolts (conventional bar or threadbar)	Mechanical + resin	expansion shell	Steel	Active
21	Full-column resin and fully threaded solid GRP bar	Resin grouted	-	GRP	Passive
22	Full-column resin and fully threaded self-drilling hollow GRP bar	Resin grouted	-	GRP	Passive
23	Innovative constant resistance large deformation anchor bolt	Mechanical + frictional-energy absorption	Resin grout	Steel	Active
24	Cable bolts	Grouted (cement or resin)	-	Steel cable	Passive
25	Cable bolts	Cement or resin	Cement/resin anchor	Steel cable	Active
26	Resin capsulate cable bolts	Resin grouted	resin grout	Steel cable	Active
27	Yielding grouting rockbolt	Mechanical-grouted + yielding	Twist anchor head	Steel	Passive
28	Energy-absorbing rock bolts (such as con bolt)	Energy absorption	Mechanical (cone + deformable sleeve)	Steel	Passive
29	Dynamic omega-bolt (dynamic inflatable, friction rockbolt)	Energy absorption-inflatble	-	Steel	Passive
30	Spin to stall resin bolt	Resin grouted (self-spinning)	Resin cartridge	Steel	Passive

*GRP refers to glass reinforced plastic. The type of point anchor parts mentions RBs that anchored and pre-tensioned at the end part of RB by mechanical, frictional or grouted mechanism.

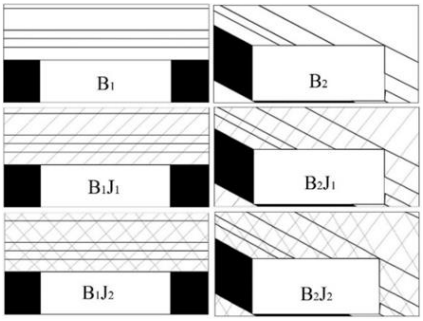

Fig. 3. Six considered categories of discontinuities formation around an underground coal mine gate for rating ranges of P2.

Table 2. Interaction matrix for the parameters affecting the selection of optimum RB in underground coal mines

P_1	3	0	2	0	3	1	1
3	P_2	0	2	0	3	1	1
0	0	p_3	1	0	2	1	0
0	0	3	P_4	0	2	2	2
3	0	0	1	P_5	1	0	1
1	1	0	1	0	P_6	0	1
0	0	0	2	3	1	P_7	0
1	2	2	0	0	3	1	P_8

$$N_c = \frac{\sigma_{cm}}{P_o} = \frac{\sigma_{cm}}{\gamma H} \quad (3)$$

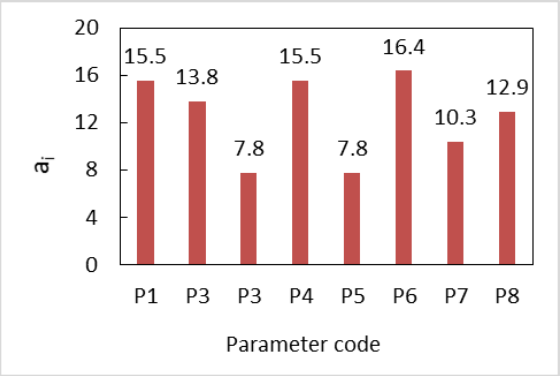

Fig. 4. Weighing of the principal parameters affecting the selection of optimum RB.

2.2 Presenting A New Rating Method For MORESM

In previous related research, the Q_i/Q_{max} in Eq. (2), was calculated by using a conventional rating method. In this method, one option or hazard was evaluated to calculate its associated risk. Several related studies are discussed here, including assessing the geotechnical hazards of TBM tunneling [28], prediction of rock fragmentation by blasting [29], risk analysis and prediction of out-of-seam dilution in longwall mining [30], risk analysis of floor failure mechanisms [31], and prediction of face advance rate in retreat longwall mining panel [32]. In this research, the rating of parameters' values has been carried out based on their effect on the considered hazard (for example, calculation of the out-of-seam dilution [30] or single option or factor (for example, face advance rate [32] to calculate the Qi/Qmax in Eq. (2).

In cases where there are several options/hazards to assess and multiple parameters (Pi) affect each option differently, the conventional RES rating method is not adequate, as it does not allow for the bidirectional prioritization needed for multi-hazard assessments. In this regard, MORESM should satisfy two purposes: first, the possibility of determining the VI_{ap} of various RBs in various conditions, and second, finding the relationship between VI_{ap}s and displacements in the roof. So, a new rating method was developed, named Hazard-Dependent Priority-Option Setting Rating (HPSR). The HPSR method introduces a two-dimensional rating approach that allows consistent prioritization of rock bolt options across varying parameter value ranges. This structure enhances adaptability in multi-hazard/options conditions, reduces subjectivity, and supports validation using routinely collected field data. This method was based on an m*n rating matrix formed by m value ranges of P_i and n options to achieve both of the above purposes (Fig. 5). HPSR introduces a structured two-dimensional rating process:

- Horizontally, it ranks the relative suitability of value ranges of each Pi for each option.
- Vertically, it ranks all options under each specific value range of Pi.

The maximum value in each rating matrix is considered as Qmax for corresponding Pi, which is used to calculate Qi/Qmax. This dual-axis rating allows for greater consistency in the prioritization process, prevents subjective inconsistencies by using a unified baseline (Qmax), and ensures adaptability across varying hazard/options conditions. Additionally, this structure enables validation through field data and avoids potential misjudgments that arise from using fixed or isolated scoring systems.

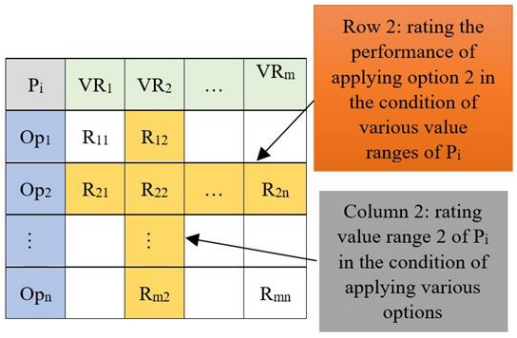

Fig. 5. Rating matrix for a MORESM; VR and Op are the value range and option, respectively.

In this research, eight rating matrices were formed based on the selected parameters, and six were considered for RBs. According to the investigations, experiences, and extensive literature review, the ratings of these matrices were carried out, and results are illustrated in Table 3 and Figure 6. In this figure, the legend for all graphs (a to f) is the same as the considered legend for graph (c). For P2, categorical discontinuity types were converted to numerical ratings through expert experience and literature-informed evaluation of their relative effects on RB performance under various geological conditions, ensuring consistency and practical applicability across different mining sites.

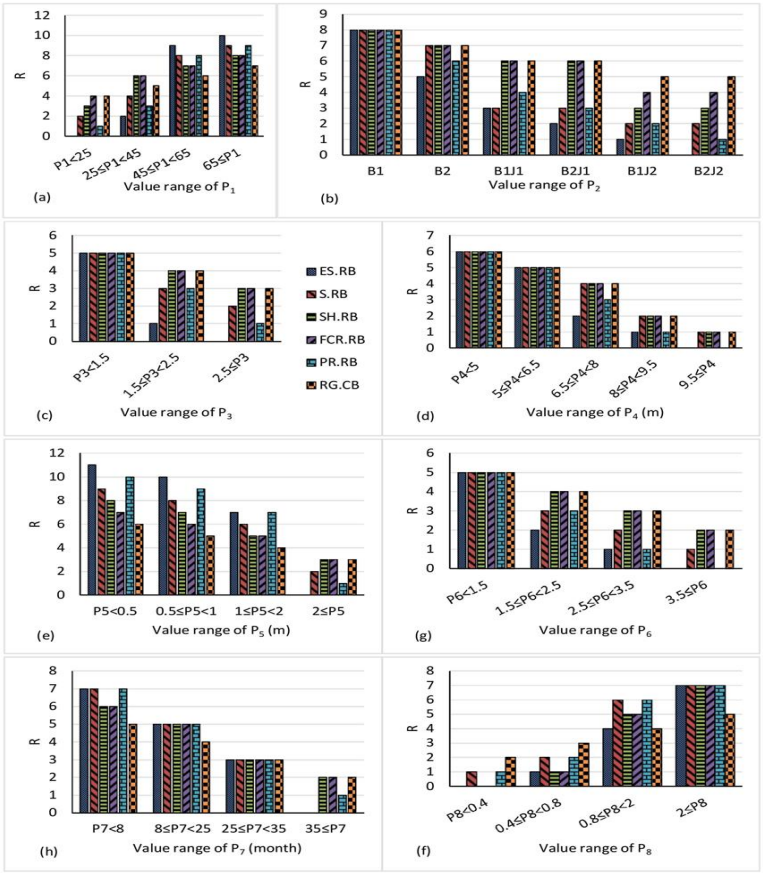

Fig. 6. Ratings of the P_1 to P_8 effect in VI_{ap} of RB in underground coal mines (a to f), obtained results from rating matrixes of the P_3 to P_8

Table 3. Assigning the values to rating matrix of P1 (CMRR)

P_1: CMRR	P_1<25 (very Weak)	25 ≤P_1<45 (Weak)	45≤P_1<65 (Moderate)	65≤P_1 (Strong)
ES.RB	0	2	9	10
S.RB	2	4	8	9
SH.RB	3	6	7	8
FCR.RB	4	6	7	8
PR.RB	1	3	8	9
RG.CB	4	5	6	7

In the following, a summary of adopted principles for rating and division of the parameters is presented. Ratings and divisions were carried out based on the experiences of experts and the literature review. In the presented graphs (Fig. 6), there is an ascending-descending trend in the all results. This trend indicates that worsening conditions for the parameters generally increase instability in the roof and applying extra load on the support system. Also, the best and worst options were specified for each considered range value of the parameters. In some value ranges, there is no priority for the options, which refers to the specified almost identical performance of the RBs in the considered class.

P1: Increasing the quality of roof strata causes increasing the self-supporting capability that creates minimum pressure on the support system. FCR.RB and RG. CB are the best options for soft rocks. The division of P1 was carried out in four value ranges based on the presented classification [33] which was divided into two classes, 0 to 25 and 25-45 for interval of 0 to 45, referring to very weak and weak strata, respectively.

P2: Discontinuities formation has a high effect on the mechanism of roof falls and requires supporting systems. The stability of the roof decreases with increasing the number of discontinuities and inclination of strata, which creates a hard condition for the support system, so that RG. CB and FCR.RB are the best options in a weak rock mass. P_2 was divided into six classes according to strata inclination and number of discontinuities sets in the roof.

P3: Increasing the induced stresses due to intense mining operation causes more failures and displacements in strata, so, it creates a hard condition for applying some RBs. Longwall mining with a roughly concentration factor of 2.5

around the operation area was considered as a scale for the division of P_3. ES.RB and PR.RB are appeared to have the worst performance in high induced stress conditions.

P4: A large dimension of excavation (width for roadways in coal mines) causes an increase in the height of the damaged zone in roof and changes the required support mechanism that generally provides a worse situation for applying RBs and so the worst options are ES.RB and PR.RB. These conditions lead to more and intense instabilities in the roof. The widest widths applied for the roadways, reached 9 to 10 m, and minimum widths are generally equal to 4 m. So, the division was adopted in the five classes.

P5: The existence of a strong bed near the roofline increases the loading capacity of the immediate roof. The presence of a strong bed beyond the first 2 m of roof makes a hard or impossible situation for applying the mechanical RBs to implement the suspension supporting mechanism. Based on these points, rating and value ranges of P_5 were determined.

P6: Generally, the large number of joints make a hard condition for the RBs, if it is the only component in the support system. Decreasing the bolt spacing to less than 1.5 times the joint spacing provides suitable conditions for applying the RBs. Resin bolts are the best options for an intensely jointed rock.

P7: The lifetime of the excavation is one of the determining factors for support design and bolt selection (based on the literature review). According to the lifetime of different excavations in underground coal mines and imposed situations by their application, four value ranges were considered for this parameter. Generally, increasing the lifetime makes a hard situation for apply the RBs. ES.RB and S. RB are not suitable options for long-term support.

P8: Increasing the degree of squeezing provides a hard condition for any support system. The division was carried out based on the present classification for the degree of squeezing based on Jethwa (1984) [27]. Energy-absorbing RBs are suitable options for highly squeezing rock conditions.

2.3 Application Procedure For MORESM In New Mines

To apply MORESM in a new mining environment, field engineers should:

- Collect comprehensive field data on rock mass properties, excavation characteristics (like geometry), installation conditions, and stress environments.
- Apply parameters calculable from the field data (both previously introduced and potentially new parameters) that represent rock mass properties, rock mass behavior, interactions created by excavation, and the hazard considered for model validation and optimization. These parameters should accurately simulate the relevant processes influencing the selection of the optimum option.
- Preprocess and organize the data according to MORESM input requirements and develop the model accordingly.
- Validate the model outputs against field observations to ensure accuracy and reliability.
- Use the validated model to select the optimum rock bolt options under varying site conditions.
- Successful implementation requires geomechanical knowledge, training on the MORESM methodology, and a time commitment for initial data collection and model calibration. Once established, MORESM provides a valuable decision-support tool for optimizing rock bolt selection.

3. CASE STUDY

To test and validate the presented MORESM, a case study consisting of 100 locations/cases of six panel gates (E0 TG, E_0 MG, E_2 TG, E_2 MG, E_3 TG, and E_3 MG) and two set-up rooms (E_0 Face and E_3 Face) were taken into account from longwall panels in Parvadeh-I coal mine (Fig. 7). These locations are the installation points of tell-tale extensometers in panel gates and set-up rooms. The required information of these cases was collected, and values of the effective parameters were determined for them. These cases have an approximately equal interval from together and cover various geological and geotechnical conditions. Information of 12 cases is presented in Tables 4 and 5. Table 6 provides a statistical description of the case study. The recorded convergence from tell-tales (TTD) consists of recorded values of part A and part B. Parts A and B indicate movement above and within bolted height, respectively. Three statuses of stress concentration factor ranging from less than 1.5, 1.5 to 2.5, and more than 2.5 were taken for considering various conditions of P_3 (induced-mining stress conditions). The corresponding lifetime (P_8) and the corresponding TTD were also determined for these three statuses. Lifetime refers to the life of the excavation from the time of creation to the time of recording the relevant

TTD. Therefore, with these three statuses, 197 cases/dataset were prepared to calculate VI_{ap}. It should be noted that in 197 cases, the recorded TTDs were available for 100 locations. To calculate the corresponding distance between longwall face and tell-tale for each range of stress concentration factor, information and presented results of longwall numerical modeling in Basic Design report of Parvadeh-I [34] were used.

Using measured and recorded field data collected along excavated spaces provides more reliable information and helps reduce uncertainties, while also capturing anisotropy better than other data collection methods. This approach compensates for spatial variability in rock mass conditions, such as anisotropy and fault proximity, by using parameter values averaged over short, well-defined roadway segments (straps) rather than individual points. These averages are based on frequent, systematic field measurements taken during routine operations, capturing localized geological variations. This method balances practical data collection constraints with the need to reflect spatial heterogeneity, providing robust and representative input for the model despite inherent variability [35-37].

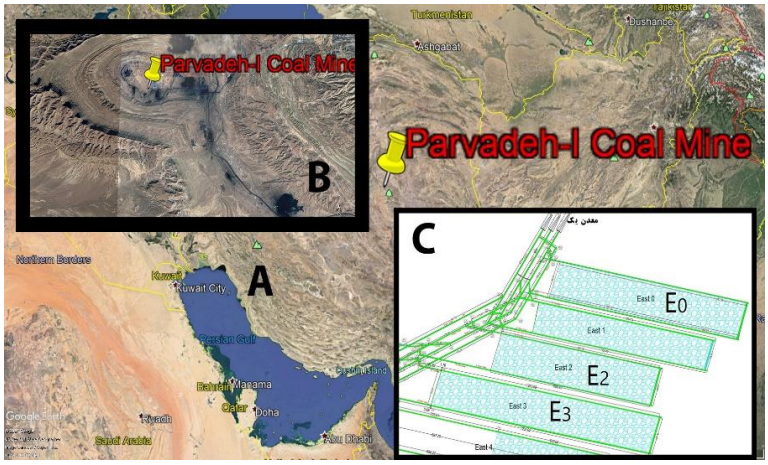

Fig. 7. A plan view of layout of the first longwall panels in Parvadeh-I coal mine, A and B show the location of Parvadeh-I, and C show the plan of considered longwall panels.

Table 4. Information of 12 locations from considered case study

Panel	Exc. type	Strap No.	Tell-tale No.	Depth (m)	P1: CMRR	P_2	P_4	P_5	P_6	P_8
E_0	TG	900	77	55.00	40.1	B2	4.5	No Present	No joint	3.26
E_0	TG	170	15	90.00	22.4	B2J1	4.5	No Present	0.40	2.56
E_0	MG	1150	72	160.00	31.8	B2J1	5.0	No Present	1.82	0.89
E_0	MG	900	54	135.00	40.1	B2	5.0	No Present	No joint	1.33
E_2	TG	1010	59	230.00	23.5	B2J2	4.5	No present	6.29	0.43
E_2	TG	368	27	200.00	16.4	B2	4.5	No present	No joint	0.81
E_2	MG	1079	68	300.00	1.5	B2J1	5.0	No Present	15.38	0.54
E_2	MG	833	46	270.00	34.3	B2J1	5.0	No Present	0.75	0.76
E_3	TG	1300	93	365.00	28.7	B2J1	4.5	No present	2.50	0.28
E_3	TG	918	64	330.00	40.1	B2J1	4.5	No Present	0.41	0.63
E_3	MG	1590	113	440.00	18.9	B2J1	5.0	No present	0.96	0.53
E_3	MG	1168	80	390.00	28.7	B2J1	5.0	No present	2.56	0.37

Table 5. Information of 12 locations from considered case study (Continuation of Table 4)

Panel	Exc. type	Strap No.	P_3 Status 1	P_7 Status 1	related TTD (mm) Status 1	P_3 Status 2	P_7 Status 2	related TTD (mm) Status 2	P_3 Status 3	P_7 Status 3	related TTD (mm) Status 3
E_0	TG	900	<1.5	12.5	0	1.5-2.5	12.8	0	2.5≤	12.9	0
E_0	TG	170	<1.5	23.9	1	1.5-2.5	24.1	1	2.5≤	24.3	1
E_0	MG	1150	<1.5	3.6	0	1.5-2.5	3.7	9	2.5≤	4.0	14

E_0	MG	900	<1.5	4.2	0	1.5-2.5	4.5	0	2.5≤	5.0	2
E_2	TG	1010	<1.5	28.6	81	1.5-2.5	34.3	110	2.5≤	35.0	132
E_2	TG	368	<1.5	57.8	21	1.5-2.5	58.8	30	2.5≤	58.9	42
E_2	MG	1079	<1.5	33.4	190	1.5-2.5	36.6	457	2.5≤	37.1	556
E_2	MG	833	<1.5	46.5	60	1.5-2.5	48.1	83	2.5≤	48.2	94
E_3	TG	1300	<1.5	9.3	15	1.5-2.5	10.6	84	2.5≤	10.7	100
E_3	TG	918	<1.5	22.6	28	1.5-2.5	24.1	28	2.5≤	24.2	52
E_3	MG	1590	<1.5	4.7	11	1.5-2.5	6.2	14	2.5≤	6.2	25
E_3	MG	1168	<1.5	16.4	40	1.5-2.5	17.2	82	2.5≤	17.5	140

Table 6. Statistical description of the case study

Parameters name/code	Ave.	Min	Max	St. Dev.
P_1	32.16	1.5	40.1	8.67
P_2	Nominal	-	-	-
P_4 (m)	4.99	4.5	7	0.71
P_5 (m)	2<	2<	2<	-
P_6	1.88	0.20	15.38	2.55
P_7 in condition of P_3<1.5 (month)	21.97	0.55	61.59	16.37
P_7 in condition of P_3=1.5-2.5 (month)	26.28	3.70	63.20	18.60
P_7 in condition of 2.5≤P_3 (month)	30.50	4.00	63.55	18.79
P_8	0.99	0.28	3.26	0.76
TTD (mm) in condition of P_3<1.5	25.36	0	216	38.16
TTD (mm) in condition of P_3= 1.5-2.5	52.03	0	457	77.55
TTD (mm) in condition of 2.5≤P_3	80.94	0	556	107.24

4. MORESM VALIDATION

To evaluate MORESM's performance and capability, the model was considered in the case study. In this regard, VI_{ap} of each RB type was determined for all the locations of the case study in Parvadeh-I mine, and results are illustrated in Table 7 and Figure 8. As it can be seen, FCR.RB, SH.RB and RG. CB are the best options for the considered case study, respectively. These results are affected by the geomechanical conditions of the considered site, as soft rocks under stresses increasing with depth. According to the outputs, RG. CB is the optimum selection in E_2 MG, E_3 TG, E_3 MG, and E_3 Face, which results from variation of low-stress conditions to high-stress conditions in soft rocks due to increasing the depth. In these conditions, energy-absorbing of RBs displayed better performance in controlling the roof strata. Although, the difference between VI_{ap}s of FCR.RB, SH. RB, and RG. CB is low. On the other side of these investigations, mechanical RBs have the lowest performance for all considered locations. According to the results of Table 7, the uncertainty bounds for VI_{ap} values were quantified using 95% confidence intervals, with margins of error ranging from ±0.75 to ±1.63 units across the six RBs. These translate to relative errors of approximately 2.3% to 3.8%, indicating that the MORESM model predicts optimum support systems with an estimated error margin of about ±3%, demonstrating high confidence in the model's accuracy and reliability.

Table 7. Description of all calculated VIap for the RBs in Parvadeh-I coal mine

RB code	Ave. VI_{ap}	Min VI_{ap}	Max VI_{ap}	St. Dev.	Margin of Error	CI lower bound	CI upper bound	Relative Error%
ES.RB	51.78	28.3	81.77	11.64	1.64	50.15	53.42	3.16
S.RB	40.08	20.34	67.31	10.78	1.51	38.56	41.59	3.78
SH.RB	32.83	16.53	53.94	8.31	1.17	31.66	34.00	3.56
FCR.RB	32.37	16.53	52.39	7.99	1.12	31.25	33.49	3.47
PAR.RB	43.39	24.32	72.92	10.88	1.53	41.86	44.92	3.52
RG.CB	32.86	23.25	48.7	5.31	0.75	32.11	33.61	2.27

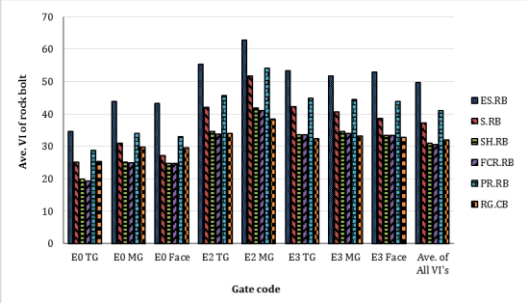

Fig. 8. Average VIap for each RB type in the panel gates in Parvadeh-I coal mine.

For validation and identification of the model performance, the relationship between the determined VI_{ap}s of applied RB in Parvadeh-I mine and the corresponding recorded TTDs were investigated, and results are presented in Figure 9. In the following, a dataset including 14 locations/cases (see 10 locations in Table 8) located in all three desired panels is involved to test the ability of the model to predict the TTD for new locations. Figures 10 and 11 depict the comparison of predicted TTDs with the measured TTDs at the site. In this step, root mean squared error (RMSE) and mean absolute error (MAE) were used to assess the accuracy of fitted models and outcomes, which were formulated in Eqs. (6) and (7). The obtained values of 0.803, 54.8, and 13.8 for R^2, RMSE, and MAE, respectively, which are acceptable and consistent with the scale of the data.

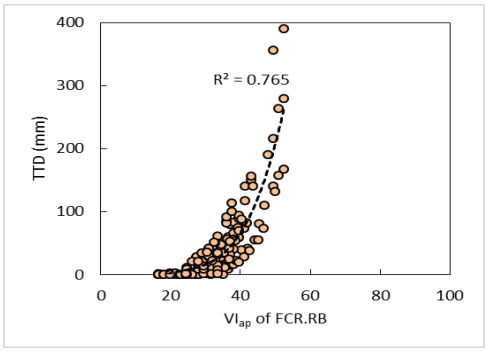

Fig. 9. Relationship between the VIaps of applied RB and corresponding recorded TTDs, polynomial and linear regression analyses.

$$RMSE = \sqrt{\frac{1}{n}\sum_{i=1}^{n}(y_i - y_i^*)^2} \quad (6)$$

$$MAE = \frac{1}{n}\sum_{i=1}^{n}|(y_i - y_i^*)| \quad (7)$$

Table 8. Information of the 10 considered cases/locations to test the ability of MORESM for TTD prediction

Case No.	P_1	P_2	P_4	P_5	P_6	P_8	P_7 Status 1	TTD Status 1	P_7 Status 2	TTD Status 2	P_7 Status 3	TTD Status 3
1	40.1	B2	4.5	No present	NJ	NJ	22.3	3	22.9	3	MD	MD
2	40.1	B2	5.	No present	NJ	NJ	3.6	0	3.84	4	MD	MD
3	40.1	B2	5.0	No present	NJ	NJ	9.27	0	MD	MD	MD	MD
4	40.1	B2	7.0	No present	NJ	NJ	5.5	2	MD	MD	MD	MD
5	25.6	B2J1	4.5	No present	0.32	0.60	33.17	18	37.11	38	37.77	57
6	16.4	B2	4.5	No present	NJ	NJ	55.59	35	56.5	45	56.77	105
7	32.1	B2J1	5.0	No present	1.88	0.76	44.7	42	46.19	54	46.6	77
8	40.1	B2J1	4.5	No present	0.55	0.63	24	18	25.9	24	MD	MD
9	36.3	B2J1	5.0	No present	0.77	0.43	10.12	14	10.84	14	MD	MD
10	40.1	B2J1	5.0	No present	0.21	0.51	21.9	2	MD	MD	MD	MD

MD means that information of TTD corresponding to the considered status was not measured or was not found in the reports. NJ means No joint. P3 values for three statues are similar to those considered in Table 5. According to MD data, 20 VIs were determined for the related process.

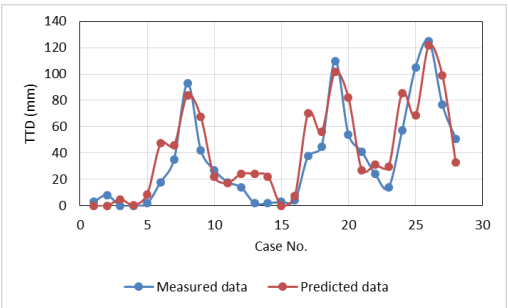

Fig. 10. Relationship between the measured and predicted TTD.

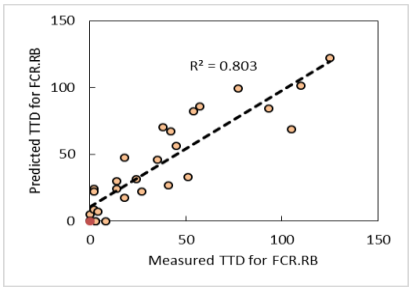

Fig. 11. Relationship between the measured and predicted TTD.

Increasing the difference between the VI_{ap} of applied RB and VI_{ap} of optimum RB (VI_{op}) leads to the lower performance of selected RB, which causes more instability and convergence in the roof. According to this concept, the relationship of the difference between the VI_{ap} of applied RB and VIop with the corresponding TTD was obtained, and outcomes are shown in Figure 12. The graph shows a non-linear ascending trend that indicates an increase in the TTD because of applying a non-optimal option. The highest difference between the applied RB and optimum RB was determined for E2 MG with very weak rocks under vertical stress of 6.62 to 7.85 MPa. In return, E0 TG, E0 MG, and E0 face showed the least difference (zero) in weak rocks under vertical stresses of 1.35 to 4.17 MPa.

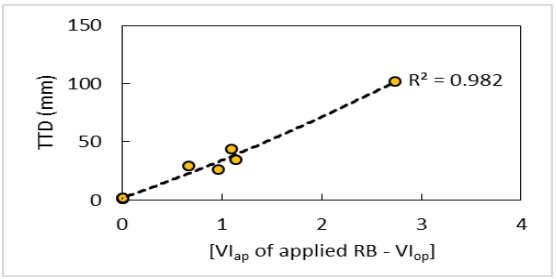

Fig. 12. Relationship of the difference between VIap of applied RB and VIop with the corresponding TTD for each considered gate, average amount for each gate, a polynomial regression analysis.

Considering the substitution time of the support system type (in this study, the type of rock bolt) has been one of the challenges that engineers encounter in mines with various geological and geotechnical conditions. One of the abilities of MORESM is estimating the substitution time (depth) of RBs according to the new requirements due to changing geological conditions versus depth. This challenge is investigated in the current study by the defined model and the results are illustrated in Figure 13. For this aim, the relationship of the difference between VI_{ap} of applied RB (FCR.RB) and VI_{ap} of RG. CB with the corresponding TTD was investigated (Fig. 13). RG. CB was selected due to its capability for supporting the soft rock strata under high-stress conditions. The results in the graph indicate that there is an ascending trend between the increase of the difference and the depth. Displacement in the roof is increased by the difference between the applied RB and the target bolt. It demonstrates that the trend is going towards the substituting FCR.RB with RG.CB. Estimating the corresponding depth of substitution time could be determined by following the trends of results where the VI_{ap} of applied RB (FCR.RB) is more than VI_{ap} of RG.CB.

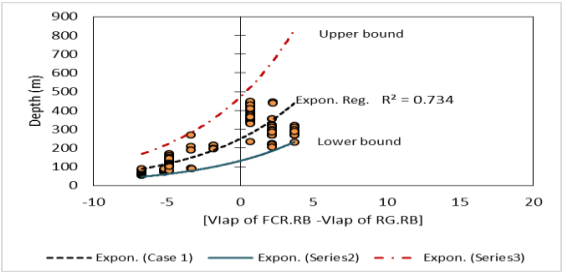

Fig. 13. Relationship of the difference between VIap of applied RB (FCR.RB) and VIap of RG. CB with the corresponding TTD, an exponential regression analysis with upper and lower bounds (confidence factor 95%).

5. DISCUSSION

Analyzing the results of the interaction matrix determines priorities for the selection of the optimum RB. There are other effective parameters in selecting optimum RB that could be involved and examined. Therefore, the obtained results indicated the importance of each parameter among the eight considered parameters based on several expert surveys in completing the interaction matrix. MORESM only includes geological and geotechnical parameters. The influence of other effective parameters, such as the loading capacity of RB, the accessibility of related products of RBs, etc., should be applied using the auxiliary criteria. This research has prioritized the performance of RB in rock mass for selecting an optimum option (see sections 1 and 2). The authors have believed that involving the economic parameters and some operational parameters can produce unanalyzable results and cause deviation from the research priority.

The obtained results of MORESM validation showed that the presented rating method to calculate the VI_{ap} is well recognized to achieve the desired purposes, including determining the VI_{ap} of various options in various conditions and finding the relationship between the VI_{ap} and the instability in the roof. There are a lot of issues and uncertainties in rock engineering that necessitate comparing the various options or hazards with each other to solve and understand the problem. This rating method could increase the capability of RES to solve such complicated problems and issues. However, the conventional rating method only allows the researcher to study one hazard or option. This method could be further explored and supplemented.

Based on the average VI_{ap} of FCR.RB, SH.RB and RG. CB, considering an auxiliary criterion for the final decision is helpful. Generally, the simplicity of accessibility to products of the selected RB is an important factor that is considered by mining companies. Although when they are faced with a long-life project, investing

to buy or produce the best option has a lot of benefits against the related operational costs of a non-optimal RB. In connection with selecting optimum RB, the main purpose is the investigation of more types of RB involving all possible effective parameters. In this regard, the results of this study indicated that reaching the aim is feasible.

By considering positive functions of the model based on the results in Figures 9 to 12, the provided new application of RES could be applied for various cases and sites, under further investigations. The amounts of R^2 between the VI_{ap}s of applied RB and the corresponding recorded TTDs demonstrated that MORESM has shown acceptable performance. However, the ability to predict TTD is one of the major criteria for validation of MOREM, but it should be noted that the main purpose is to determine an optimum RB with expected high performance. Investigating the relationship of the difference between the VI_{ap} of applied RB and the VI_{ap} with the corresponding TTD could also be one of the applicable criteria for validating the performance of an optimizer model. Results from Figure 12 specified that the instability in the roof is increased with increasing the distance of the applied option from the optimum one. The difference is high for locations with weak to very weak rocks under relatively low to high-stress conditions. It refers to the locations with a degree of squeezing lower than 0.7. This finding provides a tool to investigate the capabilities of the other RBs to substitute with the current system. In this regard, as is mentioned before, rock mass behavior is going to the soft rock under high-stress conditions with increasing the depth of mining in Parvadeh-I mine. The upper bound in Figure 13 can be introduced as the latest time to substitute the applied RB with the optimal RB, which indicates a depth of about 500 m as the substitution depth. RG. CB, as the optimal RB for the case study, has better performance than FCR.RB, as the applied RB, in rock mass with soft rocks under high stresses. Latest reports indicate that there is a very large pressure on support arches and floor heave in some roadways in depths of more than 500 meters in Parvadeh-I. The depth of 500 m in Parvadeh-I is where the degree of squeezing is approximately lower than 0.53. This technique could be used in other support systems and even other sections in mines; however, it needs to be further investigated. Lack of timely assessment and substitution of the current support system with a more suitable one can lead to operational issues such as increased roof convergence, floor heave, higher operational costs, and reduced advancement rates.

The issue of RB selection has not been studied in this way in any of the previous studies (based on the literature review). Other researchers have often focused on examining the influence of technical parameters on the performance of different types of RBs, the parameters influencing the selection of RBs, and the performance of RBs in the field and laboratory conditions. Although each of these studies has provided valuable results. The present article showed that it is possible to apply all the worthwhile results of these studies to propose a comprehensive model.

While MORESM presently operates deterministically, future versions could incorporate probabilistic methods, such as Monte Carlo simulations or Bayesian RES, to better capture uncertainty in input parameters like rock mass characteristics, stress conditions, and more. This enhancement would improve the robustness and reliability of the model in complex geomechanical settings.

In addition to the core mechanical factors modeled by MORESM, practical considerations such as installation ease and grout curing properties play a crucial role in field applications. These factors are best treated as auxiliary criteria to support final decision-making. Corrosion, given its influence on rock bolt durability, represents an important aspect that could be integrated into future versions of the model to enhance its predictive capability.

6. CONCLUSIONS

This research introduces a novel application of the Rock Engineering System (RES) for selecting the optimum rock bolt (RB) among various types. The main results and conclusions are summarized as follows:

- The proposed model relies on two fundamental components: an interaction matrix assigning weights to influential system parameters, and a rating matrix assessing each RB's performance under varying system conditions. The rating matrix enables comparative evaluation of RB effectiveness by examining relative responses without directly incorporating strength characteristics such as load-bearing capacity. This approach is particularly effective when validated against empirical field data.
- The training model was developed using data collected from 114 locations (197 cases under three stress conditions). The fitted

model demonstrates an expected, stable trend without fluctuations or oscillations and with an R^2 of 0.765. Validation across 14 additional locations (28 cases) further confirmed MORESM's effectiveness for comparing RB options. Validation metrics include: correlation between VI_{ap} of applied RBs and recorded total tunnel displacements (TTD) (R^2 = 0.765); correlation between measured and predicted TTDs (R^2 = 0.803, RMSE = 54.8, MAE = 13.8); and a novel metric correlating the difference between VI_{ap} of applied and VI_{ap} of optimum RBs with corresponding TTDs (R^2 = 0.982), offering a new scale for optimizer model assessment.

- MORESM's ability to be validated with field data is a significant advantage. The model can determine the optimal RB, evaluate the performance of different RBs at a site, analyze installed RB conditions, and estimate substitution timing for more suitable support systems.
- A new feature leverages the relationship between differences in VI_{ap} values of applied and optimum RBs and their corresponding TTDs to estimate substitution time for replacing the current support system with a more suitable option under evolving rockmass and stress conditions. For the case study, an approximate substitution depth of 500 m was identified, coinciding with hazards such as floor heave and severe roof convergence around this depth.
- While theoretical support for a causal relationship is provided by this study and prior work (Aghababaei et al., 2020), further experimental studies and long-term monitoring are needed to conclusively confirm the causality between the difference in VI_{ap} of applied and optimum options (e.g., rock bolt, as examined in the current research) and its potential use as a predictor of hazards such as roof convergence.
- The model's repeatability has been validated to ensure robustness against varying expert inputs and site data, recognizing that legitimate geological changes—especially at greater depths—may lead to different optimum RB selections.
- Given that mining challenges often involve hazards and ground response measurable by advanced tools, the method is adaptable to other issues and environments, provided validation against measured data. Though developed for coal mines and specific RB types, MORESM can be calibrated for metalliferous mines or civil tunneling projects using site-specific data.
- MORESM incorporates induced mining stress conditions related to advancing longwall faces, but its real-time adaptability to rapidly evolving stress environments (e.g., sudden face advances or longwall retreats) requires further validation.
- Although sensitivity analysis of input parameter weights is acknowledged as important, this study primarily introduces and validates the RES-based framework for rock bolt selection.
- The core of this research focuses on the interaction mechanisms between RBs and surrounding strata under varying rock mass and stress conditions. In cases with similar model results for different RBs, auxiliary criteria such as cost, bearing capacity, or operational factors may guide the final selection.
- Finally, MORESM is presented as a promising model for further investigation and application rather than a fully validated, finalized method.

List Of Symbols

C_i	Cause of the ith parameter
E_i	Effect of the ith parameter
a_i	Weighting factor of ith parameter
VI	Vulnerability index (refers to risk of applied/applying the rock bolt)
Q_i	Value (rating) of the ith parameter
Qmax	Maximum value assigned for ith parameter (normalization factor)
Nc	Degree of squeezing
σ_{cm}	Rock mass uniaxial compressive strength
Po	In situ stress
γ	Rock mass unit weight
H	Tunnel depth below surface
CF	Cost factor of rock bolt
c	Costs of rock bolt including purchase and installation
D	Discount rate
NE	lifetime of considered location where the applied rock bolt is installed
BCF	Bearing capacity factor of rock bolt
P	Maximum bearing capacity of rock bolt
L	Length of rock bolt
RB	Rock bolt
TTD	Recorded roof convergence from tell-tale extensometer
MORESM	Multi-option RES-based model

REFERENCES

[1] Mark C, M and Barczak, T. (2000): Fundamentals of coal mine roof support. Proceedings: New Technology For Coal Mine Roof Support, National Institute for Occupational Safety and Health, Pittsburgh Research Laboratory, Pittsburgh, PA, Information Circular 9453, p 23-42.

[2] Mark, C., Dolinar, D and P. Mucho, T. (2000): Summary of field measurements of roof bolt performance. Proceedings: New Technology For Coal Mine Roof Support, National Institute for Occupational Safety and Health, Pittsburgh Research Laboratory, Pittsburgh, PA, Information Circular 9453, p 81-86.

[3] Mark, C. (2000): Design of roof bolt systems. In: New technology for coal mine roof support. Pittsburgh, PA: U.S. Department of Health and Human Services, Public Helath Service, Centres for Disease Control and Prevention, National Institute for Occupational Safety and Health DHHS, (NIOSH) Publication No. 2000-151, IC 9453, p 111-131.

[4] Parker, J: (2001): Selecting a roof bolting system. Part 2, AGGMAN, November, pp. 16-21.

[5] Yassien, A.M. (2003): 2-D numerical simulation and design of fully grouted bolts for underground coal mines. PhD Thesis. West Virginia University, Morgantown. 180 pp.

[6] Canbulat, I., Wilkinson, A., Prohaska, G., Minsi, M and Singh, N. (2005): An investigation into the support systems in South African collieries. CSIR Division of Mining Technology, Report No: CR231/0205/SIM302.

[7] Jalalifar, H., Behaadini, M and Aghajani B. A. (2009): The optimum rock bolt support system selection by using AHP-Entropy-TOPSIS method. Journal of mines, metals & fuels. Iss9 Vol 57: 251-266.

[8] Spearing, A.J.S., Mondal, K and Bylapudi G. (2010): Experimental studies on corrosion of rock anchors in US underground coal mines. Journal of Transactions of the Society of Mining, Metallurgy, and Engineering, Vol. 328, PP 556-563.

[9] Li C. C., Stjern, G and Myrvang, A. (2014): A review on the performance of conventional and energy-absorbing rockbolts. J Rock Mech Geo Eng. http://dx.doi.org/10.1016/j.jrmge.2013.12.008.

[10] Scolari, F., Brandon, M and Krekula, H. (2017): Dynamic inflatable, friction rockbolt for deep mining. International Conference on Deep and High Stress Mining, Australian Centre for Geomechanics, Perth, ISBN 978-0-9924810-6-3.

[11] Zhigang, T., Fei, Z., Hongjian, W., Haijiang, Z and Yanyan, P. (2017): Innovative constant resistance large deformation bolt for rock support in high stressed rock mass. Arab J Geosci. DOI 10.1007/s12517-017-3127-5.

[12] Li C.C. (2017): Principles of rockbolting design. J Rock Mech & Mining Sci. http://dx.doi.org/10.1016/j.jrmge.2017.04.002.

[13] Song, G., Li, W., Wang, B., & Ho, S. C. M. (2017): A Review of Rock Bolt Monitoring Using Smart Sensors. Sensors, MDPI, vol. 17, no. 4, p. 776, https://doi.org/10.3390/s17040776.

[14] Sun, X., Wang, L., Lu, Y., Jiang, B., Li, Z and Zhang, J. (2018): A yielding bolt — grouting support design for a soft-rock roadway under high stress: a case study of the Yuandian No. 2 coal mine in China. The journal of the Southern African Institute of Mining andMetallurgy. ttp://dx.doi.org/10.17159/2411-9717/2018/v118n1a9.

[15] Wu, Y., Gao, F., Chen, J. (2019): Experimental Study on the Performance of Rock Bolts in Coal Burst-Prone Mines. Rock Mechanics and Rock Engineering, Springer, 52, 3959–3970 (2019). https://doi.org/10.1007/s00603-019-01794-9.

[16] Shaposhnik, Y.N., Konurin, A.I., Neverov, A.A. et al. Validation of Friction-Anchored Rock Bolt Supports for Underground Excavations in Backfill. (2021): J Min Sci 57, 775–786. https://doi.org/10.1134/S1062739121050070

[17] Tshitema, N., & Kallon, D. V. V. (2022): Product Development of a Rock Reinforcing Bolt for Underground Hard Rock Mining. Mining, MDPI, 1(3), 364-390. https://doi.org/10.3390/mining1030023.

[18] Frenelus, W., Peng, H., & Zhang, J. (2022): An Insight from Rock Bolts and Potential Factors Influencing Their Durability and the Long-Term Stability of Deep Rock Tunnels. Sustainability, MDPI, vol. 14, no. 17, p. 10943, https://doi.org/10.3390/su141710943.

[19] Xu Li, Guangyao Si, Joung Oh, Peter Corbett, Terri O'Sullivan, Zizhuo Xiang, Naj Aziz, Ali Mirzaghorbanali. (2022): Effect of Pretension on the Performance of Cable Bolts and Its Optimization in Underground Coal Mines with Various Geological Conditions. International Journal of Rock Mechanics and Mining Sciences, Elsevier, Volume 152, 2022, 105076, ISSN 1365-1609, https://doi.org/10.1016/j.ijrmms.2022.105076.

[20] Jiang, H., Li, S., Li, Q., & Xu, J. (2023): Mechanical Behavior of Fully Grouted Rock Bolts in Soft Rock Conditions. Tunnelling and Underground Space Technology, Springer, 13(5), 1280. https://doi.org/10.3390/buildings13051280.

[21] Demin, V., Kalinin, A., Baimuldin, M., Tomilov, A., Smagulova, A., Mutovina, N., Shokarev, D., Aliev, S., Akpanbayeva, A., & Demina, T. (2024): Developing a Technology for Driving Mine Workings with Combined Support and Friction Anchors in Ore Mines. Applied Sciences, MDPI, vol. 14, no. 22, p. 10344, https://doi.org/10.3390/app142210344.

[22] Mesutoglu, M., Ozkan, I. (2024): Evaluation and Comparison of Rock Bolting Versus Steel Arch Support Systems in Thick Coal Seam Underground Galleries: A Case Study. Mining, Metallurgy & Exploration, Springer, 41, 1719–1737 (2024). https://doi.org/10.1007/s42461-024-00994-4.

[23] Wang, C., Zheng, X., Xin, W., Wang, J., & Liu, L. (2025): Investigation of Bolt Support Mechanisms and Parameter Optimization for Hard Roof Control in Underground Mining. Processes, MDPI, 13(1), 94.

[24] Isfahani, N. S., Azhari, A., Motra, H. B., Hashemalhoseini, H., Hosseinabadi, M. H., Baghbanan, A., & Bazargan, M. (2025): Optimizing Rock Bolt Support for Large Underground Structures Using 3D DFN-DEM Method. Geosciences, MDPI, vol. 15, no. 8, p. 293, https://doi.org/10.3390/geosciences15080293.

[25] Zhou, Y., Yang, J., Zhang, C., Li, D., & Hu, B. (2025): Selection of an Optimum Anchoring Method of Composite Rock Stratum Based on Anchor Bolt Support Prestress Field. Applied Sciences, MDPI, 15(13), 6990.

[26] Hudson, JA. (1992): Rock engineering systems: theory and practice. Chichester: Ellis Harwood.

[27] Jethwa, J.L., and Singh, B. (1984): Estimation of ultimate rock pressure for tunnel linings under squeezing rock conditions – a new approach.Design and Performance of Underground Excavations, ISRM Symposium, Cambridge, E.T. Brown and J.A.Hudson eds., pp. 231-238.

[28] Benardos, AG and Kaliampakos, DC. (2004): A methodology for assessing geotechnical hazards for TBM tunneling-illustrated by the Athens Metro, Greece. Int J Rock Mech Min Sci 41: 987–999.

[29] Faramarzi, F., Mansouri, H and Ebrahimi Farsangi, MA. (2013): A rock engineering systems based model to predict rock fragmentation by blasting. Int J Rock Mech Min Sci 60:82–94.

[30] Bahri Najafi, A., Saeedi, G and Ebrahimi Farsangi, MA. (2014) Risk analysis and prediction of out-of-seam dilution in longwall mining. Int J Rock MechSci 70: 115-122.

[31] Aghababaei, S., Saeedi, G and Jalalifar H. (2015): Risk analysis and prediction of floor failure mechanisms at longwall face in parvadeh-I coal mine using rock engineering system (RES). Int J Rock Mech Rock Eng. DOI 10.1007/s00603-015-0884-x.

[32] Aghababaei, S., Jalalifar H and Saeedi, G. (2019) Prediction of face advance rate and determination of the operation efficiency in retreat longwall mining panel using rock engineering system. Int J Coal Sci Technol. DOI 10.1007/s40789-019-0245-6.

[33] Mark, C., Chase, F.E and Molinda, G.M. (1994): Design of longwall gate entry systems using roof classification. Paper in New Technology for Longwall Ground Control: Final Proc. USBM Technology Transfer Seminar, USBM SP 94-01, pp. 5–18.

[34] IRASCO, IRITEC, Cementation SKANSKA. (2005): Basic design report. Parvadeh, Tabas Coal Mine Project, Iran.

[35] Hosseini, A., Najafi, M. and morshedy, A. H. (2022). The effect of technical parameters of cross-measure boreholes methane drainage method on the amount of exhaust gas (Case study: Tabas Parvadeh coal mine No.1). *Journal of Analytical and Numerical Methods in Mining Engineering*, 12(30), 79-89. doi: 10.22034/anm.2022.2570

[36] Faramarz,A,Saeedi, G., Hosseini, A. and Aghababaei, S. (2025). Prediction and Optimization of Roadheader Performance based on Characteristics and Geo-Mechanical Parameters of Rock (Case Study: TABAS Parvedeh coal mine No. 1). *Journal of Analytical and Numerical Methods in Mining Engineering*, doi: 10.22034/anm.2025.21296.1628.

[37] Eslamzadeh, M., Ataei, M., Sereshki, F. and Najafi, M. (2022). Predicting the coal production rate of shearer device based on the gas properties and coal Strength in Tabas No. 1 Parvade coal mine. *Journal of Analytical and Numerical Methods in Mining Engineering*, 12(31), 25-34. doi: 10.22034/anm.2022.2571

Vol. 15, No. 45, Winter 2026, pages 51-62

Journal of Analytical and Numerical Methods in Mining Engineering

Journal home page: http://anm.yazd.ac.ir/

Research article

Application of Fractal modeling for mapping Hydrothermal Alteration Zones Using ASTER imagery in the southeastern part of IRAN

Mohammad Hossein Aghlan[1], Mohammad Hadi Hadigheh[2], Saeed Khojastehfar[1], Hojjatollah Ranjbar[3]*

1- **School Of Mining Engineering, College Of Engineering, University Of Tehran, Tehran, Iran**
2- **Kushamadan Consulting, Tehran, Iran**
3- **Dept. of Mining Engineering, Shahid Bahonar University of Kerman, Kerman, Iran**

*Corresponding author: E-mail: *h.ranjbar@uk.ac.ir*
(Received: *June 2025*, Accepted: *September 2025)*

DOI: 10.22034/ANM.2025.23223.1683

Keywords

Fractal modeling
Anomaly detection
Remote sensing
Hydrothermal alteration
ASTER imagery
Argillic zone
Jebal Barez

Abstract

This study presents an integrated approach to map hydrothermal argillic alteration zones using ASTER satellite imagery in the Jebal Barez region of southeastern Iran. The novelty of this research lies in the combination of Spectral Angle Mapper (SAM), Matched Filtering (MF), and fractal value–area modeling for anomaly detection and classification. After atmospheric correction using the IARR method, kaolinite spectral signatures were extracted and used in the SAM and MF techniques to delineate altered zones. A total of 34 ground control points were collected across representative lithologies to validate remote sensing outputs. SAM and MF both identified key alteration zones, with MF demonstrating higher classification accuracy (82.35%) compared to SAM (73.52%). The fractal model enabled effective separation of anomalous zones by detecting scale-invariant spatial patterns and extracting critical breakpoints. The integration of fractal modeling with spectral analysis provided improved anomaly delineation and exploration targeting. Field validation confirmed the presence of Pb–Zn mineralization and silica-rich alteration in high-response zones. This methodology offers a replicable framework for mineral exploration in complex terrains using freely available remote sensing data. A detailed workflow chart is also proposed to enhance clarity and reproducibility.

1. INTRODUCTION

The concept of fractals, introduced by Mandelbrot in the 1980s, describes self-similar patterns that remain consistent across different scales. Fractal geometry enables the analysis of complex natural shapes beyond the scope of classical Euclidean geometry [1]. Building on this, multifractals describe systems governed by a multifractal spectrum [2–6] and are widely applied to scale-invariant phenomena [7].

Numerous geological processes—such as mineralization, sedimentation, volcanism, and landform evolution—exhibit self-similarity and are well-modeled using fractal and multifractal approaches [6, 8–9], making fractal analysis a valuable tool in geoscience [10–11]. In mineral exploration, fractal-based techniques (e.g., box-counting, number-size, radial density, concentration–area (C–A), concentration–distance (C–D), and local singularity models) help delineate geochemical and geophysical anomalies while preserving key spatial and statistical properties [12–21].

In remote sensing, spectral classifiers such as the Spectral Angle Mapper (SAM) are widely used

to identify alteration minerals associated with mineralization by comparing pixel spectra to known reference spectra [22–24]. Similarly, the Matched Filter (MF) method enhances mineral mapping by maximizing the signal-to-noise ratio with respect to specific spectral endmembers [25–26].

This study focuses on the identification and delineation of hydrothermal alteration zones in a part of southeastern Iran, specifically within the Jebal Barez region. ASTER satellite imagery was utilized in combination with two widely recognized spectral analysis methods: the Spectral Angle Mapper (SAM) and Matched Filter (MF). These techniques were applied to detect argillic alteration zones indicative of potential mineralization. To enhance the interpretation and spatial characterization of alteration intensity, the results were further analyzed using the value–area fractal model, which enables quantitative classification and prioritization of alteration zones for mineral exploration purposes. Despite the proven utility of spectral methods in alteration mapping, the integration of fractal models for enhancing spatial analysis and anomaly detection remains underexplored, particularly in the Jebal Barez region. This study aims to fill this gap by applying a value–area fractal approach to quantify alteration intensity derived from ASTER-based spectral classification, thereby improving mineral target delineation. The main objective is to integrate SAM and MF outputs with fractal modeling to enhance spatial analysis of alteration zones and validate results through field sampling and petrographic studies.

2. STUDY AREA

The study area is located in southern Kerman Province, Iran, approximately 45 km northeast of the city of Jiroft, between 57°58′36″–58°04′07″ E and 28°44′32″–28°49′09″ N (Fig. 1). It lies within the southeastern segment of the Urmia–Dokhtar magmatic arc, a subduction-related belt formed by the convergence of the Arabian and Iranian plates. This magmatic arc, comparable to Andean-type systems, is composed of extensive volcanic and intrusive rocks [27–30].

The regional geology includes two primary lithological units:

- The Ert unit, consisting of volcanic and pyroclastic rocks such as rhyolitic pyroclasts, basaltic andesites, and agglomerates, is predominantly observed in the northern part of the study area.
- The Gd unit comprises granitic to quartz dioritic intrusive rocks that have intruded into Eocene formations across the northern and southern regions.

Additionally, dyke-like intrusions (unit d), ranging from diorite to quartz diorite in composition, crosscut the older units and are typically concentrated around major intrusive bodies (Fig. 2).

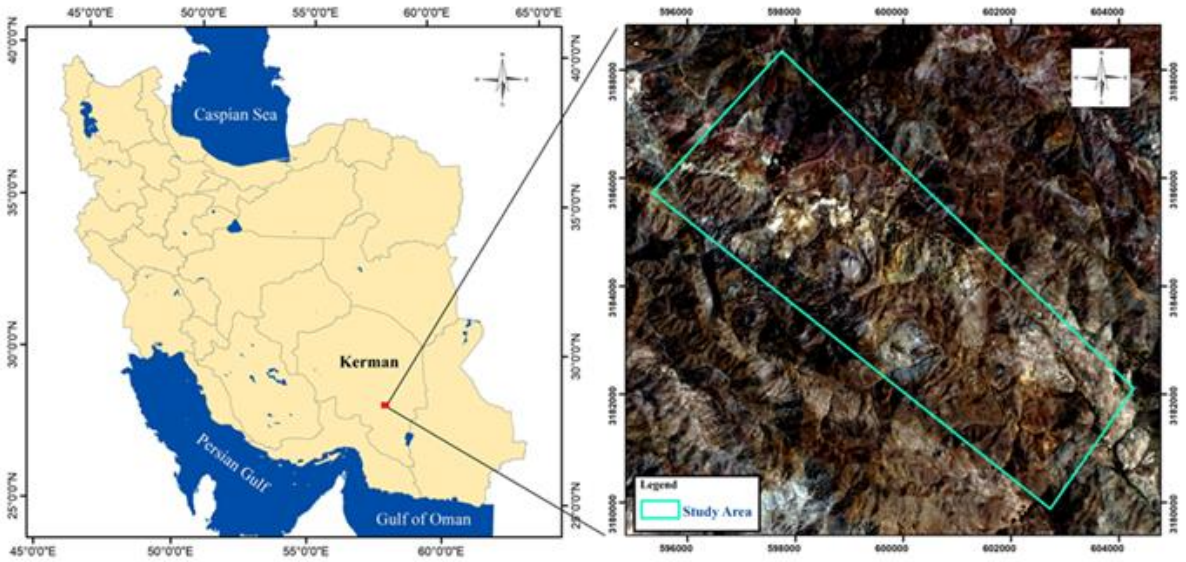

Fig.1. Geographical location and access routes of the study area.

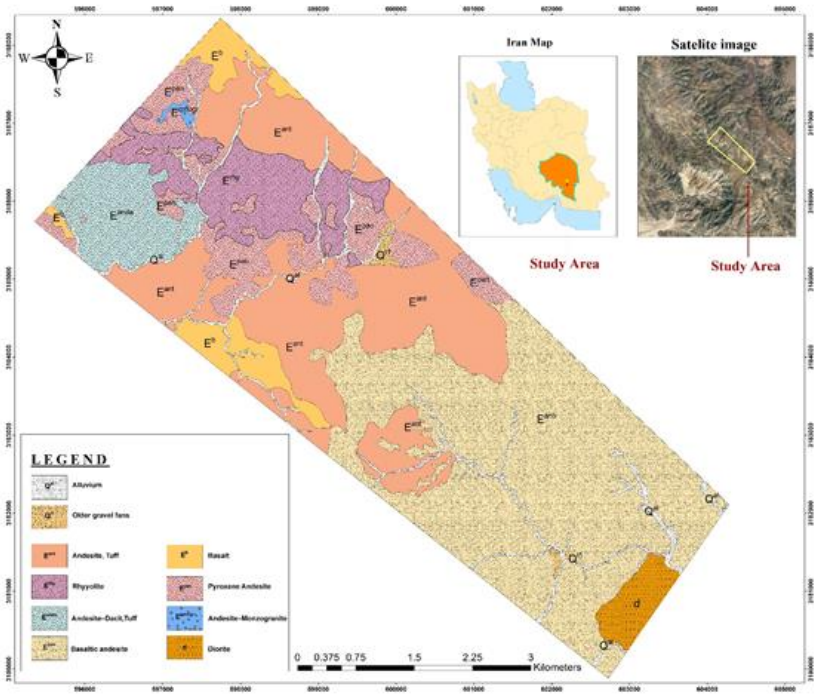

Fig. 2. The case study is located in the southeast of Urmia-Dokhtar volcanic belt and the Kerman copper.

From an economic perspective, the region hosts lead–zinc mineralized veins rich in chalcopyrite, sphalerite, and galena. These veins occur primarily within andesitic and pyroclastic rocks and are structurally controlled, often associated with iron oxide mineralization—indicative of hydrothermal processes and a favorable environment for mineral exploration.

3. DATA AND METHODS

The Advanced Spaceborne Thermal Emission and Reflection Radiometer (ASTER) is a multispectral imaging sensor widely utilized in geological applications. It provides 14 spectral bands across three subsystems: VNIR (3 bands, 15 m), SWIR (6 bands, 30 m), and TIR (5 bands, 90 m). This study employed Level 1T (L1T) ASTER imagery (scene AST_L1T_00306172007065639, acquired on June 17, 2007), pre-processed with radiometric, geometric, and topographic corrections. Atmospheric correction was applied using the Internal Average Relative Reflectance (IARR) method.

Additionally, ASTER is equipped with a backward-looking VNIR telescope that provides 15 m stereo imagery [31]. This study utilized Level 1T (L1T) ASTER imagery, which includes radiometric, geometric, and terrain corrections. The specific scene analyzed was AST_L1T_00306172007065639, acquired on June 17, 2007.

Radiometric correction was conducted using the IARR (Internal Average Relative Reflectance) method within ENVI software. This technique normalizes image spectra by internal averaging, minimizing the impact of atmospheric and topographic effects — especially important in arid, high-relief regions like southeastern Iran.

To investigate the spectral characteristics of alteration minerals, field samples were collected and analyzed. The spectral signatures of kaolinite—an indicator of argillic alteration—were extracted for use in the Spectral Angle Mapper (SAM) and Matched Filtering (MF) techniques. Following alteration mapping, a fractal-based analysis was applied to separate anomalous zones from the geologic background. Ground validation was performed through field observations and sample analysis to assess the accuracy of classification results for both SAM and MF. Atmospheric correction was conducted prior to processing using the Internal Average Relative Reflectance (IARR) method.

3.1. Spectral Characteristics Of Argillic Alteration

Kaolinite, a principal indicator of argillic alteration, exhibits distinct absorption features in the SWIR region. These include a strong absorption band near 2.2 μm and a weaker one at 2.15 μm, both associated with Al-OH vibrations. A notable absorption around 1.4 μm is also linked to OH-stretching modes [32] (Fig. 3).

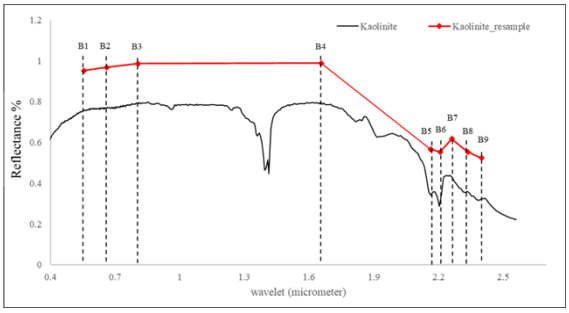

Fig. 3. Spectral profile of kaolinite (0.4–2.5 µm) with resampled bands corresponding to ASTER sensor wavelengths (adapted from USGS spectral library).

3.2. Alteration Mapping Using Spectral Angle Mapper (SAM)

The Spectral Angle Mapper (SAM) is a widely adopted technique in remote sensing for mineral exploration [33–34]. It quantifies spectral similarity by calculating the angle between a target pixel's spectrum and a reference spectrum in n-dimensional space. Both spectra are treated as vectors, and their angular relationship is measured using the following formula:

$$\cos a = \frac{\sum_{i=1}^{nb} t_i . r_i}{\sum_{i=1}^{nb} t_i^2 . \sum_{i=1}^{nb} r_i^2} \quad (1)$$

where t_i and r_i are the reflectance values of the target and reference spectra in band *i*. SAM produces two outputs: a rule image showing the spectral angle for each pixel (lower angles = better match), and a classification image based on user-defined thresholds.

3.3. Alteration Mapping Using Matched Filtering (MF)

The Matched Filtering (MF) method is used to estimate the presence of specific target endmembers in mixed pixels [35]. It enhances the spectral response of the target while suppressing background noise, effectively maximizing the signal-to-noise ratio.

MF generates fraction images for each target endmember, with grayscale pixel values ranging from 0 to 1—where 1 represents a perfect spectral match, and 0 indicates no similarity [36-37].

3.4. Rationale For Method Selection And Modeling Strategy

SAM and MF were selected due to their proven effectiveness in identifying hydroxyl-bearing alteration minerals such as kaolinite and alunite[38-39]. SAM measures spectral similarity by calculating the angle between image and reference spectra, while MF enhances the target spectral response by suppressing background interference.

In this study, kaolinite spectra from the USGS spectral library were resampled to match ASTER bands and used as reference. For SAM, classification thresholds were empirically set at 0.1 radians after trial runs to minimize false positives. MF outputs were thresholded using statistical cutoffs derived from histogram analysis of fraction images (mean + 1.5σ).

Following spectral classification, the fractal value–area model was applied to quantify the spatial distribution of alteration intensities. This model plots the cumulative area above a given pixel value versus the pixel value itself on a log–log scale, revealing linear segments that correspond to distinct geospatial regimes. Breakpoints in these plots were determined visually and statistically using slope-change detection, and used to classify pixels into background, weak, and strong anomalies.

The MF and SAM grayscale outputs served as input images for fractal modeling, enabling a hierarchical classification based on spatial complexity. This integration improved the identification of discrete alteration zones and supported prioritization of field validation targets.

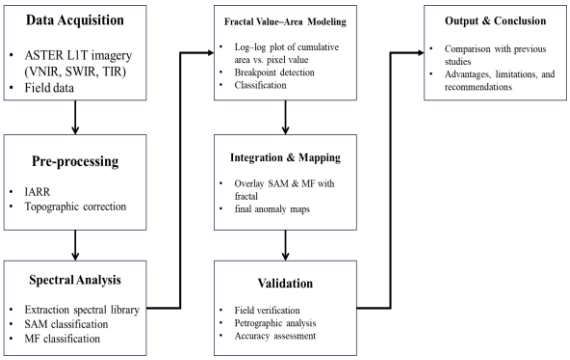

Fig. 4. Workflow of the research methodology applied in this study.

4. RESULTS AND DISCUSSION

To assess the performance of the SAM and MF techniques, spectral match outputs were thresholded based on histogram analyses. For SAM, an angular threshold of 0.1 radians was applied to highlight areas of strong spectral similarity with kaolinite. For MF, pixel values above 0.45 (mean + 1.5σ) were considered indicative of probable alteration. Visual comparison between Figures 5a and 5b reveals broader coverage by SAM, identifying generalized alteration halos, whereas MF shows higher spatial contrast and more localized high-intensity zones. This difference reflects SAM's sensitivity to broad spectral features and MF's ability to suppress background noise and highlight pure endmembers. The SAM and MF techniques were

implemented using reference spectra from the United States Geological Survey (USGS) spectral library. Both methods successfully identified hydrothermal alteration zones, which were subsequently verified through field observations.

Significant argillic alteration was concentrated in the southern and southeastern sectors of the Jebal Barez region. These zones were characterized by intense clay alteration and the presence of iron oxides, as illustrated in Figures 5 and 6.

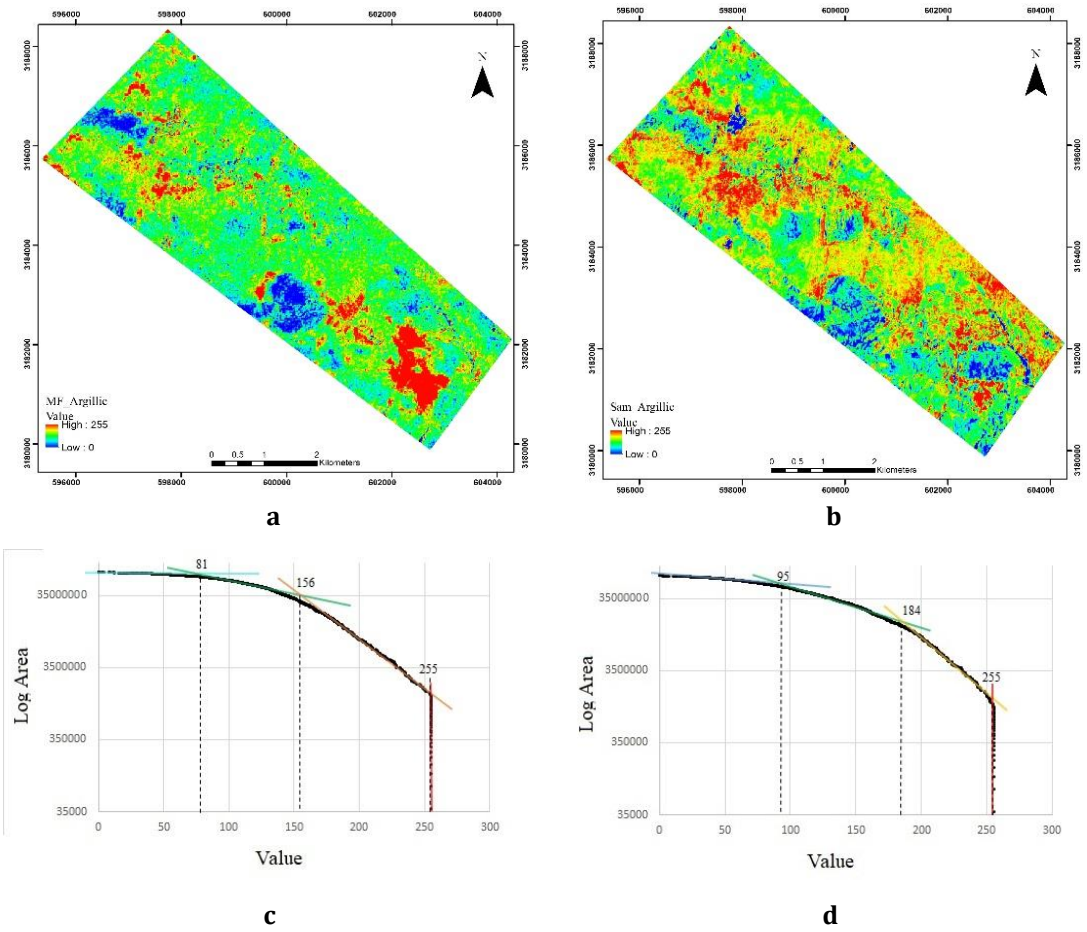

Fig. 5. (a) Argillic alteration zones derived from Matched Filtering (MF). (b) Argillic alteration zones mapped using the Spectral Angle Mapper (SAM). (c) Value–area fractal plots for MF and (d) SAM outputs.

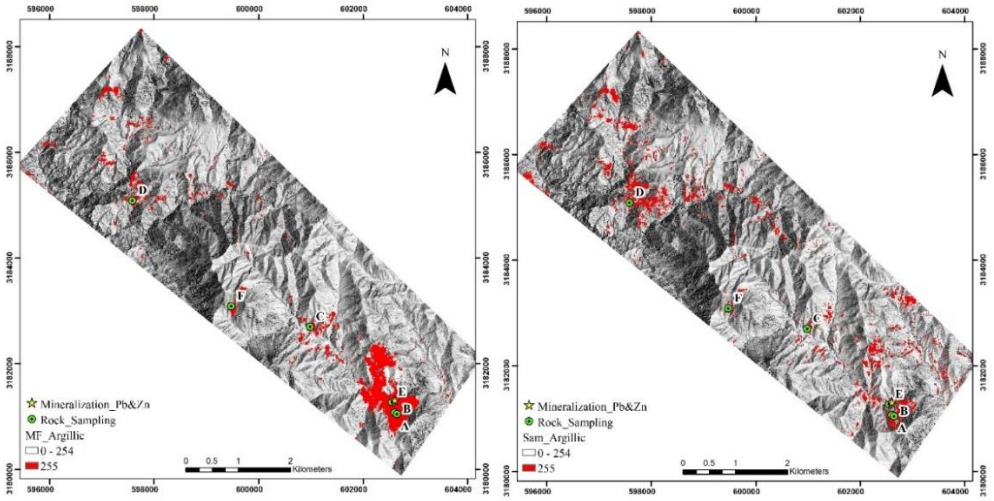

Fig. 6. Detailed field photographs and petrographic views of six representative ground control points (GCPs) selected from the total set of 34 samples. These samples were chosen to reflect a variety of lithologies and alteration intensities. Overlay of alteration zones (value = 255) from (a) MF and (b) SAM techniques with field data including sampling sites and Pb–Zn mineral occurrences.

Field investigations confirmed that mineralization in these altered zones primarily occurs as siliceous veins enriched in lead and zinc, with galena and sphalerite identified as the main ore minerals. As shown in Figures 5a and 5b, both MF and SAM successfully delineated argillic alteration zones, with the MF technique offering more localized and high-contrast outputs. The fractal value–area plots in Figure 5c confirm the presence of scale-invariant patterns within the mapped data. Identified breakpoints at values 81 and 156 (MF), and 95 and 184 (SAM), effectively separate background from anomalous regions. Figure 6 demonstrates strong spatial agreement between high-response alteration zones (red pixels) and field-verified Pb–Zn mineralization sites, particularly in the southern sector. Sampling points coincide with MF and SAM anomalies, validating the spectral results.

Fractal value–area plots were generated by ranking pixel values and plotting cumulative area versus value on a log–log scale. Breakpoints were identified visually and numerically as inflection points where slope changes occur, indicating transitions between background and anomaly regimes.

For MF (Figure 5c), breakpoints at pixel values 81 and 156 effectively delineated low-, medium-, and high-intensity alteration. Similarly, SAM-derived values at 95 and 184 (Figure 5d) reflect consistent spatial trends. These thresholds were subsequently used to reclassify output maps for interpretation.

The findings are consistent with previous studies in Iran and other regions with similar geological settings. For instance, Tangestani et al. (2008) reported effective alteration mapping using ASTER in the Shahr-e-Babak region, but without employing fractal analysis. Similarly, Afzal et al. (2011) applied C–A fractal models for porphyry Cu systems but relied on geochemical data. Our integration of SAM/MF with value–area fractal modeling represents a novel contribution by enabling anomaly separation directly from remote sensing outputs, offering both spatial precision and scalability.

Compared with previous ASTER-based alteration mapping in SE Iran (e.g., Tangestani et al., 2008) and fractal applications primarily in geochemical domains (e.g., Afzal et al., 2011), our approach integrates fractal value–area analysis directly with SAM/MF outputs. This yields objective, reproducible thresholds for anomaly separation and improves target prioritization without requiring additional ancillary datasets.

Petrographic observations (sericitic/argillic overprint, iron-oxide veining, silica enrichment) are consistent with SWIR absorption features detected for kaolinite-bearing alteration, supporting both SAM halos and MF high-contrast centers. The spatial coincidence between mapped high-value pixels and hand-specimen/mineralogical evidence strengthens the interpretation of argillic alteration zones as validated targets

5. ACCURACY ASSESSMENT

In this study, a total of 34 ground control points (GCPs) were collected across different lithologies and alteration zones for validation. Six representative samples (Fig. 6) were selected for detailed petrographic and spectral examination because they cover the range of alteration intensities and lithological contexts observed in the field. The locations of all 34 GCPs are shown in Figure 7. This approach allows in-depth discussion of typical alteration patterns while ensuring that the accuracy assessment incorporates the full validation set.

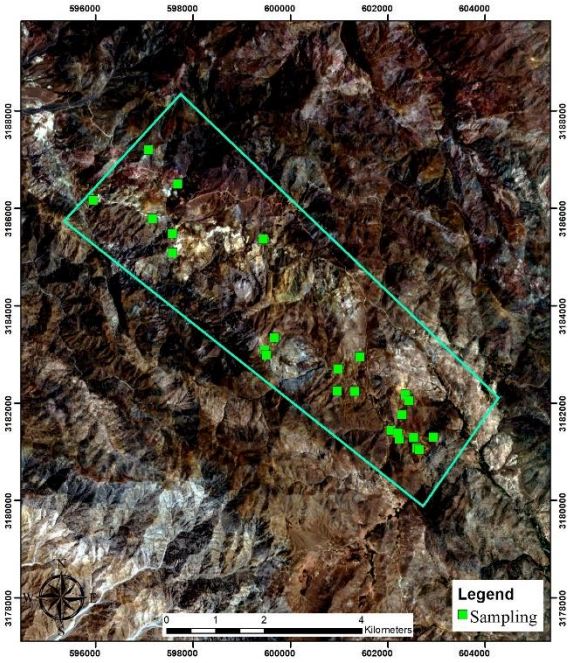

Fig. 7. Spatial distribution of ground control sampling points within the study area.

To validate the remote sensing results, a field survey was conducted to verify zones of argillic alteration, iron oxide staining, and kaolinite occurrences visually identified in ASTER imagery. Ground-truth observations were used to assess the performance of the SAM and MF classification methods by comparing pixel-based predictions with field data (Figures 8 and 9). The Matched Filtering (MF) method achieved an overall classification accuracy of 82.35%, while the Spectral Angle Mapper (SAM) achieved 73.52%

accuracy, as presented in Table 1. The classification accuracy was assessed by comparing remote sensing outputs (SAM and MF) to field-verified control points. Confusion matrices were constructed, and overall accuracy was calculated. The MF method yielded 82.35% accuracy (28/34 correct predictions), while SAM achieved 73.52% (25/34). These results indicate higher spatial precision for MF in mapping argillic alteration. The observed misclassifications were primarily in transitional zones, suggesting potential spectral mixing or sub-pixel heterogeneity. Further field validation involved petrographic analysis of representative rock samples collected from selected alteration zones. Two key samples are described below:

To further validate the alteration zones identified through remote sensing, selected rock samples were prepared as thin sections and analyzed under a polarizing microscope. Two representative samples are described below, highlighting key mineralogical features and hydrothermal alteration signatures. Figure 8 highlights a significant variation in the spatial distribution of alteration zones derived from SAM and MF. MF (Fig. 8a) isolates more compact and high-contrast alteration centers, while SAM (Fig. 8b) maps broader and less distinct halos. These differences emphasize MF's higher specificity and SAM's broader sensitivity. This complementarity suggests the potential benefit of integrating both outputs in a hybrid decision-support system for exploration.

Petrographic analysis confirmed the presence of alteration minerals such as sericite, epidote, and kaolinite in samples collected from mapped anomalous zones. These minerals correspond with absorption features detected in the SWIR bands of ASTER, validating the spectral approach. The spatial overlap between altered outcrops and high-value pixels in MF and SAM maps supports the robustness of the classification framework. Some limitations affect the accuracy assessment. First, field sampling was constrained by terrain accessibility, potentially biasing spatial coverage. Second, spectral confusion due to overlapping mineral features may result in classification errors. Third, weathering effects and vegetation may obscure alteration signatures in some zones. These factors should be considered when extrapolating results to broader regions.

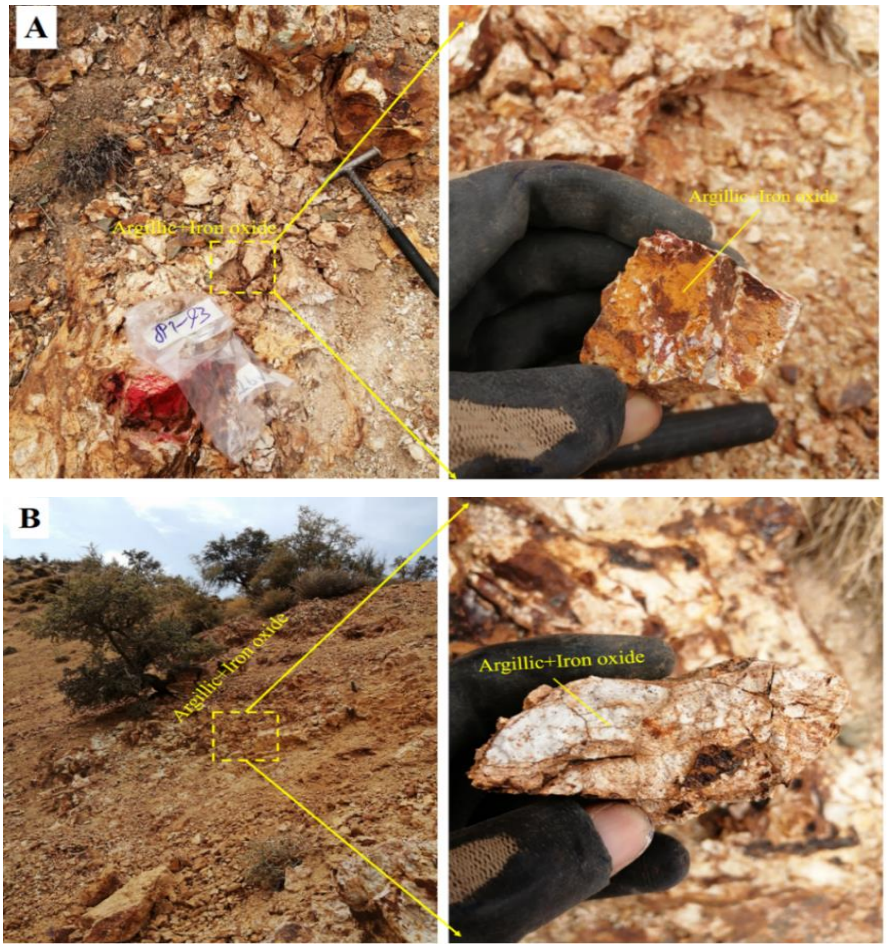

Fig. 8. (A, B) Outcrops of argillic alteration observed in dioritic and granodioritic rocks in the southeastern part of the study area.

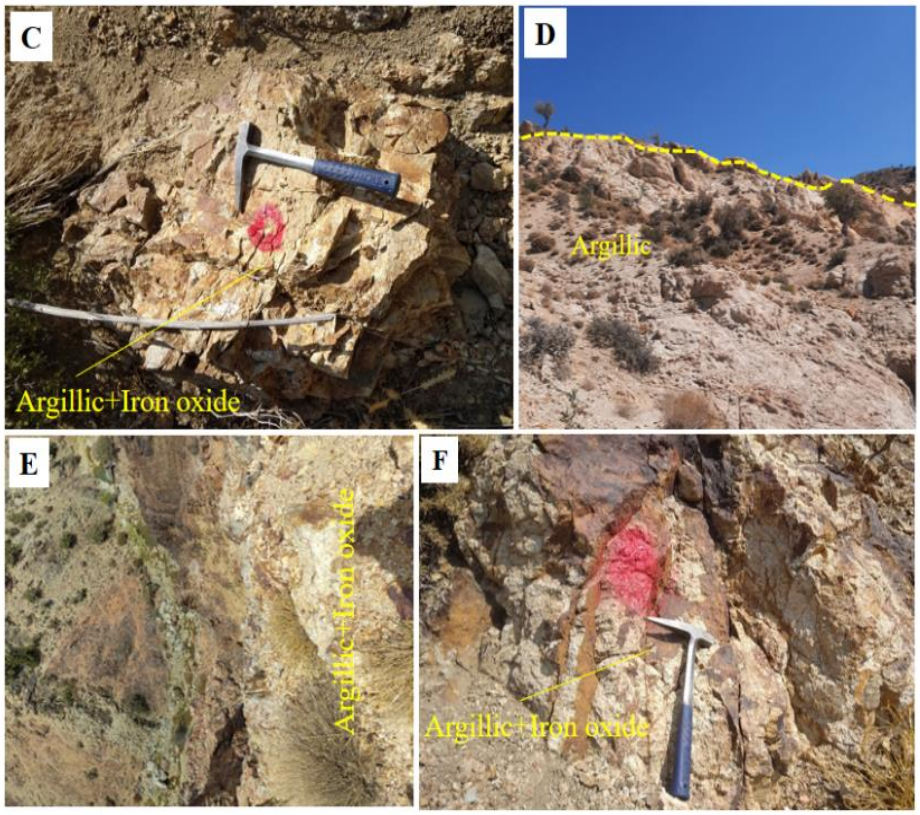

Fig. 9. (C, D) Iron oxide vein networks formed within argillic alteration units, with vein thicknesses ranging from 1 to 10 cm. (E) Iron oxide outcrop in andesitic rocks located in the northern to central parts of the study area. (F) Argillic alteration outcrop observed in diorite, located in the central sector.

Fig. 10. Silica-rich veins with visible galena and Pb–Zn mineralization in the northern part of the study area, providing ground evidence in support of remote sensing results.

Table 1. The overall accuracy for SAM and MF methods in detecting hydrothermal alterations

Method MF		Method SAM	
Predict	class	Predict	class
Other	6	Other	9
Argillic	28	Argillic	25
total	34	total	34
Accuracy Assessment%	82.35	Accuracy Assessment%	73.52

To further validate the alteration zones identified through remote sensing, selected rock samples were prepared as thin sections and analyzed under a polarizing microscope. Two representative samples are described below, highlighting key mineralogical features and hydrothermal alteration signatures.

5.1. Sample 1: Altered And Silicified Quartz-Monzogranite

This sample exhibits a poikilitic texture and intense hydrothermal alteration. The mineral assemblage includes sericitic, argillic, epidotic, and phyllic alteration types, indicative of prolonged fluid-rock interaction. Major mineral components include quartz, alkali feldspar, and plagioclase.

Plagioclase (~35%): Euhedral to subhedral tabular crystals (0.5–1.5 mm), extensively altered to sericite, clay minerals, epidote, and other phyllosilicates.

Quartz (~15%): Subhedral grains approximately 1 mm in size.

Alkali feldspar (~25%): Strongly altered to sericite and clay; crystal size ranges from 0.3 mm to >1 mm.

Pyroxene (<10%): Occurs as scattered subhedral grains (<1 mm), often associated with iron oxide

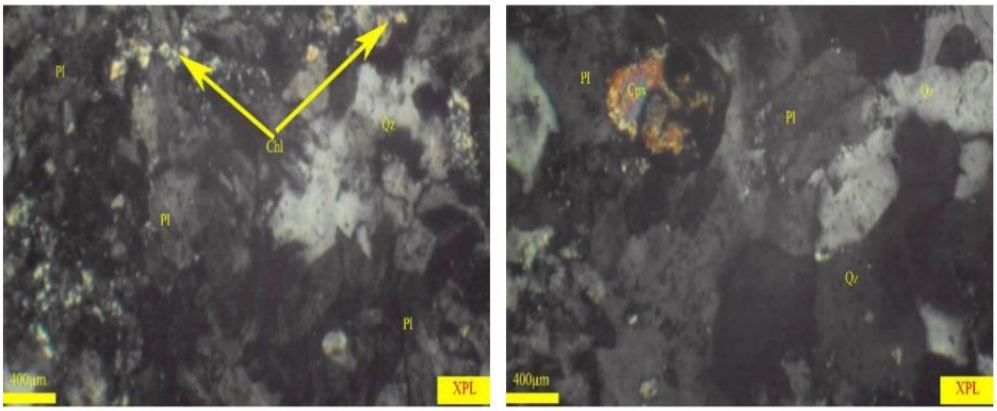

Fig. 11. Photomicrograph of Sample 1 showing altered plagioclase (sericitic and argillic), subhedral quartz, and pyroxene grains with evidence of iron oxide overprint.

5.2. Sample 2: Altered Volcanic Rock

This sample is interpreted as an altered intrusive volcanic unit with porphyritic to massive texture. The rock has undergone significant hydrothermal overprinting, characterized by sericitic, argillic, and local epidotic alteration.

Plagioclase: The dominant phase, appearing as subhedral crystals (>1 mm), moderately to intensely altered by sericite and clay minerals.

Epidote: Present in localized zones, suggesting multiphase fluid evolution.

Quartz and alkali feldspar (~35%): Subhedral grains ranging from 0.3 mm to >1 mm.

Siliceous veining: Composed of subhedral quartz, cross-cutting the matrix and indicative of late-stage silica mobilization.

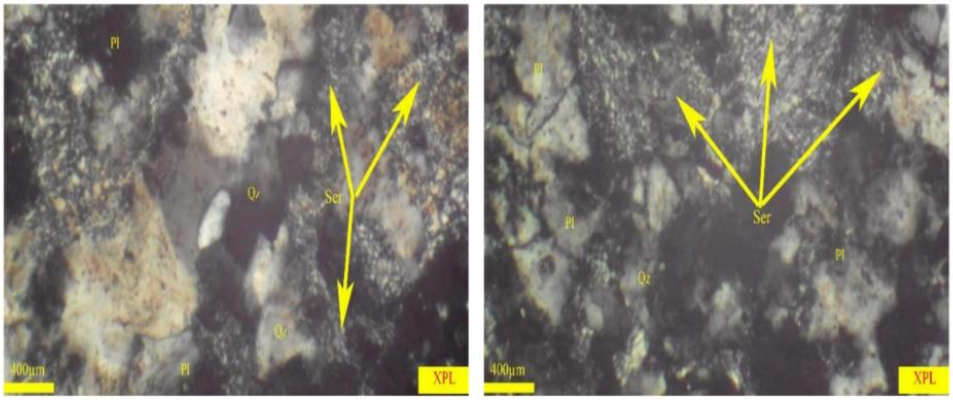

Fig. 12. Photomicrograph of Sample 2 showing altered plagioclase (sericitic and argillic), semi-formed quartz crystals, and quartz-rich veinlets.

6. SUMMARY AND CONCLUSIONS

This study successfully delineated hydrothermal argillic alteration zones in the Jebal Barez region through an integrated approach combining ASTER satellite imagery, spectral classification (SAM and MF), and fractal value–area modeling.

SAM and MF both identified key altered zones, with MF achieving a higher accuracy (82.35%) in pixel-level classification compared to SAM (73.52%). Fractal modeling revealed scale-invariant spatial patterns and allowed threshold-based classification of anomalies, improving the interpretation of alteration intensity.

Field validation, including petrographic analysis of representative samples, confirmed the presence of kaolinite, iron oxides, and Pb–Zn mineralization in high-response areas. The strong spatial correlation between mapped anomalies and ground evidence underscores the effectiveness of the integrated methodology.

While SAM offered broader coverage of alteration halos, MF provided greater sensitivity to pure mineral signatures. Their combined use enhances both detection and spatial refinement of anomalies. Despite the promising results, certain limitations remain. ASTER's moderate spatial resolution may limit the detection of small or narrow alteration features. The fractal model relies on empirical breakpoint selection, which may introduce subjectivity. Future research should explore integration with hyperspectral data and machine learning-based anomaly detection to enhance predictive performance and reduce uncertainty.

Acknowledgment

The authors would like to express their sincere gratitude to the Geological Survey Organization for providing essential datasets that supported the execution of this research. Appreciation is also extended to Kusha Madan Consulting Engineers for their logistical support and for making additional data and resources available throughout the course of the study.

REFERENCES

[1] Davis, J. C. (2002). Statistics and data analysis in Geology (3rd ed.) (pp. 342–353). New York: Wiley.

[2] Feder, J. (1988). Fractals New York: Plenum.

[3] Stanley, H., & Meakin, P. (1988). Multifractal phenomena in physics and chemistry. Nature, 335(6189), 405–409.

[4] Evertz, C. J. G., & Mandelbrot, B. B. (1992). Multifractal measures. Appendix B. In H.-O. Peitgen, H. Jurgens, & D. Saupe (Eds.), Chaos and fractals (pp. 922–953). New York: Springer.

[5] Agterberg, F. P., Cheng, Q., & Wright, D. F. (1993). Fractal modelling of mineral deposits. J. Elbrond & X. Tang (Eds.), Application of computers and operations research in the mineral industry (pp. 43–53), Proceedings of the 24th APCOM Symposium. Montreal: Canadian Institute of Mining Metalling and Petroleum.

[6] Cheng, Q. (1994). Multifractal modeling and spatial analysis with GIS: Gold potential estimation in the Mitchell-Sulphurets area, northwestern British Columbia. Unpublished Doctoral Dissertation, School of Graduate Studies and Research, University of Ottawa.

[7] Mandelbrot, B. B. (1974). Intermittent turbulence in self-similar cascades: Divergence of high moments and dimension of the carrier. Journal of Fluid Mechanics, 62(2), 331–358.

[8] Cheng, Q., Bonham-Carter, G. F., Hall, G. E. M., & Bajc, A. (1997). Statistical study of trace elements in the soluble organic and amorphous Fe–Mn phases of surficial sediments, Sudbury Basin, 1, Multivariate and spatial analysis. Journal of Geochemical Exploration, 59(1), 27–46.

[9] Cheng, Q. (1999b). Multifractality and spatial statistics. Computers & Geosciences, 25(9), 949–961.

[10] Panahi, A., Cheng, Q., & Bonham-Carter, G. F. (2004). Modeling lake sediment geochemical distribution using principal component, indicator kriging and multifractal power-spectrum analysis: a case study from Gowganda, Ontario. Geochemistry: Exploration, Environment, Analysis, 4(1), 59–70.

[11] Zuo, R., & Xia, Q. (2009). Application fractal and multifractal methods to mapping prospectivity for metamorphosed sedimentary iron deposits using stream sediment geochemical data in eastern Hebei province, China. Geochimica et Cosmochimica Acta, 73, A1540.

[12] Deng, J., Fang, Y., Yang, L. Q., Yang, J. C., Sun, Z. S., Wang, J. P., et al. (2001). Numerical modelling of ore-forming dynamics of fractal dispersive fluid systems. Acta Geologica Sinica, 75(2), 220–232.

[13] Deng, J., Wang, Q. F., Huang, D. H., Wan, L., Yang, L. Q., & Gao, B. F. (2006). Transport network and flow mechanism of shallow ore-bearing magma in Tongling ore cluster area. Science in China (Series D), 49(4), 397–407.

[14] Mandelbrot, B. B. (1983). The fractal geometry of nature (updated and augmented). New York: Freeman.

[15] Turcotte, D. L. (2002). Fractals in petrology. Lithos, 65(3–4), 261–271.

[16] Wang, Q. F., Deng, J., Liu, H., Yang, L. Q., Wan, L., & Zhang, R. Z. (2010). Fractal models for ore reserve estimation. Ore Geology Reviews, 37(1), 2–14.

[17] Raines, G. L. (2008). Are fractal dimensions of the spatial distribution of mineral deposits meaningful? Natural Resources Research, 17, 87–97.

[18] Carranza, E. J. M., Owusu, E., & Hale, M. (2009). Mapping of prospectivity and estimation of number of undiscovered prospects for lode-gold, southwestern Ashanti Belt, Ghana. Mineralium Deposita, 44(8), 915–938.

[19] Li, C. J., Ma, T. H., & Shi, J. F. (2003). Application of a fractal method relating concentration and distances for separation of geochemical anomalies from background. Journal of Geochemical Exploration, 77(2), 167–175.

[20] Cheng, Q., Agterberg, F. P., & Ballantyne, S. B. (1994). The separation of geochemical anomalies from background by fractal methods. Journal of Geochemical Exploration, 51(2), 109–130.

[21] Afzal, P., Alghalandis, Y. F., Khakzad, A., Moarefvand, P., & Omran, N. R. (2011). Delineation of mineralization zones in porphyry Cu deposits by fractal concentration–volume modeling. Journal of Geochemical Exploration, 108(3), 220–232.

[22] Ahmadi, H. and Uygucgil, H. (2021) Targeting Iron Prospective within the Kabul Block (SE Afghanistan) via Hydrothermal Alteration Mapping Using Remote Sensing Techniques. Arabian Journal of Geosciences, 14, Article No. 183.

[23] Hdeid, O. M., Morsli, Y., Raji, M., Baroudi, Z., Adjour, M., Nebagha, K. C, & Vall, I. B. (2024). Application of Remote Sensing and GIS in Mineral Alteration Mapping and Lineament Extraction Case of Oudiane Elkharoub (Requibat Shield, Northern of Mauritania). Open Journal of Geology, 14(9), 823-854.

[24] Chen, L., Sui, X., Liu, R., Chen, H., Li, Y., Zhang, X., & Chen, H. (2023). Mapping alteration minerals using ZY-1 02D hyperspectral remote sensing data in coalbed methane enrichment areas. Remote Sensing, 15(14), 3590.

[25] Wu, C., Dai, J., Zhou, A., He, L., Tian, B., Lin, W. & Bai, L. (2023). Mapping alteration zones in the Southern section of Yulong copper belt, Tibet using multi-source remote sensing data. Frontiers in Earth Science, 11, 1164131.

[26] Khademian, F., Alaminia, Z., Nadimi, A., Lentz, D. R., Ghasemi, A., & Sharifi, M. (2024). Structural and alteration zones controls on Cu mineralisation in the northwest of Nain (northeastern Isfahan, Iran): A remote sensing perspective. Journal of African Earth Sciences, 211, 105151.

[27] Alavi, M. (1980). Tectonostratigraphic evolution of the Zagrosides of Iran. Geology, 8(3), 144-149.

[28] Alavi, M. (1994). Tectonics of the Zagros orogenic belt of Iran: new data and interpretations. Tectonophysics, 229(3-4), 211-238.

[29] Berberian, M., & King, G. C. P. (1981). Towards a paleogeography and tectonic evolution of Iran. Canadian journal of earth sciences, 18(2), 210-265.

[30] Berberian, F., Muir, I. D., Pankhurst, R. J., & Berberian, M. (1982). Late Cretaceous and early Miocene Andean-type plutonic activity in northern Makran and Central Iran. Journal of the Geological Society, 139(5), 605-614.

[31] Rowan, L. C., Hook, S. J., Abrams, M. J., & Mars, J. C. (2003). Mapping hydrothermally altered rocks at Cuprite, Nevada, using the Advanced Spaceborne Thermal Emission and Reflection Radiometer (ASTER), a new satellite-imaging system. Economic Geology, 98(5), 1019-1027.

[32] Clark, R. N., King, T. V., Klejwa, M., Swayze, G. A., & Vergo, N. (1990). High spectral resolution reflectance spectroscopy of minerals. Journal of Geophysical Research: Solid Earth, 95(B8), 12653-12680.

[33] Kruse FA, Lefkoff AB, Boardman JB, Heidebrecht KB, Shapiro AT, Barloon PJ, Goetz A.F.H (1993)The Spectral Image Processing System (SIPS) – interactive visualization and analysis of imagingspectrometer data, Remote Sensing of Environment 44: 145–163.

[34] Tangestani MH, Mazhari N, Agar B, Moore F (2008) Evaluating Advanced Spaceborne Thermal Emission and Reflection Radiometer (ASTER) data for alteration zone enhancement in a semi-arid area, northern Shahr–e–Babak, SE Iran, International Journal of Remote Sensing 29: 2833–2850.

[35] Habashi, J., Moghadam, H. J., Oskouei, M. M., Pour, A. B., & Hashim, M. (2024). PRISMA hyperspectral remote sensing data for mapping alteration minerals in sar-e-châh-e-shur region, birjand, Iran. Remote Sensing, 16(7), 1277.

[36] Rossi, C., & Gholizadeh, H. (2023). Uncovering the hidden: Leveraging sub-pixel spectral diversity to estimate plant diversity from space. Remote Sensing of Environment, 296, 113734.

[37] Khojastehfar, S. , Ranjbar, H. and Shafiei Bafti, S. (2023). Sub-pixel Mineral Mapping of Serpentine and Magnesite for Chromite Exploration, Using Hyperion (EO1) Images. *Journal of Analytical and Numerical Methods in Mining Engineering*, *13*(35), 39-49. doi: 10.22034/anm.2023.18911.1565

[38] Ilyati, I. , Amanian, N. , Ansari, A. and Mokhtari, M. H. (2020). Combination of Remote Sensing and Ground Penetrating Radar methods to estimate suitable areas for locating subsurface dams in Abouzeidabad Plain. *Journal of Analytical and Numerical Methods in Mining Engineering*, *10*(25), 1-11. doi: 10.29252/anm.2020.13980.1443

[39] Mokhtari, Z. and Seifi, A. (2021). Detection of Hydrothermal Alteration Zones Using ASTER Remote Sensing Data in Turquoise mine of Neyshabur. *Journal of Analytical and Numerical Methods in Mining Engineering*, *11*(28), 1-22. doi: 10.22034/anm.2021.203

Vol. 15, No. 45, Winter 2026, pages 63-74

Journal of Analytical and Numerical Methods in Mining Engineering

Journal home page: http://anm.yazd.ac.ir/

Research article

Investigating the effects of loading rate and mixing design on concrete's direct tensile strength using the CTLC test

Manouchehr Sanei[1]*, Mohammad Fatehi Marji[1], Dinmohammad Yusufi[1], Mohammad Davood Yavari[2]

1- **Dept. of Mining and Metallurgy Engineering, Yazd University, Yazd, Iran**
2- **Dept. of Mining Engineering, Faculty of Engineering, Kashan University, Kashan, Iran**

*Corresponding author: E-mail: *m.sanei@yazd.ac.ir*
(Received*: January 2025*, Accepted*: May 2025)*

DOI: 10.22034/ANM.2025.22631.1657

Keywords

Concrete
Direct tensile test
Brazilian tensile test
Mixing design
Loading rate

Abstract

The tensile strength of concrete is measured using direct tensile tests on rectangular concrete samples with dimensions of 19 cm in length, 16 cm in width, and 6 cm in thickness, with a central hole of 9 cm in diameter. The concrete specimens were prepared in the laboratory by mixing cement, fine sand, gravel, and water in appropriate proportions. Calibration of the new direct tensile strength test apparatus was carried out to determine the tensile strength of different brittle materials (gypsum and concrete) under various loading rates and different mixing design types. The direct tensile strength tests were accomplished by a compressive-to-tensile load converter (CTLC) fitted with the specimens and placed in the universal testing machine in the laboratory. For the indirect Brazilian tensile strength tests, loading rates of 5, 10, and 15 kg/s were considered. For the direct tensile strength tests, loading rates of 2, 2.5, and 3 mm/min were used. The results of this paper show that the direct tensile strengths measured by the CTLC apparatus are approximately 25% lower than those measured by the Brazilian tests. The average tensile strengths of the geo-material samples increase as both the loading rate and the ratio of fine sand to gravel increase.

1. INTRODUCTION

Concrete is one of the most important materials in today's society and is widely used in many construction projects consist including foundations, dams, and tunnel stability [1-6]. The tensile strength of concrete is one of the most basic and key features that has a significant impact on the stability of structures, tunnels, and bridges. Furthermore, due to its brittle nature, concrete performs very poorly against applied stresses, so it is not expected to withstand direct stress. Therefore, when the tensile forces exceed the tensile strength of concrete, cracks are created in concrete, which eventually cause fracture [7-13]. Therefore, measuring the tensile strength of concrete as a heterogeneous material is a challenging issue. The existing methods for measuring tensile strength are grouped according to indirect and direct tensile strength. In the indirect tensile test, various methods such as the Brazilian and bending tensile tests have been presented to measure the tensile strength [14-18]. The Brazilian tensile test is performed on cylindrical specimens, and the flexural test on beam-like specimens; although these methods are widely accepted, they do not provide the true tensile strength of concrete [19-25]. In direct tensile testing, the load application mechanism must be carefully designed to reduce load eccentricity and stress concentration at the end of the specimen. It is challenging to place the

specimen and apply the load in the direct tension apparatus. Direct tensile testing is usually performed uniaxially. However, setting up a direct tensile test is time-consuming, and the results can depend on the applied boundary conditions [26-29]. Many experimental and theoretical studies have been conducted to determine the tensile strength [30], including the tensile strength of concrete using a uniaxial tensile test on rectangular samples [31]. Sarfarazi et al. have presented a new approach to determine the direct tensile strength of concrete based on the uniaxial method using a dumbbell sample [32]. Liao et al. conducted a direct tensile test using cylindrical specimens with a diameter of 101.6 mm and a height of 203.2 mm, similar to that used in the uniaxial tensile test [33]. Sarfarazi et al. have used the compressive to tensile load transformer apparatus as a modern approach to determining the direct tensile strength of concrete [34]. Fakhimi and Laboz have proposed the development of a new method for testing the tensile strength of concrete using a Strut and tie method [7]. Haeri et al. studied the direct tensile strength measurement of granite by the universal tensile testing machine [35]. Fu et al. improved the tensile strength of reinforced concrete by evaluating the impact of different fiber additives through numerical and experimental analysis [36].

Wang et al. developed the dynamic tensile strength prediction model and tensile behavior of concrete considering pores based on the impact splitting tensile test [37]. They have measured the tensile strength of concrete by using special samples, considering the compressive to tensile load converter apparatus. According to the previous research and the results expressed by the researchers, it can be claimed that additional studies are still needed to develop the apparatus to determine the tensile strength of concrete, as well as various investigations to evaluate the quality of concrete. Although there are many tensile strength devices, most of them are either limited in availability or expensive. Therefore, it is necessary to develop a new device that can measure the tensile strength of concrete.

According to the limitations stated in this field, a new method has been used to test the tensile strength of concrete using a new direct tensile test apparatus based on a compressive-to-tensile load converter. Also, the calibration of the new direct tensile test apparatus was performed by considering the effect of different loading rates and different mixing designs on two types of materials, concrete and gypsum, with two methods, the Brazilian test and direct tensile test. This newly developed apparatus is equipped with a data logger and records information such as time, load, and displacement to the computer through the cable with a serial port monitor Software. Then, using the newly developed apparatus, the effect of loading rate and different mixing designs on concrete was investigated. It is essential to mention that one of the important goals of this study is to analyze the effect of loading rate and different mixing designs by using this new apparatus. Also, comparing the results of this apparatus with the Brazilian test shows a 26% difference in tensile strength.

2. DETERMINATION OF TENSILE STRENGTH

While this study focuses on the direct tensile behavior of concrete under varying loading rates and mix designs, the broader implications of tensile strength in geomechanical systems are evident across diverse applications. Tensile resistance plays a critical role not only in wellbore stability analysis within petroleum engineering—where directional drilling and safe mud weight windows are governed by subsurface stress conditions—but also in the structural integrity of underground caverns for hydropower facilities. Moreover, the interaction between tensile capacity and dynamic fluid loads becomes particularly relevant in large-scale infrastructure such as double-arched dams, where water-structure coupling under impact conditions demands robust numerical modeling. These parallels underscore the interdisciplinary relevance of tensile strength across both surface and subsurface engineering domains [38-40]. Generally, determining tensile strength is measured by two indirect and direct methods using separate apparatus. In the following section, a brief description of the mentioned methods will be given.

2.1. Indirect Tensile Strength Measurement

Brazilian tests and bending tests are widely used as indirect approaches to measure tensile strength [1, 11]. In this section, the Brazilian test is used to determine the tensile strength of concrete. Also, the impact of loading speed and different mixing designs on the tensile strength of concrete has been considered using the Brazilian method, which will be discussed further.

2.1.1. Indirect Brazilian tensile strength test (IBTS)

In the Brazilian test to measure the tensile strength of concrete, standard cylindrical specimens with a ratio of length to diameter (0.5) are prepared and placed horizontally under the testing apparatus. As a result, applying a plane or radial force on a cylindrical specimen causes a vertical crack along the diameter of the specimen.

Then, the tensile strength of Brazil is calculated from Eq. (1).

$$\sigma_t = \frac{2p}{\pi Dt} \quad (1)$$

Where p is the vertical force, t is the thickness of the Brazilian specimen, and D is the diameter of the Brazilian specimen.

In this topic, a concrete sample prepared with a central hole has been used to perform a direct tensile test, whose central hole has a height of 6 cm and a diameter of 9 cm as a Brazilian sample under vertical loading with a load of 0.03. mm/s, considering the standard conditions applied. 6 Brazilian concrete samples were tested as standard Brazilian samples after 28 days under the loading of the testing apparatus to measure the tensile strength.

Figure 1 shows a Brazilian sample subjected to a testing apparatus to determine the tensile strength, which caused a crack along the diameter of the sample as a result of the application of a vertical force. The tensile strength of concrete in the Brazilian test was calculated using Eq. (1), the results of which are shown in Table 1.

Fig. 1. Concrete sample under Brazilian test

Table 1. Test results of concrete samples using the Brazilian tensile method

Mix design	Components	Values %	Test Method	Tensile strength (MP)
Proper mixing design with Portland cement for 28 days	water	10	Brazilian	0.89
	cement	15	Brazilian	0.93
	sand	43	Brazilian	0.82
			Brazilian	0.97
			Brazilian	0.87
	gravel	32	Brazilian	0.83
			average	0.88

Also, in Table 2, samples of Brazilian gypsum with a length to diameter ratio of 0.5 were prepared under standard conditions after 48 hours under the load of the testing machine to measure tensile strength, the results of which are reported.

Table 2. Test results of gypsum samples using the Brazilian tension method

No	Test Method	Time(hour)	Tensile strength (MP)
1	Brazilian	48	0.70
2	Brazilian	48	0.82
3	Brazilian	48	0.82
	average		0.78

Measuring tensile strength directly in the laboratory is not an easy task. The uniaxial tensile test is performed to determine the direct tensile strength of brittle materials such as concrete and rock using different methods and special samples [8, 24]. The uniaxial tensile strength of concrete is significantly affected by the way the test is performed. The shape of the sample, the concentration of local stress, and the way of sample setting are important factors that affect the obtained results [8, 25].

Therefore, in this section, the direct tensile strength of concrete was measured using a new apparatus based on a compressive-to-tensile load converter. In this developed apparatus, easy loading and direct tensile strength measurement results are close to reality. We will talk more about this apparatus in the following.

2.2. New Direct Tensile Testing Using CTLC

A new direct tensile test apparatus based on a compressive to tensile load converter (CTLC) is used to determine the direct tensile strength of concrete, considering specific samples with dimensions of 19 cm in length, 16 cm in width, 6 cm in thickness, and a central hole diameter of 9 cm. This testing apparatus is equipped with strain gauges that are installed on the specially prepared samples. The load converter apparatus comprises different hard steel components. Component 1 comprises two sections that are installed at the top and bottom of the apparatus, as shown in Figure 2a. Component 2 comprises two steel circles with diameters of 65 mm and a thickness of 10 mm, as shown in Figure 2b. Component 3 comprises two cylindrical rods, with 200 mm and

120 mm in length, 38 mm in width, and 15 mm in thickness, as shown in Figure 2c.

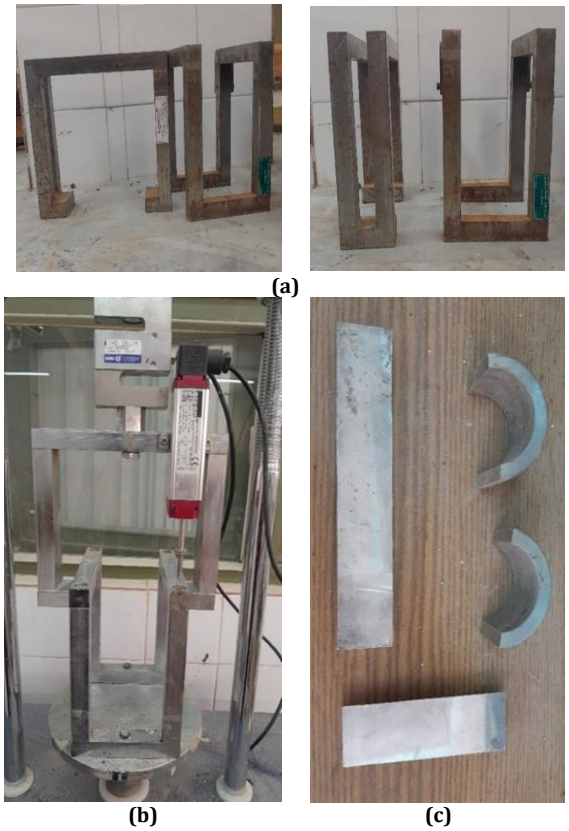

Fig. 2. Components of the compressive to tensile load converter (CTLC): (a) Jaws for direct traction, (b) Cylindrical rods and loading steel circles, and (c) CTLC apparatus assembly

The steps for setting up the CTLC apparatus are as follows:

- The concrete sample is placed along the top of the lower jaw of the apparatus, and the upper jaw is placed on the left and right sides of the sample.
- Two steel circles are inserted into the central hole of a rectangular sample, and a cylindrical rod is placed on the steel circle above the lower jaw of the apparatus, which holds the upper part of the sample. The second cylindrical rod is placed on the lower steel circle of the sample, on which the upper jaw of the apparatus is placed.

This apparatus is developed in such a way that the upper part of the concrete sample is in contact with the lower jaw of the apparatus, and the lower part of the concrete sample is in contact with the upper jaw of the apparatus. The lower jaw of the apparatus is movable and drives a cylindrical rod upwards, which compresses the upper part of the sample. So that the upper jaw of the apparatus is fixed, and the lower part holds the sample. As a result of applying force in the opposite direction, the lower part of the sample is also under pressure. It can be seen that the concrete samples are fractured under tension along the horizontal axis. The setup process of the compressive to tensile load converter is shown in Figure 3.

Fig. 3. The process of setting up the new apparatus based on the compressive to tensile load converter

The direct tensile strength is calculated using the compressive to tensile load converter from Eq. (2).

$$\sigma_\tau \frac{f}{(d_1 + d_2)\, x\, t} \qquad (2)$$

Where σ_τ is the tensile strength, f is the applied load in kg, (d1+d2) is the width of the fracture zone on both sides of the sample, and t is the sample thickness.

2.3. Sample Preparation Techniques

Rectangular concrete samples with a central hole are made from suitable mixtures: gravel, sand, and cement according to ASTM standards. The mentioned samples were prepared by considering 15% cement, 10% water, 43% sand, and 32% gravel, and were tested after a period of 28 days. These samples are 19 cm long, 16 cm wide, and 6 cm thick with a central hole diameter of 9 cm, as shown in Figure 4.

Fig. 4. Rectangular samples with a central hole

2.4. Determination Of Concrete Aggregates

First, to make concrete samples, a sand and gravel grading test was done. Therefore, in this topic, the sand and gravel grading test has been done considering standard sieves 12/5, 9/5, 6/3, 4/75, and 3/3 mm. A sand grading test was considered to determine the largest aggregate size and how it is distributed.

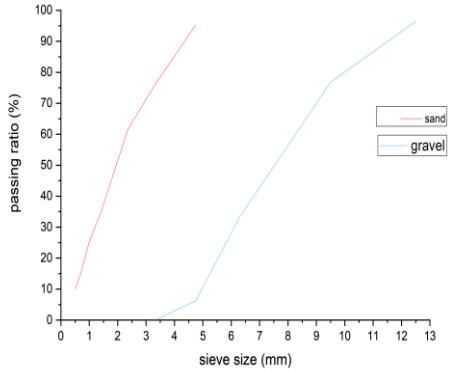

Fig. 5. The graph of the ratio of the percentage of passing the volume of aggregates to the size of the sieve.

From Figure 5, it can be concluded that in the desired mixing design, the size of aggregates (gravel) is between 3.35 and 12.5 mm, and the size of fine aggregates (sand) is between 0.5 and 4.75 mm.

2.5. Calibration Of New Direct Tensile Test Apparatus (CTLC)

CTLC is used to measure the tensile strength of concrete. This apparatus has a capacity of 5 tons of pressure load and records data such as time, load, and displacement to the computer through a cable with Serial Port Monitor software. For the calibration of the new direct tensile test apparatus based on the compressive to tensile load converter, two types of materials— concrete and gypsum— have been used. Rectangular concrete samples with a central hole and Brazilian samples were prepared to measure the tensile strength, considering the same mixing design and the same duration. Rectangular concrete samples with central holes were subjected to direct tensile loading by the CTLC apparatus with a constant loading rate. The results obtained from the direct tensile test were compared with the results of the Brazilian test.

2.5.1. Determining the direct tensile strength test of concrete

Rectangular concrete samples with a central hole were subjected to direct tensile loading by the CTLC apparatus with a constant loading rate of 10 kg/s. This loading rate is within the recommended range for the Brazilian test. All samples were subjected to direct tensile loading, cracks were created along the horizontal line from the center of the hole, and as a result, the said samples were broken. The loading arrangement of a rectangular sample with a central hole under the CTLC apparatus is shown in Figure 6.

Fig. 6. Rectangular specimen with a central hole under CTLC loading

In Figure 7, it can be seen that all the samples were measured under direct tensile loading using the CTLC apparatus. The results indicate that the samples fractured along a horizontal line from the center of the hole.

Fig. 7. Fracture mode of samples under direct tensile loading

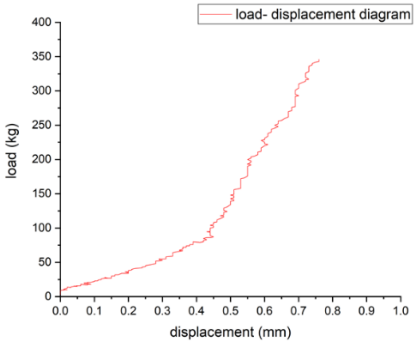

Fig. 8. The diagram of the ratio amount of applied load to displacement

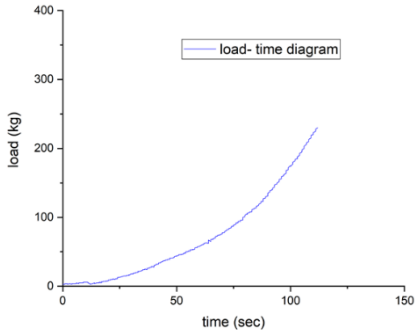

Fig. 9. The graph of the amount of load in relation to time

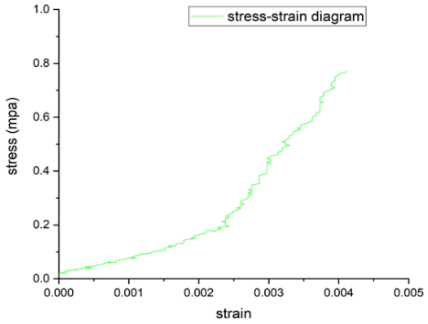

Fig. 10. Diagram of stress-strain ratio

Figures 8 and 9 show that the vertical axis is the load and the horizontal axis is the displacement, and time. The results show that with increasing displacement and time, the load increased. The concrete specimen prepared under tension with a force of 346 kg with a displacement of 0.76 mm in 129 seconds led to failure. Figure 10 also shows the stress-strain ratio, which shows that with increasing strain, stress also increases.

The direct tensile strength of concrete samples has been calculated considering Eq. (2), the results of which are shown in Table 3.

From Table 3, it can be concluded that seven concrete samples in the same loading conditions and dimensions were subjected to the loading of the compressive to tensile load converter apparatus, each of which had different results, and as a result, its average value is 0.65 MPa. This value is the direct tensile strength of concrete.

Table 3. Result of the direct tensile strength test of concrete under CTLC apparatus

Mix design	Components	Values %	Test Method	Tensile strength (MP)
Proper mixing design with Portland cement for 28 days	Water	10	Direct tensile	0.62
	Cement	15	Direct tensile	0.65
	Sand	43	Direct tensile	0.71
			Direct tensile	0.58
			Direct tensile	0.68
	Gravel	32	Direct tensile	0.60
			Direct tensile	0.72
			average	0.65

2.5.2. Determination of the direct tensile strength test of gypsum

Gypsum samples were made as rectangular samples with a central hole, with one-third of water, and then dried at room temperature. These samples were tested under the new direct tensile test apparatus after 48 hours, considering the mixing plan and duration similar to the Brazilian sample. The direct tensile strength of gypsum samples has been calculated considering Eq. (2), the results of which are shown in Table 4. The process of testing gypsum samples under the compressive to tensile load converter test apparatus is shown in Figure 11.

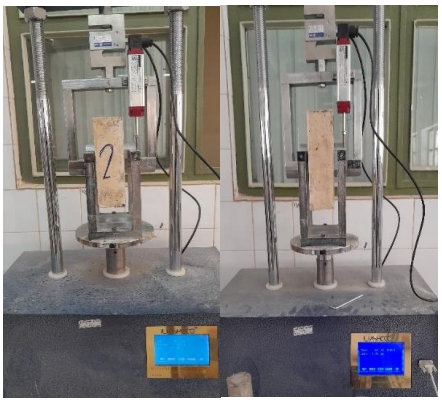

Fig. 11. Rectangular gypsum specimen with a central hole under CTLC loading

The state of failure of the gypsum sample after testing under the direct tensile testing machine of the compressive to tensile load converter is shown in Figure 12. The failure mode of the gypsum samples indicates that the samples were crushed under tension.

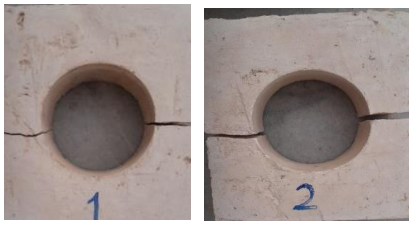

Fig. 12. Fracture mode of samples under direct tensile loading

Table 4. Result of the direct tensile strength test of gypsum under CTLC apparatus

No	Test Method	Time(hour)	Tensile strength(MP)
1	Direct tensile	48	0.58
2	Direct tensile	48	0.51
3	Direct tensile	48	0.65
	average		0.58

Table 4 shows that the average direct tensile strength of gypsum is 0.58 MPa.

2.5.3. Comparison of the Brazilian test and direct tensile test

The Brazilian test is an indirect tensile test used to determine tensile strength. The results show that the Brazilian test determines the tensile strength more. To determine the direct tensile strength of concrete, a new direct tensile test apparatus based on a compressive-to-tensile load converter was used. The failure in the new direct tensile test is the failure that occurred along the horizontal axis with the help of two cylindrical bars. The results obtained from this new direct tension apparatus with a loading speed of 10 kg/s have provided reasonable and acceptable results for determining the tensile strength of concrete compared to the Brazilian test. The comparison of Brazil's test results and direct stress is shown in Table 5. For the validation of the CTLC, about 30 samples were selected, including concrete and gypsum. Different mixing designs were investigated, and the validity of the device was evaluated and confirmed with respect to this wide range of data. A limited number of results are presented in Tables 3 and 4, which are representative of each series of samples. The results of this study show that the CTLC test device is in accordance with reality.

Table 5. Comparison of the results of the new direct tensile test apparatus compared to the Brazilian apparatus

Materials	Concrete	Gypsum
Average direct tensile strength (MP)	0.65	0.58
Average Brazilian tensile strength (MP)	0.88	0.78
Difference between direct and Brazilian tensile strength	26.1%	25.6%

2.5.4. Comparing the results of the direct tension test with the performed work

In this discussion, a direct tensile test device based on a compressive-to-tensile load converter for determining direct tensile strength is reviewed according to the work of researchers.

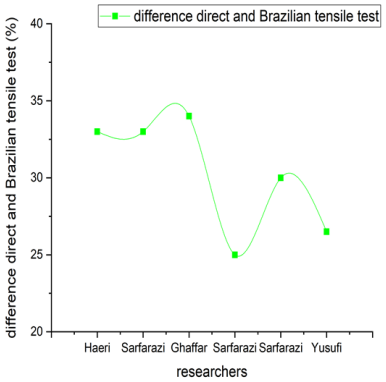

Fig. 13. Diagram of the difference between the direct and Brazilian tensile strength tests based on the researchers' work

Figure 13 shows the difference between direct and Brazilian tensile strength tests performed by researchers in previous years. In this research, the difference of the direct tensile strength test using the compressive to tensile load converter apparatus with the Brazilian sample was 26.1%, which was compared with the works of other researchers.

This difference is usually due to reasons such as loading method, sample size, sample mixing design, and simplifications made by some inventors of these devices. However, the most important issue in validating these results is the common trend in concrete tensile strength and the effect of various factors on its strength.

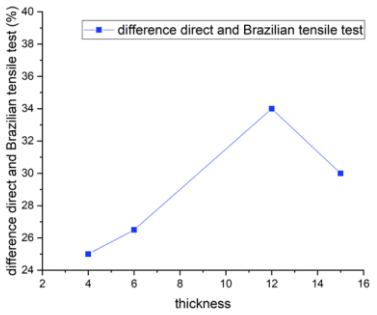

Fig. 14. Tensile strength test diagram according to sample thickness

Figure 14 shows the percentage difference between the Brazilian and tensile strength tests based on the thickness of the concrete samples. As a result, it can be said that by changing the size of the thickness of the sample and the test method, the size of the direct tensile strength of concrete

changes. From this graph, it can be concluded that the concrete tensile strength test is influenced by the dimensions of the sample.

3. INVESTIGATING THE EFFECT OF LOADING RATE AND DIFFERENT MIXING DESIGNS ON DIRECT TENSILE STRENGTH

In this section, the effect of loading rate and different mixing designs with the newly developed apparatus was investigated. Rectangular concrete samples with a central hole made of suitable sand, gravel, and cement mixtures with different mixing designs have been prepared and examined. Concrete samples were made according to ASTM standards from four different mixing designs with the same duration. From each type of mixing design, 3 rectangular concrete samples with a central hole were repeatedly tested to increase the accuracy of the results under the CTLC test. A concrete sample with a duration of 7 days has been tested under a new direct tensile testing apparatus, considering the mixing design and different loading rates. The amount of loading considered to determine the direct tensile strength of concrete using the new direct tensile apparatus is 5, 10, and 15 kg/s. The characteristics of the mixing design are shown in Table 6, which shows that the amounts of fine grains (sand) have decreased from the first to the fourth mixing design.

Table 6. Specification of concrete mixing design to investigate tensile strength

Different types of mixing designs to check the tensile strength of concrete				Parameter
m_4	m_3	m_2	m_1	Component
15%	15%	15%	15%	Cement
10%	10%	10%	10%	Water
25%	39%	40%	45%	Sand
50%	36%	35%	30%	Gravel

From Table 6, it can be concluded that four types of mixing design have been considered to investigate the tensile strength of concrete, that the mixing design m1 comprises of 45% sand, 30% gravel, 10% water, and 15% cement. The direct tensile strength of concrete under the CTLC apparatus was calculated from Eq. (1) by considering different loads and different mixing designs, and its average value for each mixing design is shown in Table 7.

Table 7. Direct tensile strength test results under the influence of different loading rates and different mixing designs

Direct tensile strength with different mixing designs (MP)				Variables
m_4	m_3	m_2	m_1	Loading rate
0.43	0.65	0.68	0.8	5kg/s
0.46	0.66	0.69	0.84	10kg/s
0.67	0.67	0.71	0.89	15kg/s

Table 7 shows the direct tensile strength values considering different mixing designs and different loading rates. The results show that the direct tensile strength increased with increasing loading rate and sand aggregates. Therefore, according to Table 7, the tensile strength is increased from m4 to m1 mixing design.

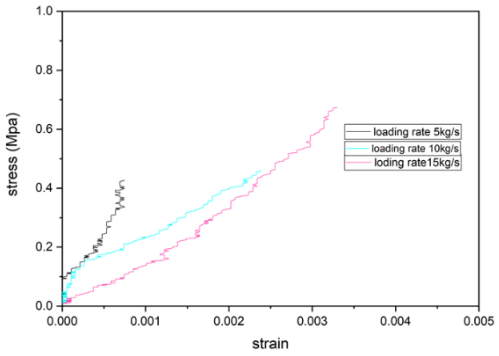

Fig. 15. Diagram of stress-strain ratio

It is shown in Figure 15 that the diagram of the ratio of stress to strain with mixing scheme number 4 is the ratio of sand to sand (25/50), 25% sand and 50% gravel. The results obtained from this graph show that the stress and strain increased with increasing loading rate from 5 to 10 and 15 kg/s.

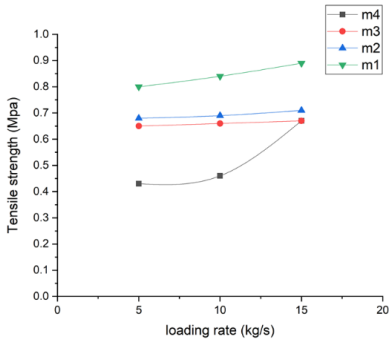

Fig. 16. Diagram of the ratio of tensile strength to loading rate with different mixing designs

Figure 16 shows four types of mixing designs with three loading rates tested under the new direct tensile testing machine. The results show that the direct tensile strength increased with increasing loading rates from 5 to 10 and 15 kg/s and sand to gravel ratios.

4. EFFECT OF LOADING RATE AND MIXING DESIGN ON BRAZILIAN TENSILE STRENGTH

The effect of loading rate and different mixing designs was investigated using the Brazilian

tensile test. Brazilian samples of suitable mixtures: gravel, sand, cement, and water have been made, considering four different mixing designs based on ASTM standards. 3 Brazilian samples for each mixing design were subjected to Brazilian testing after seven days, considering different loading rates and different mixing designs. Brazilian tensile strength is calculated from Eq. (1), and its average for each mixing design is shown in Table 8.

Table 8. Brazilian tensile strength test results according to displacement rate and mixing design

Brazilian tensile strength with different mixing designs (MP)				Variables
m_4	m_3	m_2	m_1	Loading rate
0.58	0.68	0.76	0.82	2mm/min
0.61	0.76	0.92	1.1	2.5mm/min
0.68	1.07	1.1	1.24	3mm/min

Table 8 shows that with the increase of loading rate based on displacement from 2 to 2.5 and 3 mm/min according to different mixing designs, the tensile strength of Brazil has an increasing trend. In all mixing designs, the amount of water is 10% and cement is 15%, and only the ratio of sand to gravel changes. In mixing design number 1, the ratio of sand to gravel (45/30), sand is 45% and gravel is 30%.

The following are the mixing designs numbers 1 to 4:

- Mixing design number 1, the ratio of sand to gravel (45/30)
- Mixing design number 2, the ratio of sand to gravel (40/35)
- Mixing design number 3, the ratio of sand to gravel (39/36)
- Mixing design number 4, the ratio of sand to gravel (25/50)

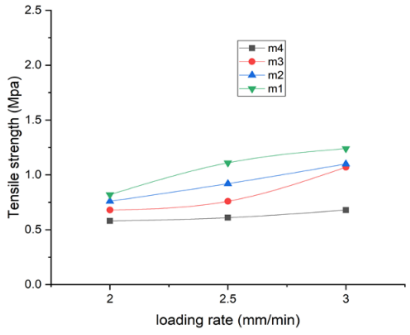

Fig. 17. Graph of the ratio of Brazilian tensile strength to displacement rate with different mixing designs

Figure 17 shows four types of mixing designs with three different loading rates from the Brazilian experiment. The results show that the tensile strength of Brazil increases with the increase in displacement loading rate and sand-to-gravel ratio. Then, by comparing the results of the Brazilian test and the direct tensile test, it has been investigated regarding the effect of loading rate and different mixing designs on the tensile strength of concrete. Brazilian tensile test with different loadings of 2 mm, 2.5 mm, and 3 mm/min, and direct tensile test with different loadings of 5 kg, 10 kg, and 15 kg/s were performed with the same mixing design. The results of the two test methods show that, as shown in Figure 16, the tensile strength increases with the increase in the loading rate.

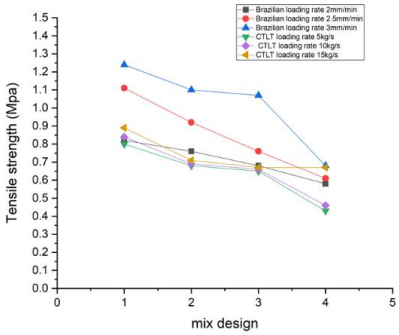

Fig. 18. Graph of the ratio of direct and Brazilian tensile strength to mixing design

From Figure 18, it can be concluded that the direct tension test with a loading rate of 10 kg/s and the Brazilian test with a displacement loading rate of 2 mm/min show similar and suitable results for the tensile strength of concrete.

5. DISCUSSIONS

In the newly developed direct tension apparatus based on the compressive to tensile load converter, it is easy to mount the specimen and apply the load. The amount of tensile strength obtained by this method is close to reality. Also, this apparatus can accurately display the behavior model of brittle materials such as concrete and rock. Then, the effect of loading rate and different mixing designs was investigated with two test methods, a direct tensile test using a compressive to tensile load converter and a Brazilian tensile test. The results obtained from the direct tensile test were compared with the Brazilian test. The results of the Brazilian test show that increasing the displacement-based loading rate from 2 mm/min to 3 mm/min, with a specific mixing design, increases the tensile strength from 0.82 MPa to 1.24 MPa.

The direct tensile test using a compressive to tensile load converter has shown that the tensile strength of concrete with a loading rate of 10 kg/s is 0.84 MPa. When the loading rate was increased

to 15 kg/s, the tensile strength of the concrete was 0.89 MPa, close to the Brazilian tensile strength. The tensile strength of concrete was investigated according to different mixing designs. The results showed that the tensile strength of concrete increased with the increase in the ratio of sand to gravel in the mixing design.

In mixing design number 1, the sand-to-gravel ratio is (45/30), the Brazilian test shows the tensile strength of concrete to be 0.82 MPa, and in mixing design number 4, the sand-to-gravel ratio is (25/50), the tensile strength of concrete is 0.58 MPa. In mixing design number 1, the sand-to-gravel ratio is (45/30), The direct tensile test using a compressive to tensile load converter shows the tensile strength of concrete to be 0.8 MPa, and in mixing design number 4, the sand-to-gravel ratio is (25/50). The tensile strength of concrete is 0.43 MPa.

Figure 19 shows that the more homogeneous the material, the smaller the difference between tensile strength and Brazilian strength. The results show the heterogeneity of concrete compared to plaster, and that the percentage difference between tensile strength and Brazilian strength is higher.

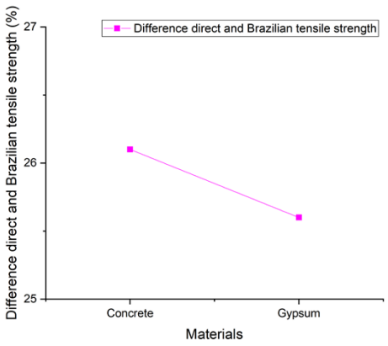

Fig. 19. Percentage difference between direct and Brazilian tensile test results according to material type

In Figure 20, the percentage difference between the direct tensile strength test results under the compressive to tensile load converter apparatus and the Brazilian test apparatus, considering different loading rates, is investigated. The results have shown that by increasing the loading rate of the compressive to tensile load converter test machine and keeping the loading rate of the Brazilian test machine constant, the direct tensile strength results are almost the same as the results of the Brazilian test. Compared to previous laboratory methods, such as the Brazilian method, the CTLC test may better approximate the reality of concrete and rock mass. On the other hand, access to some laboratory tests is limited, but this device has made it possible to determine the tensile strength of concrete and rock.

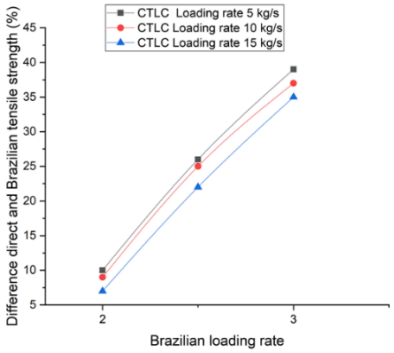

Fig. 20. Percentage difference between direct and Brazilian tensile test results according to loading rate

6. CONCLUSION

The direct tensile strengths of brittle materials such as rocks and concretes can be measured by a new apparatus based on the concept of compressive to tensile load transferring approach. In this research, calibration of the new direct tension apparatus was performed for two types of brittle materials i.e., gypsum and concrete, considering different loading rates and different mixing designs. The rectangular concrete samples with a central hole were prepared for measuring the direct tensile test by a CTLC apparatus at different loading rates. The Brazilian discs were also prepared and tested under vertical force with a constant loading speed of 0.03 mm/s according to standard conditions. The results obtained from the direct tension tests were compared with those gained from Brazilian tensile strength tests, and the following main conclusions were obtained:

- Rectangular gypsum samples with a central hole were tested under a compressive to tensile load converter apparatus with a loading rate of 10 kg/s, and a Brazilian disc sample with a length-to-diameter ratio of 0.5 with a loading rate of 0.03 mm/s. The direct tensile strength is about 25.6% less than that measured by the Brazilian test.
- The results obtained from the direct tensile strength measuring apparatus were compared with the works of other researchers, which showed very close agreement with their results.
- The effects of loading rate and different mixing designs on the tensile strength of concrete specimens were investigated by the two testing methods. It has been shown that the results obtained from the present work demonstrate that tensile strength

increases with the increase in the loading rate and the ratio of sand to gravel.

- The results show that the direct tensile strength test yields significantly lower values (26.1% on average) for the tensile strength of concrete samples compared to the Brazilian tests.

REFERENCES

[1] Resan SF, Chassib SM, Zemam SK, Madhi, MJ. 2020 New approach of concrete tensile strength test. Case Studies in Construction Materials.: 12, e00347. https://doi.org/10.1016/j.cscm.2020.e00347

[2] Andreev ،G. ،1991 A review of the Brazilian test for rock tensile strength determination. Part II: contact conditions. Mining Science and Technology. 13(3): p. 457-465. https://doi.org/10.1016/0167-9031(91)91035-G

[3] Fu J, Sarfarazi V, Haeri H, Shahbazia A, Marji MF, Yu Y, 2022. Study of tensile crack growth in rock-like materials under punch shear test. Theoretical and Applied Fracture Mechanics: 121.p.103509. https://doi.org/10.1016/j.tafmec.2022.103509.

[4] Aghakhani MR., Fatehi M, Hashemzade A, Abdolahipour A, Sanei M. 2023. Prediction of elastic parameters in gas reservoirs using ensemble approach. Environ Earth Sci 82, 269. https://doi.org/10.1007/s12665-023-10958-4.

[5] Sanei, M., Faramarzi, L., Fahimifar, A., Goli, S., Mehinrad, A., Rahmati, A. Shear strength of discontinuities in sedimentary rock masses based on direct shear tests. International Journal of Rock Mechanics and Mining Sciences, 2015: vol.75, pp. 119-131. https://doi.org/10.1016/j.ijrmms.2014.11.009.

[6] Sanei, M., Faramarzi, L. Empirical development of the rock mass deformation modulus. Journal of Geological Resource and Engineering, 2014: vol.2, No.1, pp.55-67. https://doi.org/10.17265/2328-2193/2014.01.006.

[7] Fakhimi A. and Labuz J.F. 2022. A simple apparatus for tensile testing of rock. International Journal of Rock Mechanics and Mining Sciences.: 158: p. 105208.

[8] Zhou L, Haeri H, Sarfarazi V, Marji MF, Naderi AA, Vayani MH, 2022. Experimental and numerical investigation on the thickness effect of concrete specimens in a new tensile testing apparatus.: Vol. 31, No. 1 p 71-84 https://doi.org/10.12989/cac.2023.31.1.071

[9] Li R،Liu L, Zhang ZH, An H, 2020.Experimental Study of Brazilian Tensile Strength of Concrete Under Static Loads. in E3S Web of Conferences. EDP Sciences. Volume 206, p 4: https://doi.org/10.1051/e3sconf/202020601018

[10] Khan MI. 2012, Direct tensile strength measurement of concrete. Applied mechanics and materials, ، 117: p. 9-14.

[11] Qing L،Shi X, Mu R, Cheng Y, 2018: Determining tensile strength of concrete based on experimental loads in fracture test. Engineering Fracture Mechanics 202: p. 87-102.

[12] Li D. and Wong L.N.Y, 2013. The Brazilian disc test for rock mechanics applications: review and new insights. Rock mechanics and rock engineering: ،46: p. 269-287.

[13] Alhussainy F, Hasan HA, Rogic S, Sheikh MN, Hadi N.S, 2016. Direct tensile testing of self-compacting concrete. Construction and Building Materials: 112: p. 903-906.

[14] Silva RV, de Brito G and Dhir RK, 2015. Tensile strength behavior of recycled aggregate concrete. Construction and Building Materials, 83: p. 108-118. https://doi.org/10.1016/j.conbuildmat.2015.03.034

[15] Mubasher B،Bakhshi M and Barsby C،2014. Back calculation of residual tensile strength of regular and high-performance fiber reinforced concrete from flexural tests. Construction and Building Materials:70:p.243-253. https://doi.org/10.1016/j.conbuildmat.2014.07.037

[16] Abdollahipour A, Marji MF, 2020. thermo-hydromechanical displacement discontinuity method to model fractures in high-pressure, high-temperature environments, Renewable Energy. Elsevier: 153, 1488-1503.

[17] Fu J, Haeri H, Sarfarazi V, Asgari K, Ebneabbasi P, Marji MF, M Guo, 2022. Extended finite element method simulation and experimental test on failure behavior of defects under uniaxial compression, Mechanics of Advanced Materials and Structures, 29

[18] Abdollahipour A, Fatehi MF, Yarahmadi BAR, Gholamnejad J, 2016. Numerical investigation of effect of crack geometrical parameters on hydraulic fracturing process of hydrocarbon reservoirs, Journal of Mining and Environment: 7 (2), 205-214.

[19] Gomez J.T, Shukla A and Sharma A, 2001. Static and dynamic behavior of concrete and granite in tension with damage. Theoretical and Applied Fracture Mechanics، 36(1): p. 37-49 https://doi.org/10.1016/S0167-8442(01)00054-4

[20] Fakhri D, Hossein M, and Mahdikhani M, 2022. Effect of glass and polypropylene hybrid fibers on Mode I ،Mode II ،and Mixed-Mode fracture toughness of concrete containing micro-silica and limestone powder. Journal Mining.

Environments: 13: p. 559-577. https://doi.org/10.22044/jme.2022.11936.2188

[21] Sarfarazi V, Haeri H, Ebneabbasi P, Shemirani AB, Hedayat AR, 2018. Determination of tensile strength of concrete using a novel apparatus. Construction and Building Materials: 166: p. 817-832.

[22] Zain M.F.M, Mahmud HB, Ilham A Faizal M, 2002. Prediction of splitting tensile strength of high-performance concrete. Cement and Concrete Research ،32(8): p. 1251-1258. https://doi.org/10.1016/S0008-8846(02)00768-8

[23] Gong F, Zhang L, and Wang S, 2019. Loading rate effect of rock material with the direct tensile and three Brazilian disc tests. Advances in Civil Engineering: 2019, Article ID 6260351, 8 pages. https://doi.org/10.1155/2019/6260351.

[24] Zoumaki M, Tsongas K, Tzetzis D, Mansour G, 2022. Corn Starch-Based Sandstone Sustainable Materials: Sand Type and Water Content Effect on Their Structure and Mechanical Properties. Sustainability:14(14): p.8901. https://doi.org/10.3390/su14148901

[25] Panian ،R. and M. Yazdani. 2020. Estimation of the service load capacity of plain concrete arch bridges using a novel approach: Stress intensity factor. in Structures. Elsevier:

[26] Sanei M, Rahmati A, Faramarzi L, Goli S, Mehinrad, A, 2013. Estimation of rock mass deformation modulus in Bakhtiary dam project in Iran. In: 3rd ISRM SINOROCK Symposium, Rock Characterisation, Modelling and Engineering Design Methods, Shanghai, China, pp 161-164.

[27] Guo L, Peng X, Zhao Y, Liu G, Tang G, Pan A. 2022. Experimental study on direct tensile properties of cemented paste backfills. Advances in Design and Implementation of Cementitious Backfills:(ADICB). https://doi.org/10.3389/fmats.2022.864264

[28] Andreev GE, 1991. A review of the Brazilian test for rock tensile strength determination. Part I: calculation formula. Mining Science and Technology. 13(3): p. 445-456.: https://doi.org/10.1016/0167-9031(91)91006-4

[29] Sarfarazi V. Haeri H, Ebneabbasi P, Shemirani AB, Hedayat, AR. 2018. Determination of tensile strength of concrete using a novel apparatus. Construction and Building Material.: 166: p. 817-832.

[30] Nianxiang ،X. and L. Wenyan. 1989. Determining tensile properties of mass concrete by direct tensile test. Materials Journal.: 86(3): p. 214-219.

[31] Kim JJ, and Reda Taha M, 2014. Experimental and numerical evaluation of direct tension test for cylindrical concrete specimens. Advances in civil engineering: Article.ID 156926| https://doi.org/10.1155/2014/156926 ،.

[32] Sarfarazi V, Ghazvinian A, Schubert W, Nejati HR, Hadei, R ،2016. A new approach for measurement of tensile strength of concrete. Periodica Polytechnica Civil Engineering: 60(2): p. 199-203.

[33] Liao WC, Chen PS, Hung CW, Wagh SK, 2020. An innovative test method for tensile strength of concrete by applying the strut-and-tie methodology. Materials:13(12):p.2776. https://doi.org/10.3390/ma13122776

[34] Sarfarazi V, Haeri H and Marji MF. 2021. On Direct Tensile Strength Measuring of Anisotropic Rocks. Journal of Mining and Environment: 12(2): p. 491-499.

[35] Haeri, H., Sarfarazi, V., Marji, M. F., Yavari, M. D., & Zahedi-Khameneh, A. (2021). Direct tensile strength measurement of granite by the universal tensile testing machine. Smart Structures and Systems, 27(4), 559–569. https://doi.org/10.12989/SSS.2021.27.4.559

[36] Fu, J., Sarfarazi, V., Haeri, H. et al. Improving the tensile strength of reinforced concrete: evaluating the impact of different fiber additives through numerical and experimental analysis. Comp. Part. Mech. 12, 775–792 (2025). https://doi.org/10.1007/s40571-024-00839-3.

[37] Wang, J., Wu, Z., Deng, S., Wang, M., Tao, J., Xie, A., & Wang, Z. (2025). The dynamic tensile strength prediction model and tensile behavior of concrete considering pores based on the impact splitting tensile test. In Journal of Building Engineering (Vol. 104, p. 112272). Elsevier BV. https://doi.org/10.1016/j.jobe.2025.112272.

[38] Heydari, M. , Aghakhani Emamqeysi, M. R. and Sanei, M. (2022). Finite element analysis of wellbore stability and optimum drilling direction and applying NYZA method for a safe mud weight window. *Journal of Analytical and Numerical Methods in Mining Engineering*, 11(29), 67-76. doi: 10.22034/anm.2022.2582

[39] Dehghani, B. , Faramarzi, L. and Sanei, M. (2014). Stability Analysis of Powerhouse Caverns of Bakhtiary Dam Using 3DEC Software. *Journal of Analytical and Numerical Methods in Mining Engineering*, 4(8), 95-108. doi: 10.29252/anm.2014.576

[40] Rajabi, H. , Amin Nejad, B. and Ebrahimi, H. (2023). Numerical Modeling of Fluid Behavior on the Body of a Concrete Double-Arched Dam Considering the Interaction of Water and Structure under Impact Loads. *Journal of Analytical and Numerical Methods in Mining Engineering*, *13*(35), 63-77. doi: 10.22034/anm.2023.18761.1561

Journal of Analytical & Numerical Methods in Mining Engineering

Volume 15, No.45, Winter 2026 ISSN: 2251-6565